

STUDY OF LIQUID FUEL FLAME TOPOLOGIES VIA NEW DIAGNOSTIC
CONSIDERATIONS

By

Amirreza Gandomkar

A DISSERTATION

Submitted to
Michigan State University
in partial fulfillment of the requirements
for the degree of

Mechanical Engineering—Doctor of Philosophy

2024

ABSTRACT

This thesis presents a comprehensive study of liquid fuel flame topologies through the development and application of novel diagnostic techniques. The complexities associated with liquid fuel combustion, particularly in the context of aviation and aerospace applications, demand a deeper understanding of flame behavior and stability. Traditional diagnostic methods often fall short due to the intricate interactions between liquid droplets, flame surfaces, and multi-component fuel mixtures.

Our research focuses on addressing these challenges by introducing advanced diagnostic approaches to investigate the structure, stability, and extinction characteristics of liquid fuel flames. Key areas of exploration include the identification and analysis of reaction zones, the impact of vaporization dynamics, and the effects of turbulent flow conditions on flame stabilization. To achieve this, we employ Laser-Induced Fluorescence (LIF) and chemiluminescence imaging, alongside advanced numerical image processing algorithms to capture high-resolution data on flame behavior. These methods enable us to discern fine details about flame front interactions, droplet vaporization, and localized extinction events. By refining these diagnostic tools, we aim to provide clearer insights into the parameters influencing flame stability, such as equivalence ratio, mixing efficiency, and preheat temperature.

In addition, the study integrates computational simulations using CHEMKIN to validate experimental results, allowing for a more comprehensive understanding of how liquid fuel combustion behaves under varying conditions of turbulence and strain rates. The combined experimental and computational approach ensures that the findings are both robust and applicable to real-world aerospace scenarios.

The findings of this study contribute to the broader understanding of liquid fuel combustion processes and offer valuable implications for the design and optimization of more efficient and stable combustion systems in aerospace applications. This research not only enhances our theoretical knowledge but also provides practical guidelines for improving flame diagnostics and combustion performance.

Copyright by
AMIRREZA GANDOMKAR
2024

ACKNOWLEDGMENTS

First and foremost, I want to extend my heartfelt gratitude to my advisor, Dr. Patton Allison. His warm welcome into his lab, unwavering patience, and steadfast support throughout every step of my journey have been invaluable. Dr. Allison's exemplary passion for knowledge and science, his commitment to constructive collaboration, and his insightful guidance have profoundly shaped my thinking and were instrumental in the completion of this manuscript. I am also deeply grateful to my committee members, Dr. Wichman, Dr. Toulson, and Dr. Lira. Their constructive criticism, kind demeanor, and expert guidance helped me navigate the path to selecting the correct research topic. Finally, I would like to thank my family and friends, whose support and encouragement have been a constant source of strength, even from miles away.

TABLE OF CONTENTS

Chapter 1 Introduction	1
Chapter 2 Experiments & Methodology	22
Chapter 3 Prevaporized Liquid Fuels	55
Chapter 4 Spray Liquid Fuels	68
Chapter 5 Chemiluminescence	80
Chapter 6 Summary and Discussion	97
BIBLIOGRAPHY	105
APPENDIX	112

Chapter 1

Introduction

1.1 Background and Motivation

Liquid fuel combustion is favorable for aviation applications in the aerospace field, especially gas turbines. Little research has been conducted on liquid fuel reacting flow. The interaction of liquid droplets with the flame surface, flammability limitation, and complex fuel's multi-component properties add up to the difficulty of the problem of liquid fuel combustion. The interaction of liquid spray droplets with the flame surface and the slow vaporization process compared to the dynamics of the flow raise questions about the flammability of the mixture and the flame stabilization. The lean condition flammability and flame stabilization depend on the complex conditions where turbulent chemistry of local mixing fuel-air and fluid dynamics interact. This issue depends on several parameters: burner structure, fuels, strain rate, equivalence ratio, and preheat temperature. The flame stabilization is determined by lift-off and blow-off conditions. Lift-off is an intermediate stage before the blowout occurs, where the mixture of air and fuel velocity is higher than the flame speed and the flame detaches from the burner, stabilizing with an offset from the burner. As the mixture velocity increases, the offset height increases until blow-off happens. Under blow-off conditions, the velocity of the mixture is high enough that it does not allow the flame and chemistry to

stabilize around the burner. Flame stability and extinction result from the balance between the fluid dynamics timescale and the mixing timescale, or simply put, the balance between fluid velocity and flame speed. Flame speed depends on various parameters such as the equivalence ratio, mixing efficiencies, and preheat temperature. Flame stability is determined by whether the flow speed is higher or lower than the flame speed. For liquid flames, stabilization and extinction are more complicated due to the additional factor of vaporization timescale. In turbulent and high Reynolds number flow, the mixing and combustion timescales are longer compared to the fluid dynamics timescale. This can cause severe quenching in the flame, leading to its destabilization. The main goal of this research is to investigate local extinctions by focusing on the coupling between the flame structure, the turbulent flow field, and the interactions of droplets with the flame. Heavy hydrocarbon liquid combustion is a complex phenomenon due to the cracking into multiple components and the interaction between liquid droplets and the flame. Most diagnostic techniques are not applicable because of the limitations imposed by combustion and liquid droplet interference. Consequently, there is a lack of knowledge in this field, which intrigues researchers to investigate various aspects of this subject. The motivations behind this research include studying turbulent flame characteristics, flame stabilization, and the extinction of liquid fuel flames.

Also, the mixing process of liquid fuel is complicated compared to gaseous fuels. Since the timescale for vaporization is relatively more significant than the fluid dynamics timescale, the flammability of the mixture is unknown due to different local equivalence. Additionally, liquid fuel studies with diagnostic techniques face several difficulties. Liquid droplet interference with optical measurement is a severe problem in the diagnostic approach. Hence, most studies involve gaseous fuels, while few studies have been done on liquid fuels.

Optical measurement methods in the combustion process are widely popular, and monitoring species emissions and controlling parameters influencing the combustion phenomenon is essential. The most common approach to studying the flame structure is Planar Laser-Induced Fluorescence, PLIF. At the same time, chemiluminescence is the easiest way

to evaluate intermediate species, revealing vital information regarding flame characteristics. These two approaches are implemented in our studies and will be introduced later.

Chemiluminescence is the light emitted from a chemical reaction. An excited intermediate species that has high energy to reach a stable state releases its energy as photons of light. The chemiluminescence light emitted by the flame is well suited for diagnostic purposes. Chemiluminescence is used to obtain information in the reaction zone, which is related to combustion performance, species formation, quenching, and emission. This method has been widely used to measure equivalence ratio, heat release, flame front location, and other potential information that can illustrate the condition of combustion. One of the biggest advantages of chemiluminescence is that it is much cheaper than other measuring methods in combustion and it can be set up much easier. Unlike laser diagnostic or other methods, chemiluminescence does not need an external source for light since this process emits light during species formation by heat release. This emitted light is used as a means of diagnostic measurement since it has information about the local combustion processes. The most important species to be investigated in the combustion process are OH^1 , CH^2 , and possibly CO_2^3 . It has been noted that the relative intensities of different species depend on the fuel equivalence ratio, pressure, strain, and performing conditions. Much research has been done in numerical and experimental methods to find out the importance of species intensities and connect them to the conditions of systems.

Laser Induced Fluorescence (LIF) is optical emission from molecules or atoms that have been excited by an external source of energy. The flow is illuminated by a tunable laser that overlaps an allowed electronic vibrational or rotational transition in an atom or molecule. By absorbing the energy, the molecule reaches an excited state. The molecule can release that energy in two ways: 1-colliding with another molecule, named collisional quenching. 2-relaxing back to the ground state and emitting photons as fluorescence. LIF is

¹Hydroxyl radical

²Methylidyne radical

³Carbon dioxide

a unique and useful method for measuring variables or visualization. It can be implemented to measure various data such as density, concentration, velocity, temperature, pressure, etc. It can be used at a single point, line, or even a sheet, which is called PLIF⁴. LIF (Laser-Induced Fluorescence) is a resonant technique that requires the laser to be tuned to a specific wavelength. Single-photon LIF is linear, but it often has a low signal, necessitating the use of an Intensified CCD⁵ (ICCD) to amplify the signal. However, this amplification also increases the noise level.

The LIF method differs for the liquid phase and gaseous phase. For the liquid phase, fluorescence particles are seeded with the flow, and by absorbing energy and releasing it, measurements of concentration, temperature, etc., are performed, while in the gaseous phase, the seeded particle is not a proper way since the species have unique excitation wavelengths, and the illuminating part is not just due to the particles. For the gas phase, a specific wavelength for tuning the laser is needed to excite a specific species, and that excited species will release photons after relaxation.

Examining flame structure gives insight into the influence of turbulent flow and is beneficial for simulation and modeling. Many studies have investigated the effect of pressure [Soika et al., 2003, Lachaux et al., 2005], turbulent intensity [Jenkins and Cant, 2002, Haq et al., 2002], and Lewis number [Rutland and Trouvé, 1993, Chakraborty and Cant, 2005, Renou et al., 1998] on flame topology. Most of the previous studies focused on gaseous fuel flame. The studies on the liquid-fuel flame topology are limited and restricted due to the interference of liquid droplets in diagnostic techniques and the complexity of heavy hydrocarbon-fuel combustion.

Walsh [Smooke et al., 1996] investigated CH and OH chemiluminescence in laminar diffusion flame for methane-nitrogen fuel with experimental and simulation methods. They used two different chemical mechanisms for the numerical procedure and then compared the results with Laser Infrared Fluorescence diagnostic in their experiment. The first mechanism

⁴Planar Laser-Induced Fluorescence

⁵Charge-Coupled Device

was GRI Mech 2.11 and the second was an alternate hydrocarbon mechanism. The results as shown in Figure 1.1 indicate that the GRI mechanism predicts CH and OH intensities and their spatial resolution quite accurately while the alternate hydrocarbon mechanism has a better lift-off match with the LIF method.

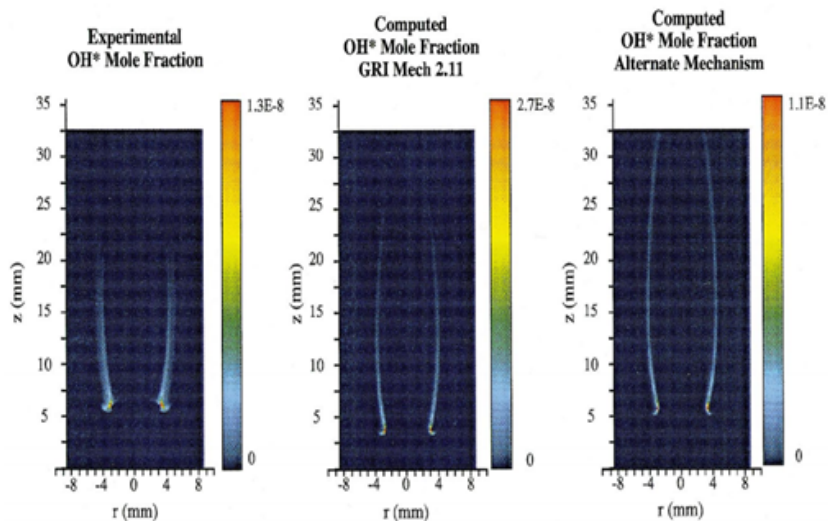


Figure 1.1: Comparison of OH PLIF and two simulations [Smooke et al., 1996]

One of the parameters which affect the emission and combustion are characteristics of fuel. Armingol [García-Armingol and Ballester, 2014] researched different compositions of fuels and their effect on chemiluminescence emission and they also tried to come up with a correlation between chemiluminescence signals and equivalence ratio. They used about 12 different mixtures of CH₄, CO, H₂ and CO₂. Numerical modeling with CHEMKIN was also performed in their study with two different simulation models to understand which one predicts the experimental results better. The models were performed by Chemkin for turbulent flame situations, named as the "free propagating laminar flame" and "the perfectly stirred reactor" (PSR). They observed that by adding methane to syngas (CO and H₂) the maximum concentration of OH increases because CH has an important role in formation of OH.

An experiment focusing on the effect of diluent in a methane-air mixture with CO₂ and N₂ was done by Guiberti [Guiberti et al., 2017]. Their experiments indicated that increasing

CO₂ and N₂ diluent would decrease the chemiluminescence of CH and OH. The decreasing rate will magnify if the concentration of diluent increases. Also as shown in figure 1.2 , they expressed that the ratio of CH/OH does not change significantly with the change in N₂ dilution, however increasing CO₂ concentration led to decrease in the ratio of intensities.

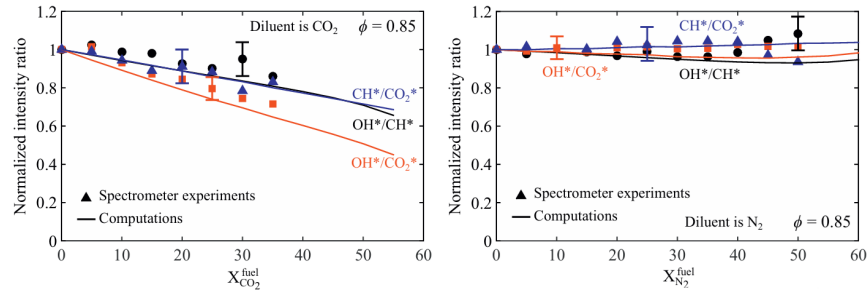


Figure 1.2: Species chemiluminescence ratio vs percentage of diluted N₂ and CO₂ and equivalence ratio [Guiberti et al., 2017]

Tripathi [Tripathi et al., 2012] investigated chemiluminescence of OH and CH in the premixed flames of methane air for various equivalence ratios by observing the reaction zone. The first impression in their results shown in Figure 1.3 is that background emission of CO₂ decreases with increasing equivalence ratio, which is normal due to low production of CO₂ at rich flame combustion, but the impact of equivalence ratio on other species emission is not certain due to the fact that they all are affected by the presence of CO₂ in the background. To eliminate background CO₂ and obtain better results for CH and OH intensities, they used a new partial least square regression (PLS-R) sensing method and measured OH and CH chemiluminescence for a range of equivalence ratios. They showed that OH peak occurs at an equivalence ratio of 0.8 and CH intensity peak happens around equivalence ratio (ϕ) of 1 and both intensities start to decrease after their peak with increasing equivalence ratio. They also came up with a correlation for the ratio of OH/CH and equivalence ratio.

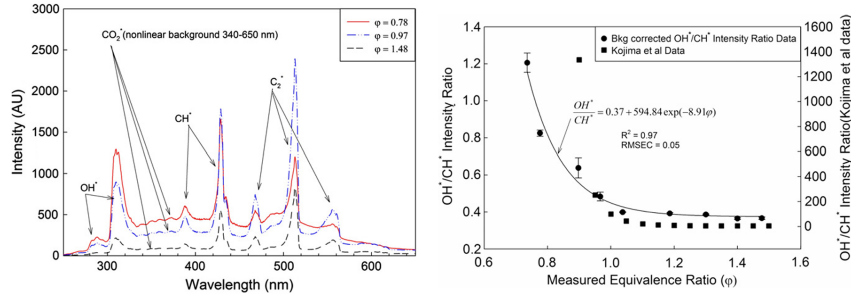


Figure 1.3: Species chemiluminescence ratio vs percentage of diluted N_2 and CO_2 and equivalence ratio [Tripathi et al., 2012]

Higgins's [Higgins et al., 2001] experiment focused on the influence of pressure, equivalence ratio, and flow rate on OH chemiluminescence intensity in the lean combustion region, laminar premixed methane-air flame. Their results seen in Figure 1.4 showed that in the lean combustion region, increasing pressure decreases OH intensities due to increasing collisional quenching at higher pressures. Also, OH chemiluminescence increased with increasing flow rate since they have a proportional relationship with each other.

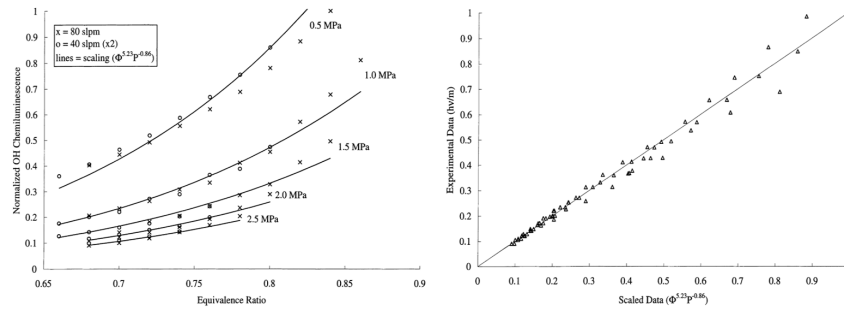


Figure 1.4: OH chemiluminescence intensity vs equivalence ratio and their correlation with pressure [Higgins et al., 2001]

Panoutsos [Panoutsos et al., 2009] simulated 8 different mechanisms and sub-mechanisms introduced by other researchers and compared them with experimental results. Their research focused on the effect of equivalence ratio on CH and OH chemiluminescence and heat release ratio. They expressed that OH could be helpful in tracking the heat release rate since it has the lowest distance between the peak of OH and the peak of the heat release profile, which can be seen in Figure 1.5. Also, OH and CH intensities were calculated and measured

for all mechanisms and experimental data, showing that these intensities depend greatly on equivalence ratio and strain rate. However, it was mentioned that the ratio of OH to CH depends only on the equivalence ratio and is independent of strain rate. All the mechanisms in this research showed a good match with the experimental data. Finally, they mentioned which mechanism works well for each species of interest.

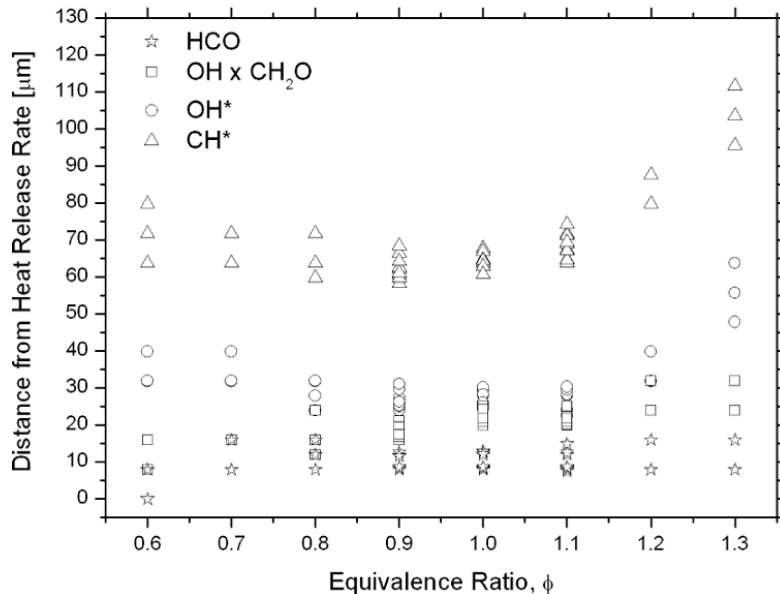


Figure 1.5: Calculated peak-to-peak distances between heat release rate and HCO, OH \times CH₂O, OH and CH, as a function of equivalence ratio [Panoutsos et al., 2009]

Constandinos [Mitsingas et al., 2019] investigated PIV⁶ and LIF⁷ in turbulent premixed methane flame using a Bunsen flame burner stabilized with a pilot burner. They obtained flame structures by analyzing the data of the CH and OH PLIF. Also, reactant pockets residing in the product stream, product pockets residing in the reactant stream, and interaction between out-of-plane and in-plane flame sheets were extracted from this analysis. Furthermore, the PLIF and PIV experiments' results measured the axial velocity and fluctuations, and the reaction layer was tracked down.

Rosell [Rosell et al., 2017] studied multi-species (CH, OH, CH₂O, and toluene) PLIF to better understand the structure of turbulent flame and reaction zones. In order to track

⁶Particle Image Velocimetry

⁷Laser-Induced Fluorescence

the unburned fuel, they excited toluene, a product formed from the breakdown of methane. The methane-air mixture was pumped through the McKenna burner with a pilot burner as the stabilizer. A Laser Doppler Anemometer device was implemented in this work to measure axial and radial velocities and their oscillations. They were able to calculate the thickness of OH, CH, and CH₂O layers and the thickness of overlapping layers between each one by the results of PLIF. The preheat zone, which was studied by following an overlapping layer of toluene and CH₂O, depends on the Reynolds number. The thickness of the preheat region increased by Reynolds number, but up until the flow is laminar. For turbulent flow, the preheat zone is independent of the Reynolds number. They observed that the CH layer, an indicator for fuel consumption rate, stayed thin through the experiments over variations of Reynolds number. The same result was obtained for heat release, characterized by an overlapping layer of OH and CH₂O. Also, by having velocities distribution, Karlovitz number and Damkohler number were obtained. Other features such as flame surface density, flame wrinkling ratio, and fuel consumption velocity are also measured. For $Ka < 40$, the surface wrinkle ratio depends on Reynolds number and flame height, and for $Ka > 40$, the surface wrinkle ratio is independent of Reynolds number.

Tsushima [Tsushima et al., 1998] studied droplet cluster behaviors in a premixed spray flame using the chemiluminescence method and Mie scattering technique. Their diagnostic system, which allows for spatially resolved chemiluminescence measurements, is the only viable option for monitoring the transient structure of flames, as laser-induced fluorescence (LIF) cannot provide continuous time-series signals due to the intermittency of pulsed lasers with droplet clusters. In the non-combusting case, there was no cluster seen in the images. In contrast, the continuous spray image was eroded in the combusting case, or no Mie scattering was detected, which is the sign of a droplet cluster. At the same time, the OH chemiluminescence increased, which suggests that the reason behind these events is flame propagation, not fluid motion. In the following period, increased OH intensity and Mie scattering proved that there are combustion reactions inside the spray region and that

droplets burn with flame propagation. In another time step, they observed erosion in spray in the downstream direction while there is no combustion, which means the upstream region of spray prevents flame propagation. At last, observing the disappearance of droplet clusters downstream, they came up with an estimation of disappearance speed.

Cessou [Stepowski et al., 1994] performed investigations of the OH concentration in the stabilization zone of a two-phase jet flame. OH PLIF was used to observe flame structures in the lift-off area of a spray jet flame. They observed that the flame propagates in two diverging and opposed diffusion structures. The thickness of these two structures was measured and reported. Lift-off height was also measured. They noticed that the chance of having a double-branched structure is higher for low atomization velocity. Also, the droplets cross the inner reaction zone to vaporize in the hot mixing structures in the double-branched structure. The peak concentration level they observed was in agreement with the measurement reported by others.

Lemaire [Lemaire et al., 2009] has evaluated liquid spray characteristics using a highly efficient nebulizer in the McKenna piloted burner for three different liquid fuels. Estimation of droplet size, evaporation time, and length of spray scale has been studied. The droplet size and liquid spray measurements were measured using the Mie scattering technique at 532 nm and 1064 nm. It was reported that droplet size distribution for all three fuels was similar to the spray structure exiting the nebulizer captured by the Mie scattering method. Liquid completely vaporized over 15-16 cm above the burner for all fuels.

Meyer [Meyer et al., 2005] investigated the formation of soot in an unsteady turbulent swirled stabilized liquid JP-8 spray combustor. They implemented several diagnostic techniques such as PLIF, Mie scattering, and LII. With the LII method at the swirl section exit area around 415 nm to 500 nm, soot formation and its volume fraction were measured. OH PLIF at 283.922 nm wavelength gave them the distribution of OH and tracked down the local equivalence ratio. Mie scattering was also performed to mimic spray patterns in the combustion flow. They observed that decreasing temperature and lack of oxidizer increase

the soot formation in lean combustion.

Flame surface density is one of the essential details of flame structure, which expresses the flame's wrinkling scale, and it can lead to the flame burning velocity or consumption speed. Zhang [Zhang et al., 2019] experimented with OH PLIF and CH chemiluminescence for a methane-air mixture in bluff-body and swirl stabilizer flame. The behavior of flame root and burning velocity are studied using flame surface density data. Weijie and Meng Zhang [Zhang et al., 2014] studied turbulent methane flame enriched with hydrogen using instantaneous OH PLIF. Their result indicated that the addition of hydrogen enhanced flame surface density, especially in higher turbulent cases. The Flame Surface Density's (FSD) profile for the mean progress variable was symmetric with the maximum location at $\langle c \rangle = 0.5$. For liquid fuel, as it appears, there is no background of flame surface measurement with CH PLIF. Usually, OH PLIF is conducted for capturing FSD, and due to interference of Mie scattering in the PLIF experiment, there are limited PLIF studies for liquid fuels.

Rodrigues [Rodrigues et al., 2015] investigated the addition of air and hot diluted co-flow to the ethanol swirl spray flames. They implemented Laser Doppler Anemometry (LDA) and Phase Doppler Anemometry (PDA) to measure velocities of gas and spray, respectively. Alongside high-speed visualization, they measured temperature in the spray region using anti-Stokes Raman spectroscopy. Their experiment's result can be used for further simulation models since it contains various information about the different regions of spray flame. They observed that hot diluted co-flow has a significant effect on the liquid breakup mechanics. In hot diluted where the droplet is surrounded by hot gas, the maximum temperature shifts toward the lean section, and vaporization of droplets accelerates.

Sadiki [Sadiki et al., 2005] experimentally investigated the vaporization rate and combustion of kerosene in a turbulent spray flame. They utilized Phase Doppler Particle Analyzer (PDPA) to capture velocity and sizes of droplets. In their burner facilities, a methane-air mixture piloted burner was used to stabilize the spray flame. OH chemiluminescence was performed at the wavelength of 308 nm as well. Gas chromatography was performed to

measure the concentration of various gases such as O₂, H₂, CH₄. Due to resolution and secondary light scattering from droplets, Mie scattering images were only used to show droplet dispersion. They observed that faster evaporation, which can be achieved by decreasing the centrifugal Stokes number, does not imply faster combustion. They expressed that dispersion of fuel in the gaseous phase is slower than in the liquid phase. Therefore, the represented flame length is significantly longer compared to the other one.

The DNS results as shown in Figure 1.6 indicate the effect of Lewis number of liquid fuels on heat release and fuel consumption in the region of high curvature [Aspden et al., 2017, Savard and Blanquart, 2015, Savard et al., 2015]. Furthermore, the instantaneous CH PLIF imaging visualizes a substantial variation of CH signals in high-curvature areas for high-Le-number fuels. While for fuels with Le number around unity, there is weak variation in the CH fluorescence signal [McManus et al., 2021]. This behavior intrigues the idea that there may be a relation between Le number, the CH signal, and heat release. The quantification between the CH signal and curvature for different fuels is required to prove this idea.

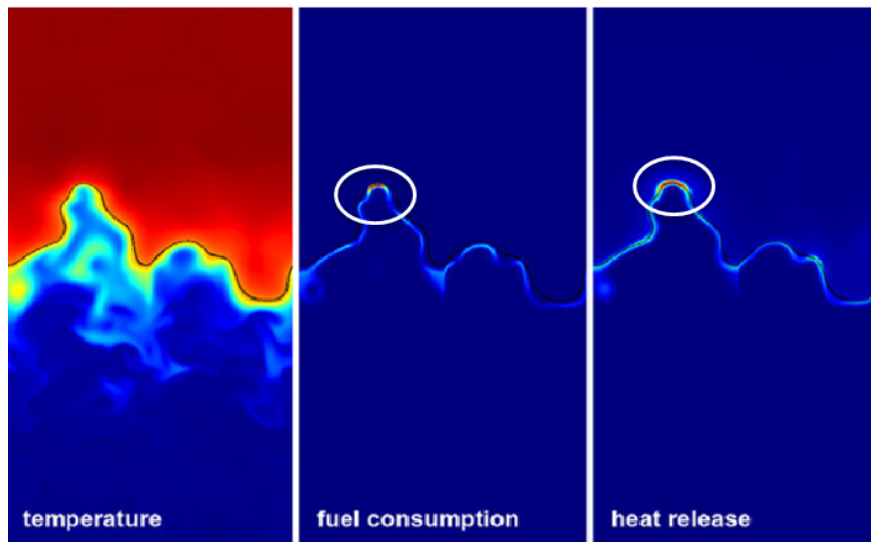


Figure 1.6: Strong variation of temperature, fuel consumption, and heat release around regions of high curvature captured by DNS results [Aspden et al., 2017]

1.2 Gaps and holes in the Research

In this section, I am going to talk about gaps and holes in diagnostic methods in flame studies. First, in the chemiluminescence method, it should be noted that the light emitted by species in combustion produces a relatively low signal compared to other methods, making it more challenging to detect and extract detailed information about flame characteristics. To address the low signal in chemiluminescence, an intensifier can be applied in front of the camera or detector. However, intensifiers typically cause image blurriness. This blur can be partially reduced using image processing techniques.

A primary challenge in this method is detecting CO₂ chemiluminescence, as it spans a wide range of wavelengths and affects measurements of other species. While some studies have attempted to calculate CO₂ chemiluminescence, they are limited to light hydrocarbon fuels. The models for CO₂ are generally confined to a specific range of equivalence ratios and do not fully predict all chemiluminescence trends. For heavier hydrocarbons like kerosene, which exhibit more complex behavior, there is no detailed study. To achieve more accurate measurements for kerosene, a detailed mechanism tailored to this fuel is necessary to improve our understanding of the problem.

In Laser-Induced Fluorescence (LIF), interference from species bands in other LIF signals remains an unresolved issue. For example, in CO LIF, there are reports of interference from the C₂ Swan band in the LIF signals. Similarly, in OH LIF (0,0) around 308 nm, interference occurs due to the proximity of the CH C-X⁸ band at 314 nm. Additionally, for visualizing spray flames, single-wavelength LIF is often unsuitable due to interference from droplets that scatter the fluorescence signal. Some researchers suggest using LIF at an alternative wavelength to mitigate droplet scattering.

Another challenge is the effect of kerosene fuel on diagnostics and flame behavior. Currently, there is no comprehensive mechanism for kerosene combustion, though some surrogates have been proposed to simulate it. The intermediate species produced during

⁸Transition from the third excited electronic state to the ground electronic state

kerosene combustion and their impact on flame front characteristics, chemiluminescence, and LIF remain largely unknown. The interaction between fuel composition and flame structure, which can lead to flame extinction or extended flammability, requires further investigation. A detailed mechanism to accurately predict the reactions involved in kerosene combustion is needed.

Regarding gaps in flame studies, further research is suggested on the interaction between flames and sprays. Studying the effects of product recirculation, unsteady mixing, or preheating could yield valuable insights. Flame extinction caused by droplet clusters or changes in flame length due to such interactions has been explored by only a few researchers. Overall, research on liquid spray flames is limited, indicating a need for the application or combination of various diagnostic techniques in this area.

Conventional laser diagnostics are not recommended for liquid fuel combustion due to interference from liquid fuel and intermediate combustion species. To study the reaction layers of flames and gather information on the extinction process, a new diagnostic method is necessary to enable imaging of liquid fuel combustion despite interference from fuel components. In collaboration with the Air Force Research Laboratory (AFRL), a new diagnostic technique has been developed, using CH PLIF imaging on prevaporized heavy hydrocarbons to study flame structure and extinction. This technique allows for the analysis of liquid fuel flame structure without interference from fuel components. Initial observations suggest that a Lewis number effect may influence the fluorescence signal in regions of high curvature, motivating further investigation into the correlation between Lewis number and signal/curvature.

Additionally, simultaneous CH/OH PLIF observations indicate that OH PLIF may be unable to detect local extinction within the flame structure. Since OH species have a slower quenching rate compared to CH, they may remain present even after flame extinction, potentially leading to an overestimation of flame characteristics in OH PLIF. The OH PLIF signal typically shows a simpler, two-sided structure without product stream orientation,

whereas CH PLIF provides a more detailed view of breaks in the flame structure. As shown in Figure 1.7, simultaneous CH/OH PLIF suggests that OH PLIF fails to detect certain local extinction regions that CH PLIF captures. This study proposes that CH PLIF may offer a more reliable diagnostic technique for turbulent flames where local extinctions are prevalent.

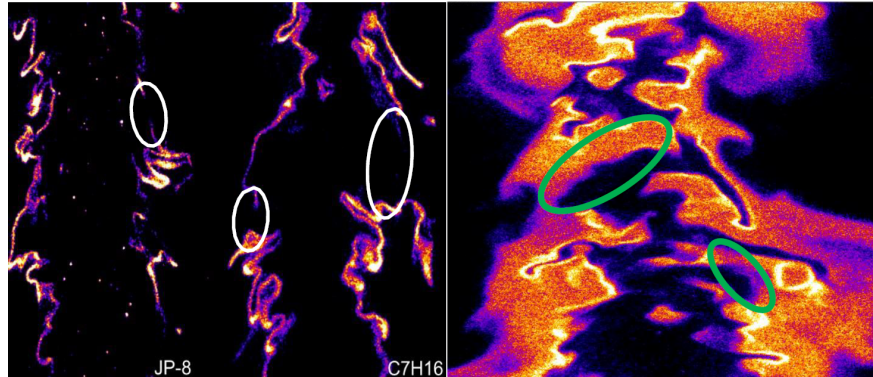


Figure 1.7: Local extinctions, circled, observed in the flame surface via CH PLIF imaging in turbulent liquid fuel jet flames [McManus et al., 2021]

Furthermore, I aim to expand our research on spray liquid flames during the extinction process using our advanced diagnostic technique. The primary motivations for this thesis include:

1. How are finite-rate chemistry effects in low-temperature processes represented in changes to the local flame structure and heat release?
2. How do global extinction behaviors in spray flames differ from those in prevaporized or gaseous fuel flames? Are there experimental indicators of extinction in turbulent sprays?
3. Is our standard diagnostic toolbox for gaseous flames sufficient for studying liquid fuels? If not, what adjustments are necessary?
 - a. Interference-free fluorescence and chemiluminescence from fuel, droplets, or polycyclic aromatic hydrocarbons (PAH)
 - b. Development of a numerical algorithm to address the complexities of turbulent structures

This research aims to examine the turbulent flame structure in liquid fuels, investigating the effects of fuel type and equivalence ratio using CH PLIF and CH*/OH* chemilu-

minescence. A new PLIF diagnostic technique compatible with liquid fuels is utilized in this study. Turbulent flame properties such as flame curvature, flame surface density, turbulent flame speed, and turbulent flame area are analyzed using an innovative image processing approach applied to CH PLIF images. Later in this work, the image processing technique for identifying reactant and product regions will be introduced. Curvature and flame surface density measurements for prevaporized and spray flames of n-dodecane and n-heptane are plotted and compared to premixed methane under similar conditions, as defined in the Borghi diagram [Borghi, 1985]. Finally, CH and OH chemiluminescence data are compared with simulations from various sub-mechanisms to evaluate their accuracy.

This thesis proposes an investigation into turbulent liquid flame characteristics by analyzing the topological features of liquid fuel combustion near blow-off, linking local extinction characteristics to global phenomena.

1.3 Research Objectives and Contributions

In this research, the primary objective is to investigate the turbulent flame structure of heavy hydrocarbon liquid fuels using advanced diagnostic techniques. By implementing CH PLIF (Planar Laser-Induced Fluorescence) to capture flame structure and devising a novel numerical image processing method, this study seeks to measure the turbulent characteristics of flames and local extinction process in liquid fuels. These types of topological statistics have not been experimentally performed before in liquid fuels.

The main complication with UV diagnostics for liquid fuels is interference from fluorescence of the fuel itself, Mie scattering from droplets or soot, and Raman scattering from the fuel. The C-X Q branch CH method performs well in liquid fuels because it is on-resonance, as same input laser wavelength to imaged wavelength, thus avoiding Raman and fuel PLIF, and because the method requires low pulse energies, there is minimal interference. The R-branch excitation works for droplet laden flows because it is off-resonance and the Mie scattering from droplets can be effectively filtered out. Hence CH can be performed in spray flames to

see local extinctions. The capability to conduct CH PLIF in both spray and prevaporized liquid fuels is innovative and valuable for obtaining extinction data, which is not accurately captured with OH PLIF

Our primary objective is to develop an algorithm that accurately captures the flame structure and distinguishes between the reactant and product side of the flame. This algorithm enhances the understanding of flame topology by improving the accuracy and reliability of identifying combustion zones. It addresses the challenge of capturing the dynamic and complex structure of turbulent flames, providing a more detailed and nuanced understanding of the combustion process. Furthermore, the algorithm can highlight the shortcomings of common approaches used in the combustion industry. This contribution is crucial for advancing diagnostic techniques in combustion research.

Additionally, we aim to analyze the turbulent flame features of prevaporized liquid fuels, focusing on flame structure statistics, extinction events, and the interaction of turbulent flow with the flame. The detailed measurement and analysis of these features offer valuable insights into the combustion behavior of prevaporized fuels. By understanding how turbulence affects flame stability and extinction, this research contributes to the optimization of fuel combustion processes, leading to more efficient and stable combustion in practical applications. This is particularly relevant for improving the performance of gas turbines and other aerospace propulsion systems.

Also, we want to investigate the turbulent flame features of liquid spray fuels, examining droplet interactions with the flame, fragmentation, vaporization, and flame stabilization. This objective highlights the differences and similarities between spray and prevaporized fuel, offering a comprehensive understanding of how liquid droplets influence flame behavior. The insights gained from this investigation are critical for optimizing fuel injection and atomization techniques, thereby enhancing combustion efficiency and reducing emissions in liquid-fueled engines. This research also contributes to the development of more accurate predictive models for spray combustion.

Chemiluminescence is an easy diagnostic for industrial applications to observed the flame and derive information about heat release and rough mixture ratio. For CFD efforts, the combustion process is calculated from a chemical mechanism optimized for particular fuels. For comparisons between CFD and industrial measurements, often the only available data on the flame is chemiluminescence. Thus, the CFD calculation also attempts to predict chemiluminescence and require a chemiluminescence chemical sub-mechanism in addition to the primary fuel mechanism. Often, these sub mechanisms are included as part of the main mechanism.

However, issues arise because the primary fuel mechanism is not optimized for the prediction of the primary chemiluminescence species and also because the chemiluminescence sub-mechanisms have been optimized for methane, not liquid fuels. CFD modelers are often unaware of the assumptions under which the mechanism and sub-mechanisms have been derived and optimized. This drives motivation to check if such mechanisms should be trusted for CFD-experimental comparison of liquid fuels.

The analysis of chemiluminescence measurements enhances the accuracy of predictive models for combustion behavior. These improved models support the design of more reliable and efficient combustion systems, benefiting a wide range of applications in aerospace and beyond. The findings of this research have practical implications for improving combustion efficiency and stability in aerospace applications. The optimized combustion processes and advanced diagnostic techniques developed through this study contribute to the design of more efficient and environmentally friendly propulsion systems.

The further objective is to conduct chemiluminescence measurements and simulations of CH^*/OH^* radicals for liquid fuel, validating combustion mechanisms and integrating findings with other diagnostic methods. The application of chemiluminescence techniques provides a powerful tool for probing flame chemistry and validating theoretical combustion models. By integrating these measurements with other diagnostic methods, the research enhances the overall understanding of flame chemistry, leading to more accurate simulations

and predictions of combustion behavior. This contribution is essential for advancing both experimental and computational studies in combustion science.

Furthermore, future implementations of this research include exploring the application of the developed algorithm and diagnostic techniques to other types of liquid fuels and combustion systems. This includes extending the methodologies to biofuels and alternative energy sources, thereby broadening the impact of the research on sustainable energy solutions. Additionally, the integration of advanced computational fluid dynamics (CFD) models with experimental data can further refine predictive capabilities, leading to more precise control over combustion processes.

Another future direction is the application of the developed techniques in industrial combustion systems, such as power plants and internal combustion engines, to enhance efficiency and reduce emissions on a larger scale. Collaborations with industry partners could facilitate the transfer of these technologies from the laboratory to real-world applications, driving innovation in combustion engineering.

This research advances the understanding of liquid fuel combustion processes and offers practical implications for improving combustion efficiency and stability in aerospace applications. The research advances diagnostic methods in combustion science, providing more accurate tools for studying flame structures and dynamics. The findings pave the way for future studies and innovations in diagnostic techniques and combustion system design, contributing to the broader field of fluid dynamics and combustion science. The insights gained from this research support the optimization of combustion processes for both prevaporized and spray liquid fuels. The continued exploration and development of these techniques promise significant advancements in both academic research and practical applications in the energy and aerospace sectors.

1.4 Outline of Dissertation

The chapters of this thesis delve into the study of liquid fuel flame topologies through the application of novel diagnostic techniques, addressing the complexities of liquid fuel combustion in various contexts.

Chapter 1 introduces the motivation behind studying liquid fuel flame topologies, outlining the research objectives and significance. This chapter provides an overview of the challenges in liquid fuel combustion and the need for advanced diagnostic techniques to enhance our understanding.

Chapter 2 details the experiments and methodologies employed in this study. It introduces the experimental setup, validation procedures and explains the data collection and analytical methods used. The chapter also covers the diagnostic tools such as Laser-Induced Fluorescence (LIF), high-speed imaging, and chemiluminescence, along with the experimental protocols for both prevaporized and spray liquid fuels.

Chapter 3 focuses on prevaporized liquid fuels, examining their characteristics and flame topology. It presents the diagnostic findings related to flame stability and extinction events and discusses the results in the context of theoretical models and combustion efficiency implications.

Chapter 4 explores spray liquid fuels, analyzing the interaction of droplets with the flame and the resulting fragmentation and vaporization. This chapter highlights the diagnostic findings on flame stabilization and quenching and provides a comparative analysis with prevaporized fuels, emphasizing the impact of turbulent flow conditions.

Chapter 5 investigates the application of chemiluminescence in studying liquid fuel flames. It elucidates the fundamentals of chemiluminescence in combustion and its role in validating combustion mechanisms proposed by other researchers through quantitative analysis. The chapter discusses the advantages and limitations of this technique, as well as its integration with other diagnostic methods.

Finally, Chapter 6 summarizes the key findings of the research, discussing the implica-

tions for future studies and practical applications in the aerospace industry and combustion system design. It concludes with reflections on the research contributions and potential directions for further investigation.

1.5 Summary

The introduction of this dissertation emphasizes the significance of understanding turbulent flame structures in heavy hydrocarbon liquid fuels, particularly for aerospace applications like gas turbines. The research aims to fill the knowledge gaps in liquid fuel combustion by developing and applying advanced diagnostic techniques to study the complex interactions between liquid droplets and flames.

The importance of liquid fuel combustion is highlighted, focusing on the challenges posed by the interactions between liquid droplets and flames and the limitations of existing diagnostic methods. This research is motivated by the need to better understand turbulent flames and improve diagnostic accuracy, seeking to capture flame structures and interactions more precisely.

The significance of this research lies in its contributions to developing more efficient and environmentally friendly combustion technologies by advancing diagnostic techniques and improving the understanding of flame dynamics. The findings support optimizing combustion processes for both prevaporized and spray liquid fuels, contributing to designing more efficient and stable combustion systems.

Furthermore, this research suggests potential future directions for further investigations, including applications to other fuel types and integration with computational models for better control over combustion processes. This study's advancements in diagnostic methods and understanding of liquid fuel combustion processes offer practical implications for improving combustion efficiency and stability in aerospace applications, paving the way for future studies and innovations in the broader fluid dynamics and combustion science field.

Chapter 2

Experiments & Methodology

2.1 Introduction

In this chapter, I will detail the experimental procedures chosen to study the turbulent flame structures of pre vaporized and spray liquid fuels. Each experiment's conditions and the diagnostic techniques implemented are explained in detail to provide a comprehensive understanding of the methodologies used. The major objective of this chapter is to introduce and devise a novel numerical algorithm designed to decipher intricate turbulent flame structures. This algorithm focuses on capturing and calculating flame edges, and relevant statistics, thereby providing valuable insights into the dynamics of liquid fuel combustion. This foundational work sets the stage for the subsequent analysis and interpretation of data, which are crucial for advancing our understanding of flame behavior in turbulent conditions.

2.2 Diagnostic techniques

Diagnostic techniques in combustion are essential tools for understanding and analyzing the complex processes that occur during the combustion of fuels. These techniques provide valuable insights into the chemical and physical phenomena that govern flame behavior, including species concentration, temperature distribution, pressure dynamics, and

overall thermal efficiency. The ability to accurately monitor and measure these parameters is crucial for optimizing combustion systems, improving fuel efficiency, reducing emissions, and advancing our fundamental knowledge of combustion science.

One of the most widely used diagnostic techniques in combustion research is Planar Laser-Induced Fluorescence (PLIF). PLIF is renowned for its ability to provide high-resolution, two-dimensional images of chemical species within a flame. By exciting specific molecules with a laser and capturing the resultant fluorescence, researchers can visualize the spatial distribution of key intermediates and reaction products. This technique is particularly useful for studying flame structure, turbulence-chemistry interactions, and pollutant formation processes.

Another powerful diagnostic method is chemiluminescence, which involves detecting the light emitted by excited species as they return to their ground state. Chemiluminescence is a relatively straightforward technique that can be used to evaluate the presence and concentration of intermediate species such as CH^* , OH^* , and C_2^* . These species are often indicators of important combustion reactions, and their detection provides critical information about flame stability, ignition processes, and reaction kinetics.

In addition to PLIF and chemiluminescence, several other diagnostic techniques are commonly employed in combustion studies. These include laser-induced incandescence (LII) for soot measurement, tunable diode laser absorption spectroscopy (TDLAS) for species concentration and temperature measurement, and particle image velocimetry (PIV) for flow field visualization. Each of these methods offers unique advantages and can be tailored to specific research objectives.

The combination of these diagnostic techniques in combustion research allows for a comprehensive analysis of flame behavior and combustion dynamics. By combining multiple methods, researchers can obtain a more complete picture of the complex interactions occurring within a flame, leading to more accurate models and better-engineered combustion systems.

In this chapter, I will go through the principles and applications of PLIF and chemi-

luminescence, the two primary diagnostic techniques utilized in our studies. I will discuss their implementation in our experimental setups, the advantages they offer, and the specific insights they provide into the turbulent flame structures of prevaporized and spray liquid fuels. Through this exploration, I aim to highlight the critical role of advanced diagnostic techniques in advancing combustion science and technology.

2.2.1 Chemiluminescence

There are several different methods in optical procedures, and chemiluminescence is one of them. Chemiluminescence is the light emitted from a chemical reaction. An excited intermediate species with high energy to reach a stable state releases its energy as photons of light. The chemiluminescence light emitted by the flame is well suited for diagnostic purposes.

Chemiluminescence is used to obtain information in the reaction zone related to combustion performance, species formation, quenching, and emission. This method has been widely used to measure equivalence ratio, heat release, flame front location, and other potential information that can illustrate combustion conditions. One of the most significant advantages of chemiluminescence is that it is much cheaper than other measuring methods in combustion, and it is way more accessible.

Unlike laser diagnostic or other methods, chemiluminescence does not need an external source for light since this process emits light during species formation by heat release. This emitted light is used as a diagnostic measurement since it has information about the local combustion processes. Flame chemiluminescence has been employed in various combustion applications, from simple Bunsen flames to full-scale gas turbine engines, as a diagnostic tool. Flame chemiluminescence is a well-established diagnostic in gaseous flames, and its behavior has been represented in several simulations [Nori and Seitzman, 2009, Panoutsos et al., 2009]. Due to adverse circumstances for laser diagnostics or restricted optical access in complicated turbulent flows, chemiluminescence is sometimes the only experimental diagnostic available.

Chemiluminescence imaging is frequently utilized as a validation and comparison metric for mathematical models [Hossain and Nakamura, 2014]. The most important species

to be investigated in the combustion process are OH, CH and possibly CO_2 . By measuring these species, this method is capable of evaluating equivalence ratio sensing [Hardalupas and Orain, 2004], heat release [Guyot et al., 2010], and marking reaction zone [Guethe et al., 2012]. There is a different approach to this investigation, such as numerical modeling or experimental research. It has been noted that the relative intensities of different species depend on the fuel equivalence ratios, pressure, strain, and performing conditions.

Several studies have been done in numerical and experimental methods to find the importance of species intensities and connect them to the conditions of systems. Knowing the mechanism of different species is the most crucial part of every chemiluminescence modeling. However, only methane oxidation processes have been used to analyze these sub-mechanisms in the past. Furthermore, chemiluminescence as a diagnostic tool for higher alkane species and kerosene fuels has not been adequately investigated. As shown in Figure 2.1, the real problem is the spectroscopic balance between the genuine chemiluminescence signal from the species of interest and a wideband background pedestal attributable to CO_2 [Lauer and Sattelmayer, 2010]. In methane flames, the ratio between these two species has fluctuated as a function of the equivalence ratio [Nori and Seitzman, 2008]. When most of the chemiluminescence signal is due to the background elevation rather than the CH, C_2 , or OH species, which have been linked to flame performance, the issue arises of what is being photographed. This study, which is the second part of the study, includes the experiment results to evaluate the mechanisms and modeling. These models will investigate kerosene fuels' performance, allowing for correlations between experimental results and combustion simulations. Nori and Seitzman [Nori and Seitzman, 2009] studied many aircraft kerosene fuels, including Jet-A, surrogates, and JP-8.

Several main mechanisms and sub-mechanisms are used to calculate main species and intermediate ones. Most chemiluminescence physics and kinetics are validated for methane with GRI Mech 3 [Smith et al., 2011] mechanism. For n-Heptane and n-Dodecane, the JetSurF2.0 [Wang et al., 2010] mechanism has provided detailed formation and quenching

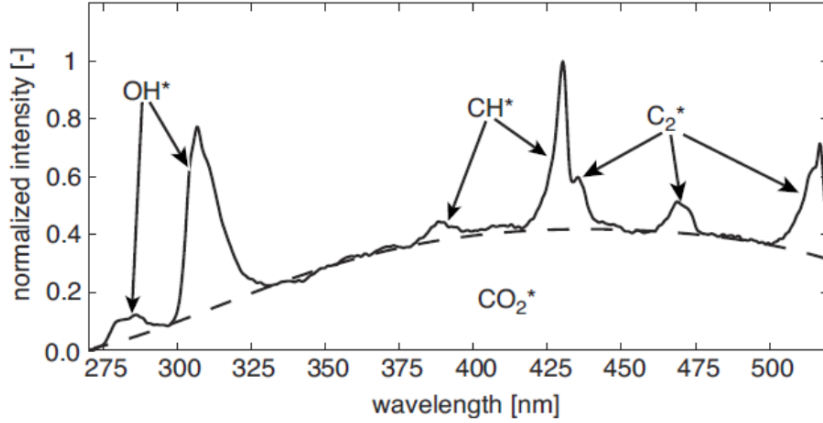


Figure 2.1: Chemiluminescence spectrum of a methane-air flame. The radical emissions from OH^* , CH^* , and C_2^* are superimposed by the broadband pedestal from CO_2^* [Lauer and Sattelmayer, 2010]

reactions with a built-in sub-mechanism to calculate CH and OH. JetSurF2.0 consists of 348 species and 2163 reactions.

The development effort centers on n-Dodecane and n-butyl-cyclohexane. However, the model also includes the high-temperature chemistry of all n-alkanes up to n-Dodecane. HyChem [Wang et al., 2018, Xu et al., 2018] is a detailed high-temperature mechanism that includes seven reaction steps to describe JP-8 POSF10264 thermal decomposition and USC Mech IIa as the foundational fuel chemistry model. The cracked products considered are C_2H_4 , H_2 , CH_4 , C_3H_6 , $1-C_4H_8$, $i-C_4H_8$, benzene, toluene, CH_3 . The chemiluminescence sub-mechanism requires formation reaction, quenching, and relaxation reactions and their constant rates to simulate CH and OH emissions. The main formation reactions for CH and OH are as follows:



Several reactions in the quenching and relaxing processes should be addressed and

considered. These mechanisms and sub-mechanisms will be addressed later in the Chemiluminescence chapter. Since radicals have a slow formation rate and a quick rate of elimination and quenching, they have a low concentration in flames. The concentrations were measured as a post-process to the flame modeling and were considered in a quasi-steady state with no impact on the overall kinetics. The formation and removal quenching reaction rates can be used to determine the concentration of species. The concentrations of CH(moles/cm³) and OH can be calculated using the equations below:

$$[CH^*] = \frac{k_1[C_2H][O] + k_2[C_2H][O_2]}{\sum_j k_{Q,j}[M_j] + A_c} \quad (2.4)$$

$$[OH^*] = \frac{k_3[CH][O_2]}{\sum_j k_{Q,j}[M_j] + A_c} \quad (2.5)$$

Where K1 and K2 are the reactions constant rates for two formation reactions (R1 and R2), k_{Q,j} is the quenching rate constant by the species j, and A_c is the Einstein coefficient for spontaneous emission. K3 is the constant reaction rate for formation reaction R3. The photon emission rate, i (mole photon, cms) is calculated by:

$$i_{CH^*} = A_c[CH^*] \quad (2.6)$$

$$i_{OH^*} = A_c[OH^*] \quad (2.7)$$

The profiles through the 1D simulation are integrated to calculate the full spatial formation of each species, I_{CH} (Photons, cms), where L is the integration path length across the 1D domain:

$$I_{CH^*} = \int i_{CH^*} dx \quad (2.8)$$

The total emission rate P (Photons/sec), is given by the flame area and can be derived by:

$$P_{CH^*} = I_{CH^*} \times A_f = I_{CH^*} \frac{m}{\rho u S_L} \quad (2.9)$$

Chemiluminescence studies on the characteristics of spectral emission of kerosene have been done by Lee [Lee and Seo, 2015]. Intermediate species of CH, OH, and C₂ were investigated for the flame of a swirl combustor. They expressed that the high luminosity of kerosene is due to a high attribution of background CO₂ chemiluminescence. Additionally, OH and CH showed similar behavior as a function of equivalence ratio: as the equivalence ratio increased, both CH and OH chemiluminescence intensities decreased. However, the C₂ chemiluminescence was affected by changes in the equivalence ratio. In rich combustion conditions or with higher inlet temperature, the C₂ intensity increased. Finally, they found a correlation between the ratio of CH/OH and the equivalence ratio.

Chemiluminescence and simulation of CH/OH for liquid fuel require detailed reaction mechanisms which depend on the fuels, temperature, and pressure. Due to the complexity of liquid fuel simulation, it is common to use gaseous fuel simulation results to estimate the CH/OH species in liquid fuel combustion.

Comparisons with experimental chemiluminescence measurements will determine the optimal scale for model validation. Experimental measurements are required to determine which sub-mechanisms provide correct predictions. Experiments validate modeling attempts for scaling CH and OH species for varied operating circumstances.

2.2.2 Laser Induced Fluorescence

2.2.2.1 LIF Concept

Laser-Induced Fluorescence (LIF) is the optical emission from molecules or atoms that have been excited by an external source of electromagnetic radiation. To understand fluorescence thoroughly, it is crucial to study the energy states and electronic transitions in molecules. Typically, molecules are in their ground state, the lowest energy state. When a tunable laser illuminates the flow, it overlaps an allowed electronic, vibrational, or rotational

transition in an atom or molecule. The molecule undergoes electronic excitation upon absorbing light, moving to a higher energy state. This state, known as an excited electronic state, depends on the number of absorbed photons and the resulting energy level.

After excitation, the molecule may undergo vibrational relaxation within the excited state, releasing excess energy through non-radiative processes. This process brings the molecule to the lowest vibrational level of the excited state. The excited molecule then undergoes a radiative transition, or fluorescence emission, returning to the ground state. During this process, the excess energy acquired during excitation is emitted as a photon with lower energy than the absorbed photon. This emission of photons from a higher energy state is termed fluorescence.

To advance deeper into molecular energy transitions and their relation to fluorescence emission, it is important to understand the various types of transitions in molecules, each associated with changes in their energy levels. The three main types of transitions are electronic, vibrational, and rotational. These transitions determine how molecules interact with each other and influence their bond lengths.

Electronic transitions involve changes in the electronic energy levels of a molecule, where electrons move between different electronic states, such as from the ground state (e.g., labeled X) to excited states (e.g., labeled A, B, C). The energy associated with electronic transitions is often in the ultraviolet (UV) or visible range.

Vibrational transitions involve changes in the vibrational energy levels of a molecule. As atoms within the molecule move relative to each other, the molecule vibrates. Transitions between vibrational states are associated with changes in these vibrational motions. The energy associated with vibrational transitions is generally lower than that of electronic transitions and falls in the infrared (IR) range. Vibrational levels are usually denoted by "v".

Rotational transitions involve changes in the rotational energy levels of a molecule. Molecules can rotate around their axes, and transitions between rotational states are associated with changes in rotational motion. The energy associated with rotational transitions is

lower than both electronic and vibrational transitions and typically falls in the microwave range. Rotational levels are usually denoted by "J".

Transition selection rules are principles that govern which transitions are allowed or forbidden in a molecule. These rules help predict and understand the spectra observed in various spectroscopic techniques. At room temperature, typically only the lowest energy vibrational state ($v = 0$) is populated, so $v_0 = 0$ and $\Delta v = 1$ are common transitions. States with $J \neq 0$ can be populated since they represent the fine structure of vibrational states and have smaller energy differences than successive vibrational levels. Additionally, $\Delta J = 1$ because a photon contains one quantum of angular momentum, adhering to the principle of conservation of angular momentum.

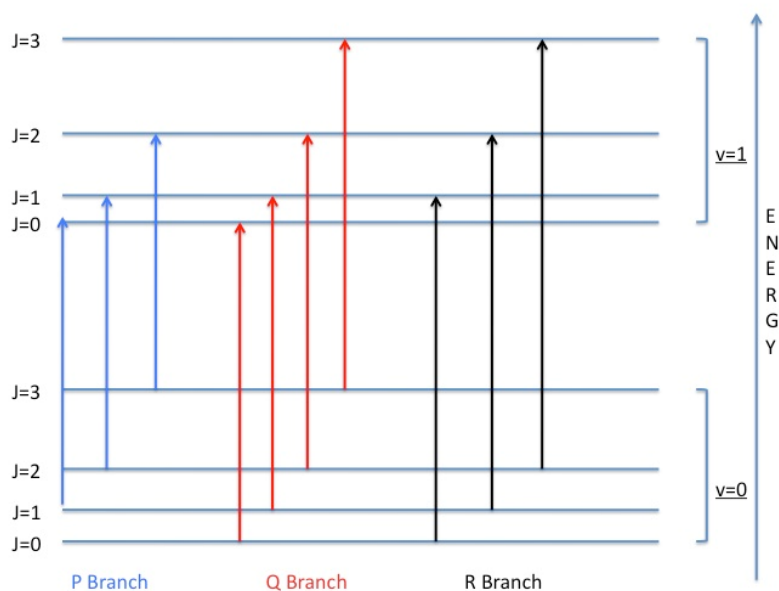


Figure 2.2: Diagram of P,Q, and R branches transitions

For diatomic molecules, the transition $\Delta J = 0$ (i.e., $J'' = 0$ and $J' = 0$) with $v_0 = 0$ and $\Delta v = +1$ is forbidden, so pure vibrational transitions are not typically observed. The rotational selection rule gives rise to an R-branch (when $\Delta J = +1$) and a P-branch (when $\Delta J = -1$). Each line of the branch is labeled $R(J)$ or $P(J)$, where J represents the value of the lower state. The R-branch transition occurs when $\Delta J = +1$, where the rotational

quantum number in the excited state is one more than in the ground state. The P-branch transition occurs when $\Delta J = -1$, where the rotational quantum number in the excited state is one less than in the ground state. The Q-branch transition occurs when $\Delta J = 0$, where the rotational quantum number remains the same in both states. These branches are presented in Figure 2.2.

2.2.2.2 LIF application in combustion

LIF is a unique and valuable method for measuring variables or visualization. It can be implemented to measure various data such as density, concentration, velocity, temperature, and pressure. It can be used at a single point, line, or even a sheet called PLIF. LIF is a resonant technique requiring the laser to be tuned to a specific wavelength. Single-photon LIF is linear, but it can have a low signal that requires ICCD to intensify the signal, but on the other hand, it increases the noise level. LIF method differs for the liquid phase and gaseous phase. For the liquid phase, fluorescent particles are seeded with the flow, and by absorbing energy and releasing it, measurement of concentration and temperature. While performing in the gaseous phase, the seeded particle is not proper since the species have a unique excitation wavelength. The illuminating part is not just due to the particles. For gas, a phase-specific wavelength for tuning laser is needed to excite a specific species, and that excited species will release photons after relaxation.

In the combustion study, OH is excited in the UV near 282nm for (1,0) or 306nm for (0,0). OH PLIF produces a high signal due to the abundance of OH, and it can be used as a marker for product and turbulent transport. On the other hand, CH is excited in the UV/vis near 390 nm for B-X¹, 413 nm for A-X², and 314nm for C-X. CH PLIF can identify the flame front in premixed flame, and it can identify the stoichiometric surface in non-premixed flame.

The study of turbulent flame topology has grown drastically recently, and quantifying

¹Transition from second excited electronic state to ground electronic state

²Transition from first excited electronic state to ground electronic state

flame features is of great use to associate with direct numerical simulation (DNS). One of the favored diagnostic techniques in combustion is CH/OH PLIF. Recent advancements in CH PLIF using C-X band transition have been applied in prevaporized and spray flames. Several features of flame structure can be measured with this method, such as flame front, flame curvature, flame surface density, and consumption speed.

Wang [Wang et al., 2019] studied turbulent liquid spray flame supported by pilot flame using OH LIF and CO PTLIF for the first time in shooting flames. A laser beam focused at 230 nm wavelength at two-photon LIF was used to excite the CO, and for OH PLIF, a laser beam at 282.75 nm wavelength was used for Q1 (5) rotational transition of OH radical excitation. OH PLIF results indicate that the reaction zone is located near the nozzle exit primarily, and it propagates uniformly by moving away from the burner since the droplets vaporized thoroughly. Analyzed data of CO TPLIF shows that near nozzle exit, a solid spectral line around 460 nm appears, which is due to C₂ Swan bands.

Heat release rate or flame burning rate is one of the characteristics that cannot be measured directly, and there are indirect measurements and correlations to predict it. HCO is the direct method and tracker of heat release rate, but it is hard to capture because of quenching and removal reactions. Since they have low concentrations in flames, it is hard to detect them by single-pulse measurements. However, Paul [Paul and Najm, 1998] utilized a new method for single-shot measurements to follow up on the heat release rate in flames. It is suggested that OH and CH₂O can be the species that can mark the heat release rate. They applied OH PLIF at 283 nm and CH₂O PLIF at 338.1 nm on a turbulent premixed dimethyl ether air V-flame vortex interaction and compared the results to a simulation outcome. It was observed that the OH surface was in contact with the CH₂O surface through the experiments, and the flame structure was hardly affected by the vortex interaction. It has been expressed that OH and CH₂O PLIF can single pulse measure the flame front and heat release rate.

Stabilization and flame structure in turbulent spray flame has been investigated by Stepowski [Stepowski et al., 1994]. Flame of atomized methanol liquid mixed with flowing air

through a duct has been studied by OH LIF measurement, and velocity distribution has been captured with the PDV³ method. The laser was pumped at the wavelength of 283.93 nm, and detection occurred at 315 nm. Although an elastic scattering of laser has been neglected by using a high pass filter, it cannot avoid big methanol droplets of Raman scattering around 309 nm which can be detected as saturated signal regions of white circles. Figure 2.3 shows flame structure at different velocities of fuel air mixtures to measure the lift off location and evaluate the effect of methanol droplets on the flame structure. Methanol droplets have caused discrete regions in the LIF result. Also, they stated that by increasing flow velocity, the lift off location increases which may affect the flame stabilization.

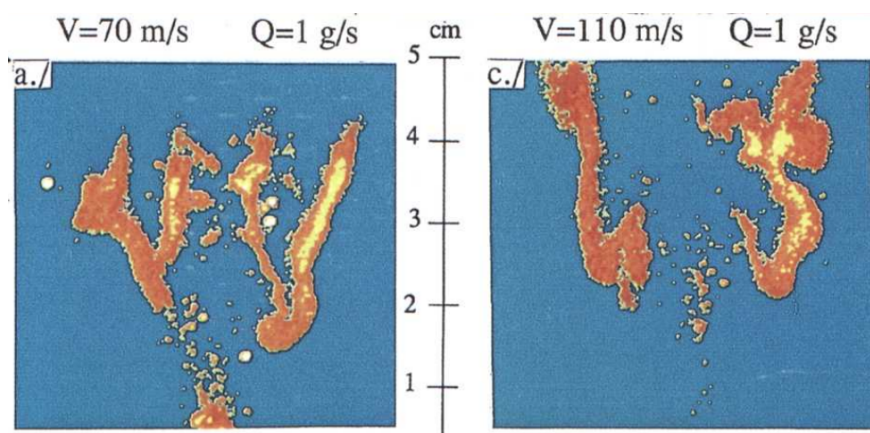


Figure 2.3: OH LIF in spray liquid flame for two different velocity and appearance of discrete region in spray axis due to large droplet scattering [Stepowski et al., 1994]

CH radical is formed within the reaction zone; therefore, it is the flame front marker. The extinction and penetration of pockets within reactants are possible by studying CH. However, due to the low concentration of CH and interference of other species, fluorescence signal detection of CH is low.

The simple approach to capturing CH radicals is to excite them via A-X and B-X bands near 340 nm by higher energy. However, by increasing the energy of the pulse of the beam, other species, such as PAH and OH, will excite as well. Since their absorbance coefficients at CH excitation wavelengths are not zero, and the concentration of these species

³Photonic Doppler Velocimetry

is much higher than CH, they will interfere with the CH signal. On the other hand, liquid droplets in spray or prevaporized cases can absorb the energy and fluorescence at a specific wavelength. This is known as the Mie scattering effect, which interferes with the CH signal.

Carter [Carter et al., 2014, Carter et al., 2016] introduced a new approach in the CH PLIF experiment to overcome this problem. Instead of exciting CH at the A-X (1-0) band at a 430 nm wavelength, they excite CH in the range of 310-320 nm wavelengths via the C-X (0-0) band, where CH has higher signal detection. There are several OH transition wavelengths in this region, which can create some interference in the CH signal, as shown in Figure 2.4.

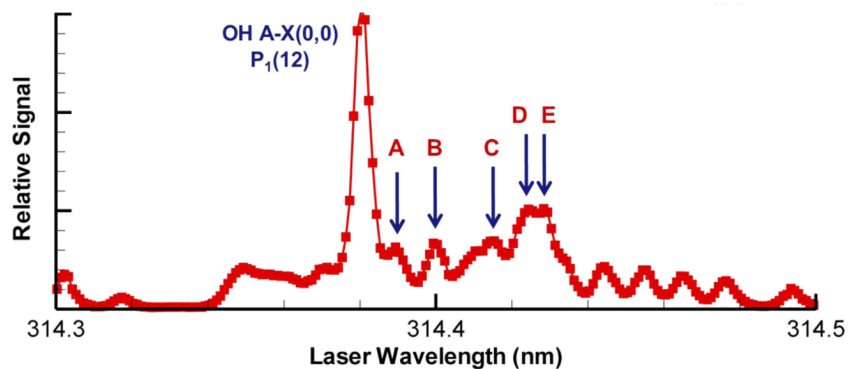


Figure 2.4: Detailed spectrum with inset images for specific wavelengths [Carter et al., 2016]

This interference can be avoided if only CH PLIF are desired. However, it poses the possibility of capturing simultaneous CH/OH PLIF with one camera and a single wavelength, as shown in Figure 2.5. The most prominent feature of this approach is that the excitation can be done with a small amount of laser energy, which makes high-speed imaging possible. Since the laser beam has low energy, the interference of droplet or PAH Mie scattering is minimized and neglected. As can be seen, there are three different regions: first, the reactant, which has minimal signal; second, the flame surface, which has the maximum signal; and last, the product, which has intermediate values of signals.

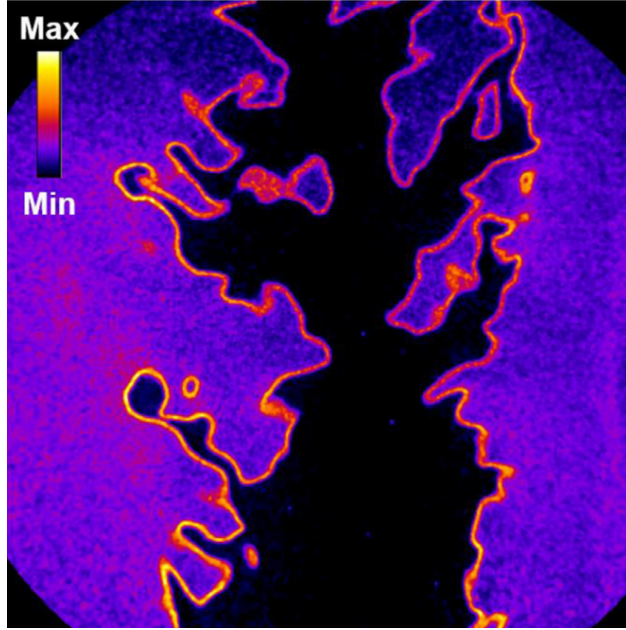


Figure 2.5: Combined CH-OH PLIF image from premixed turbulent Bunsen flame [Carter et al., 2016]

For liquid spray cases, the excitation wavelength differs compared to prevaporized studies. This idea was tested before by Hammack [Hammack et al., 2018] in turbulent liquid spray jet flame using Hi-Pilot burner. In this study, instead of exciting CH fluorescence at Q branches around 314 nm, the R-branches were chosen to excite the CH radicals. The main reason for this alteration is to avoid the interference of droplet Mie scattering by using a custom Semrock (AFRL 0002) and UG-5 filters. Figure 2.6 shows the transition wavelength spectroscopy in the R-branches region.

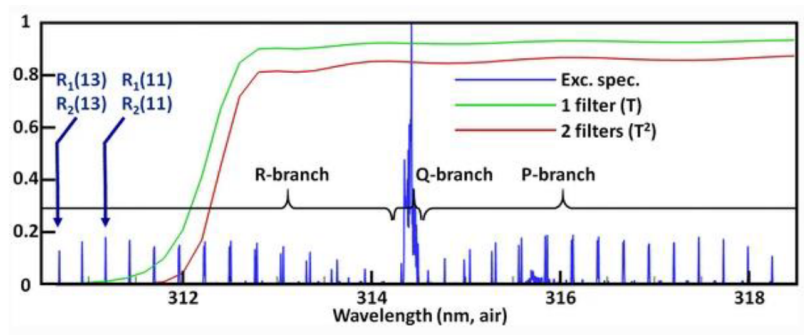


Figure 2.6: Excitation wavelength of CH in R-branches region [Carter et al., 2016]

The excitation occurs at 311 nm, where a UG5 filter around 311 nm is used to block the Mie scattering interference of liquid fuel droplets and components. However, since the filter does not completely block the fluorescence at 311 nm, two custom-made Semrock filters around 312 nm are used to improve rejection of droplet fluorescence signals. Another goal of this research is to compare CH PLIF and OH PLIF by studying flame surface structure like flame surface density. Compared to OH PLIF, where the product and reactant sides are oriented and distinguished, CH PLIF requires more detailed binarization and side detection processing due to flame fragmentation and local extinctions. Observations of simultaneous OH-CH PLIF in these flames often show layers of extinguished CH. At the same time, localized OH signal remains, which suggests the imaging of OH alone may not capture in-plane extinction and may lead to an over-prediction of flame surface density. In this study, to simulate OH PLIF and evaluate the overprediction, the edges of extinction areas in CH images are connected artificially. The flame surface is calculated separately for this pseudo-OH PLIF. Hence, the flame surface density, conditioned on the local progress variable, is calculated for all cases, comparing fueling effects and equivalence ratio. Lastly, to determine potential differences in imaging methodologies between the CH PLIF and OH PLIF, the flame surface density is measured for pseudo-OH PLIF and compared to the CH PLIF-derived measurements. CH and OH PLIF have their benefits and limits. CH PLIF depicts flame location [Smolke et al., 2018] and provides a two-sided flame structure, while OH PLIF is a marker of heat release location, and the flame structure is one-sided. The stream's orientation is known when OH PLIF is used, and the flame is divided into reactant and product. However, in CH PLIF, since the flame edges are captured, there is no distinguishable sign between reactant and product. CH PLIF can detect breaks and extinction in the flame, while OH PLIF is unable to detect it and produces a false flame edge. Overall, each method has its application based on these advantages and disadvantages. To study flame structures like flame surface density and curvature, OH PLIF is preferred. To research flame extinction and blow-off cases, CH PLIF is suitable.

2.2.3 Diagnostic Procedure

To capture the turbulent prevaporized flame structure, a CH PLIF experiment was conducted using the ($v'=0, v''=0$) band to excite CH species with a 10 Hz Nd: YAG laser at 314.4 nm. The CH PLIF method used in this experiment was previously introduced by Carter. The measurements were acquired at laser pulse energies of 1.3 mJ, which is in the saturated regime for this method. A cylindrical and spherical lens with 50 mm and 1000 mm focal lengths were employed to create the desired laser sheet. A PIMAX III intensified camera was used with a UV-Cerco 100 mm lens to visualize and capture the CH signal. In order to minimize the Rayleigh scattering, horizontal beam polarization is used. To obtain the ideal output, the settings of gain and gate were set to 51 and 250ns, respectively. Lastly, the observed field of view in this experiment was 35 x 35 mm, and the resolution was measured to be 34 microns per pixel. In order to capture liquid spray flame structure, a CH PLIF similar to prevaporized experiment was conducted. But instead of exciting the CH at CX Q-branch, the R-branch excitation was implemented. The excitation is around 311nm wavelength and to prevent the interference of Mie scattering fluorescence, two filters of UG5 and Semrock 0002 were installed in imaging equipment. The field of view in this experiment was determined to be 50 50 2 . By applying a binning process, the resolution of 49 /pixel was achieved. For CH and OH excitations, the amount of laser energy was recorded as 1-2 mJ/pulse and 3-4 mJ/pulse, respectively.

2.3 Image processing

CH radical, which is known as a flame surface marker and is formed within the flame reaction zone, has been used to identify turbulent topological features such as the formation of pockets and holes [Rosell et al., 2017, Li et al., 2010]. Tracing the CH radical can lead to identifying local extinction, and it is not transported from the reaction zone [Smolke et al., 2018]. CH and OH PLIF images have been used to measure turbulent flame features such as curvature, surface density, and consumption speed [Driscoll, 2008, Zhang et al., 2020]. But

when using only CH PLIF, the information of product zones extracted from the OH PLIF is missing. So, problems such as curvature sign, flame breaking, or extinction, etc., appear in these cases where only CH PLIF is provided.

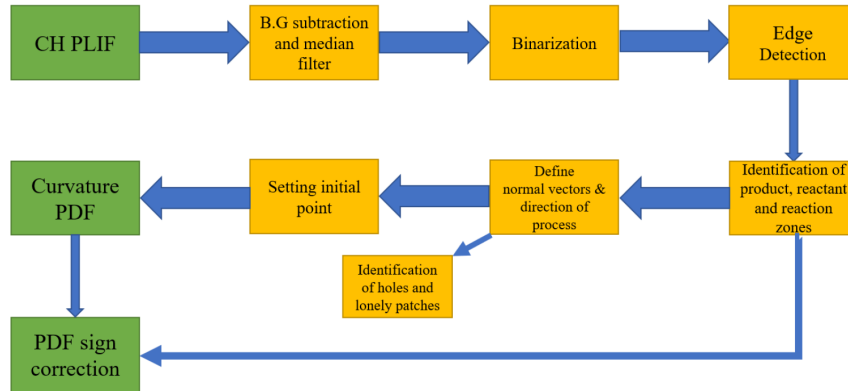


Figure 2.7: Flow chart of image processing in this method

As shown in Figure 2.7, the flow chart of the presented method is briefly explained. First, CH PLIF images (Figure 2.8a) are processed through background subtraction and noise elimination to start the logic behind this method. A 3x3 pixel square median filter is also applied to reduce the noise. The images are binarized using Otsu's method [Otsu, 1979]. Using Otsu's method, the CH PLIF image becomes a matrix of 0 and 1, where the number 1 indicates that a pixel is within the reaction zone and number 0 means that the pixel is either in the product or reactant region (Figure 2.8b). Then, by applying a gradient to the binarized images, it can identify the inner and outer surfaces of the flame. Using the gradient over the binarized image, the outcome shows either 0, +1, or -1 1/pixel.

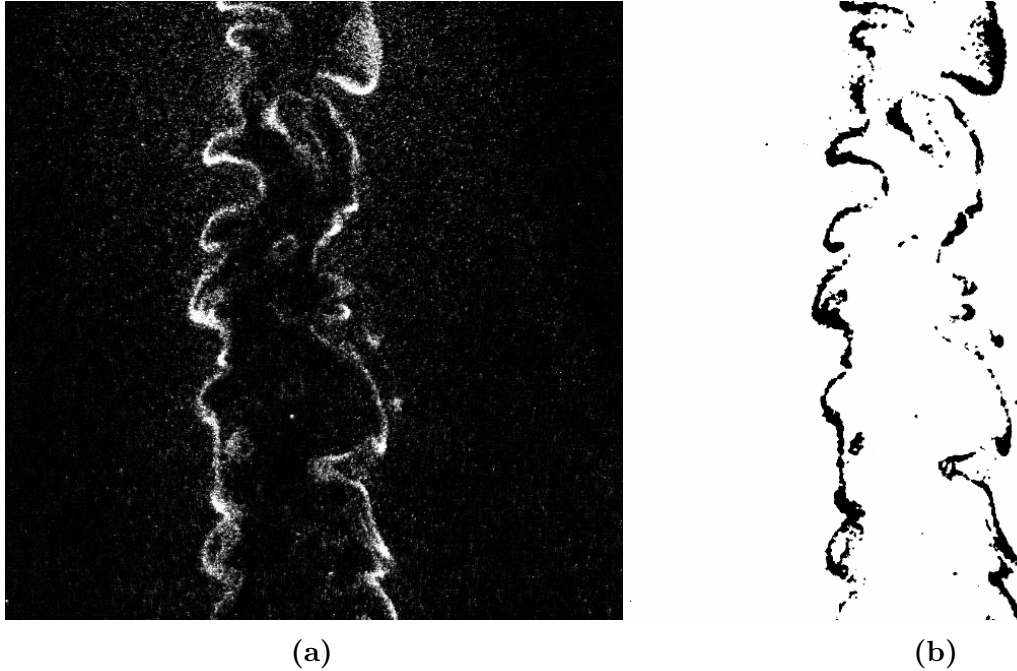


Figure 2.8: (a) Original raw and (b) binarized images for turbulent $Re = 10,000$, at equivalence ratio $\phi = 1.2$ of n-Heptane flame at 35 mm height above the burner with 60 m/s pilot flame

Now, by setting a reference point at the centerline of the image close to the burner exit, which indicates the reactant region, and moving through the gradient of the binarized image, it can identify all of the regions, such as reactants, products, and flame. For example, if the start point is in the reactant region where the value of the binarized signal is zero and the direction of movement is known, as long as the gradient value stays zero, it means the region is still reactant. And by seeing a difference in gradient, the reaction zone is identified. All image processing and coding were developed and done in MATLAB R2018a and its image processing toolbox.

The next step is to assign reaction zones, or what is used to call from now on, families. For this purpose, it has to detect the edges of the flame and then define families. The edges of the flame are easily known by searching through the binarized image. After that, to assign families, it first sets those points and searches for their neighbors with a value of 1 (since the image is binarized). If none of the neighbors have the value of 1, then this family is done,

and it looks for the next points and assigns another family. By repeating this procedure, it divides the whole flame into various reaction zones and applies the image processing to these zones or families. However, to eliminate noise and error, a threshold value for several points to consider them a family is set. The threshold value is arbitrary as long as it can be assumed that the number of points forms a reaction zone. Based on our observation through various images, the value of 40 points is considered the threshold value. Figure 2.9 shows a sample of families detected using this method.

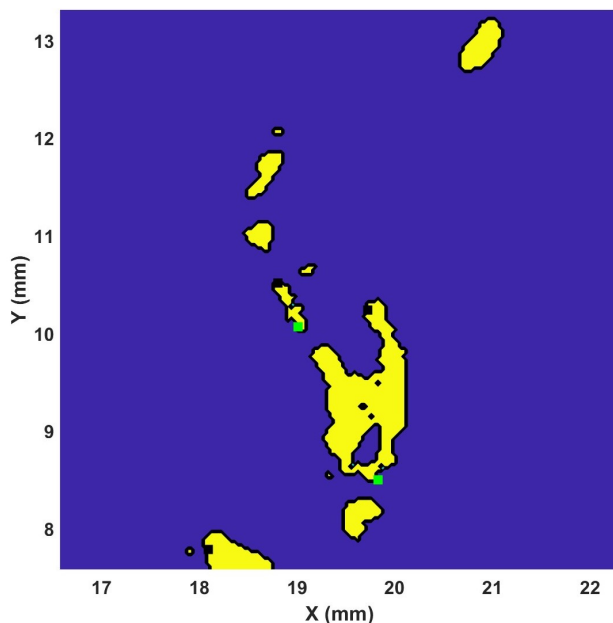


Figure 2.9: Families identified for turbulent $Re = 10,000$, at equivalence ratio $\phi = 1.2$ of n-Heptane flame at 35 mm height above the burner with 60 m/s pilot flame

The main problem in the current image processing and curvature calculation is the correct sign of the curvature since the information regarding the orientation relative to the reactant or product stream, which determines the sign of the curvature, is not known. As shown in Figure 2.10, normal vectors to the family's surface are used as a guideline for knowing the direction of movement in the flame surface, and in further steps it is used to find pockets of reactant and products in the reaction zones. Also, this is a good approach to avoid any miscalculation and it is a starting point to identify the sign of curvature, and this technique is similar to other research in this area [Haq et al., 2002, Kim and Pitsch,

2007, Falkenstein et al., 2020]. To make sure that all of the vectors are towards the outside of the surface, the method uses the normal vector to make a surface parallel to our original surface. If the values of the binarized image in that new surface were zero, it means it is outside of the flame. Vice versa, if the value of the new surface is 1, it means it is inside of the flame surface and it has to correct the normal vector.

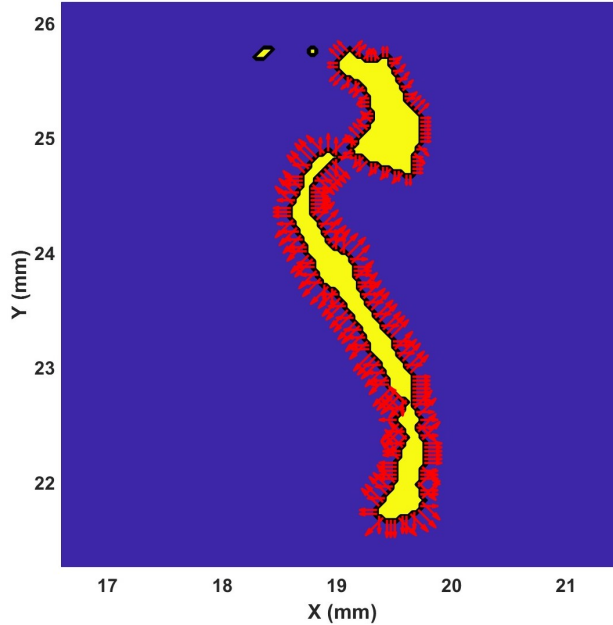


Figure 2.10: Normal vectors defined for a small segment of the binarized image for turbulent $Re = 10,000$, at equivalence ratio $\phi = 1.2$ of n-Heptane flame at 35 mm height above the burner with 60 m/s pilot flame

To identify holes or product/reactant pockets and reaction zones, based on the observation, using the normal vectors seems to be a good idea. First, it's necessary to locate the center of gravity of the family by taking the mean values of the family's points x and y coordinates. Then, using that center of gravity as a reference point, calculate the angle between two vectors. The first vector is the line going from the reference point to a point on the family surface, and the second vector is the normal vector at that point. To measure the angle between two vectors for each point, the following equation can be used:

$$\theta_i = \cos^{-1} \left(\frac{\mathbf{r}_{g,i} \cdot \boldsymbol{\eta}_i}{|\mathbf{r}_{g,i}| |\boldsymbol{\eta}_i|} \right) \quad (2.10)$$

Where η_i is the normal vector on the i th point of the family and $\mathbf{r}_{g,i}$ is the vector from the gravity point.

If the average of these angles for a family member is between 90 and 270, then that family has a product/reactant pocket or hole in itself; otherwise, that family is a reaction zone of the flame. For now, the holes are filled and excluded from our calculation, and curvature is not calculated on the hole surface. This method lacks in detecting whether the hole or pocket is reactant or product, and so the sign of curvature is not determined on these regions based on it.

The next step is to find the edges of each family and use them as initial points for each one. These edges are used as initial points to start the calculation of curvature and move clockwise with the help of normal vectors until reaching the other edge point or the last one, then start over from the last point to the initial point. To find the edges of the families, the skeleton of the families is extracted using the longest distance between the edges and branches to eliminate small and unnecessary ones. Another alternative idea is to measure the curvature on the skeleton branches; however, it may not be representative of the whole flame.

The final step is to derive the curvature value from the flame surfaces and edges. The following equation is used to measure the curvature, which is an improvised version to have better results. In this equation, the s parameter is the length of the flame alongside the initial point that has been chosen.

$$H = \sqrt{\left(\frac{d^2x}{ds^2}\right)^2 + \left(\frac{d^2y}{ds^2}\right)^2} \quad (2.11)$$

It's important to mention that this approach is specifically devised for the prevaporized liquid fuel flame structure near the base of the burner, where there is no sign of fragmentation or global extinction. However, the behavior of the flame changes significantly at higher axial locations. In the middle section of the flame, fragmentation occurs due to increased turbulence and interaction with surrounding air, requiring a different algorithm to accurately model and

address these phenomena. Similarly, at the tip of the flame, global extinction happens because of the limited fuel supply and the mixing dynamics, necessitating yet another specialized algorithm to handle these challenges. The next section delves into these additional algorithms, providing detailed solutions for managing the distinct behaviors observed in various parts of the flame.

Since the flame edge can be affected by high-frequency digital imaging, some sort of smoothing is required [Haq et al., 2002, Chen, 2007]. The Savitzky-Golay [Savitzky and Golay, 1964] algorithm, which is a low-pass filter, is used on the flame edges to smooth them and improve the procedure of calculation. This equation is a positive analytical value which needs to have a sign due to being convex or concave toward the reactant or products. Positive curvature flames are convex toward the reactant, or they are concave toward the product. These flame surfaces are curved outward, toward the reactant. The negative curvature flames are concave toward the reactant, or convex toward the product. These flame surfaces are curved inward, toward the products. The method sets the initial points on the outer surface of each family, and also every region's identity is known. So, a correction factor is assigned to the final results to identify the sign of positive or negative of the curvature.

It should be noted that, to have improvements in our calculations, an interpolation is applied to the points of the families. The rate factor of interpolation is 2, which means the number of points is doubled and between each two points, a new point is introduced and gets the average value of the two points. Also, a wavelet noise eliminator was applied to the calculation to smooth the flame edges even more and decrease the effects of digital imaging. With a greater number of points and smoother paths, higher accuracy and lower error in the calculation of curvature is achieved.

According to the study, the highest detectable curvature is 5000 1/m, which corresponds to a circle with a radius of 0.2 mm. The CH layer thickness limit predicted by the CHEMKIN simulation is likewise approximately 200 microns [McManus et al., 2021].

2.3.1 Spacial Case Algorithms

Here I try to categorize different flame structures and explain why each one of them requires a special algorithm to overcome the complexities and difficulties of their nature. Based on the field of view and how turbulent flame is captured, I can divide them into three different categories. First, the base of the burner which has been explained in the previous section. The second part is the middle section where the initial fragmentation happens and the flame divides into two parts. And lastly, the tip of the flame where the flame begins to break into small fragments and global extinction occurs. I try to come up with a unique algorithm for each case. Also, a separate individual algorithm is provided for spray liquid flame structures.

2.3.1.1 The Middle Section of The Flame

This section addresses the part of the flame where the first major fragmentation occurs, causing the main jet flame to break due to local extinction when it comes into contact with the surrounding air. To resolve the flame edge detection for this section, it is crucial to locate the breaking or fragmentation point. Most of the steps are similar to the main algorithm up to the point of connecting the reaction layers' endpoints. Our goal is to identify the breaking point and categorize the flame patches or reaction layers into two groups: one before and one after the breaking point. I then apply the previous algorithm, used for the base of the burner, to these two sections. Based on our observations, almost all fragmentation starts in the upper half of the flame, at a higher axial location compared to the center point of all patches. Additionally, most of these fragmentations can be identified by the angles they form with the center point. By restricting the patches to those whose endpoints form an angle between 60 degrees and 120 degrees, I can isolate the reaction layers that are at a higher axial location than the breaking point.

Next, I sort all the patches below the breaking point and designate them as Group A. I then identify the point with the maximum axial coordinate within Group A and use this

maximum point to determine which of the remaining patches belong to Group A.

For the other patches that are not yet sorted, I compare their endpoints to the maximum point individually. If the distances from both endpoints to the maximum point are greater than 50 pixels, these patches are labeled as Group B, which are considered the flame patches above the breaking point. Otherwise, they are included in Group A. This iterative process continues until all patches are designated as either Group A or Group B.



Figure 2.11: Rprevaporized n-dodecane at the middle section with a Reynolds number of 10000

Figure 2.11 displays a sample image of prevaporized n-dodecane in the middle section with a Reynolds number of 10,000. In this image, the reaction zones above the breaking point have been identified and isolated. Figure 2.12 illustrates the differences between application of the original base of the burner algorithm and the current algorithm to the images from the middle section. This approach prevents the omission of flame edges detected by the previous algorithm and ensures accurate assignment of regions to products or reactants.

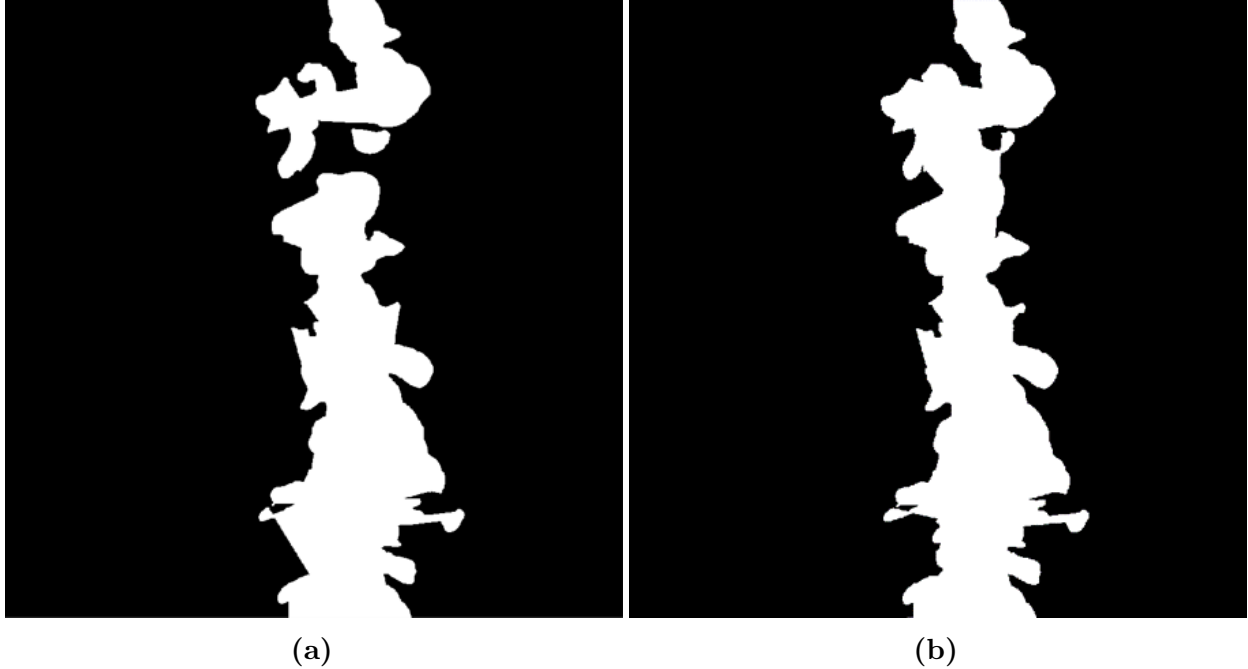


Figure 2.12: Product and reactant regions detected by (a) special algorithm for the middle section of the flame, (b)base of the burner algorithm

2.3.1.2 The Tip of The Flame Case

The final part of the flame that requires a specific algorithm due to its complex structure is the tip of the flame, where multiple small fragmentations are present. This field of view usually consists of two parts: the remaining portion of the middle section flame and multiple isolated small patches. To organize them, I must identify and exclude all small reaction layers that are no longer part of the main flame. By excluding these parts, only the main flame patches remain, which can then be processed by the previous algorithm to effectively connect the edges.

To determine if a patch is considered isolated, the distances of its endpoints from the center point and other patches are measured. Generally, a patch is considered isolated if both endpoints are far away (around 30 to 50 pixels) from other patches or if the nearest patches to its endpoints are the same. After identifying all isolated patches, I recheck them to see if any two patches are paired together. This involves examining the distances between their endpoints and those of other patches. If the minimum distances of both endpoints from

other endpoints are larger than 50 pixels, they are labeled as solo isolated patches. If two or more patches are close to each other within their neighborhood, they will connect to each other by artificial edges, as they are part of a larger flame fragmentation that has broken into smaller patches. Figure 2.13 shows a sample processed image of the flame's tip of methane at a Reynolds number of 10,000.



Figure 2.13: Processed image of methane flame at the tip section with a Reynolds number of 10000

For liquid spray with prevaporized liquid fuel flames, similar algorithm to the flame's tip is used. This is due to the presence of various small flame fragmentations around the main jet flame. The algorithm exclude isolated patches based on their size and their distance from other patches. After excluding the isolated patches, the main prevaporized base of the flame algorithm is applied to detect the flame edges. However, the criteria to identify isolated patches in the spray case may differ slightly. Since the small patches are much closer to the main flame, a smaller threshold distance is required compared to the prevaporized case.

2.3.2 Flame Surface Density Procedure

The reactant and product sides should be identified following binarizing the images locally utilizing a moving box. It is impossible to distinguish between distinct flame areas due to extinction. The method solves the problem by artificially connecting the ends of each reaction zone. The binarization method applies again to fill the reaction zone. The binarization procedure was utilized to derive the progress value contour of 500 photos. After that, a map of progress variables between 0 and 1 is created by combining them and taking an average. The density of the flame surface is computed using the following equation (Eq. 2):

In this equation, A_f and L_f are time average surface area and length of flame in the control volume of Δx^2 . For calculating the flame surface density, the flame front edge is considered. Damkohler suggested that turbulence affects flamelet regimes to wrinkle and disturb the reaction layer. This idea implies that the laminar local properties remain constant. Furthermore, following his assumption, the ratio of turbulent to laminar burning velocity S_T/S_L equals the ratio of turbulent to the laminar burning area (A_T/A_L). A_T and A_L represent a wrinkled turbulent and laminar flame's burning area, respectively. Discroll [Discroll, 2008] showed that the ratio of turbulent to the laminar area could be calculated with the following equation:

$$S_T/S_L = A_T/A_L = \int \Sigma dx \quad (2.12)$$

In this equation, η is the normal axis to $\langle c \rangle = 0.5$ from the binarized and averaged CH PLIF. The flame surface density is explained and calculated in this section.

2.3.3 OH Pseudo method

As shown in Figure 2.14, the OH PLIF pictures are straightforward, dividing the reactant and product areas. It cannot, however, detect extinction events or flame edge breaks. Figure 2.15 depicts the reaction zone's outer surface (product side) for the CH and pseudo-

OH techniques. Because only the edge of the reaction zone is visible with CH PLIF (Figure 2.15a), the extinctions and breaks may hinder the distinction between the reactant and product sides. The locations on the flame breaks are artificially linked to imitate OH PLIF compared with the CH PLIF technique. The OH PLIF, which differentiates the reactant and product parts, is similarly represented by this artificially linked surface, which I call OH-Pseudo. The extinction endpoints on the CH PLIF are depicted in Figure 2.15b within a red rectangular box containing the fabricated lines. The flame surface density is estimated using two distinct approaches to determine the potential differences.

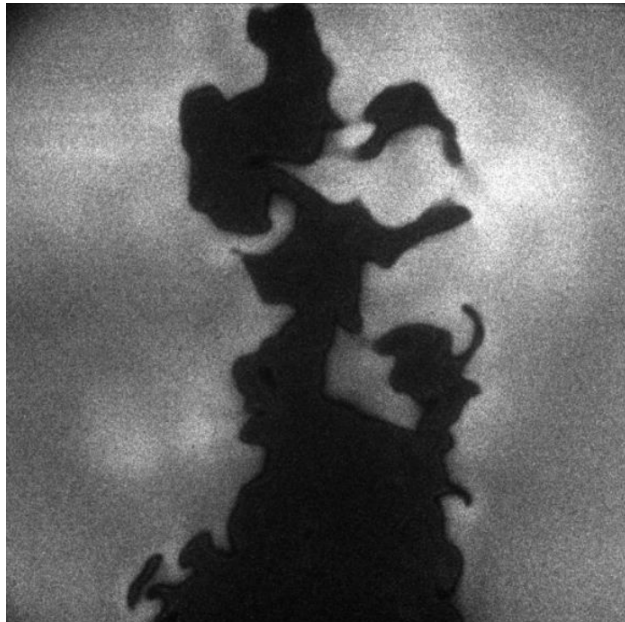


Figure 2.14: OH PLIF image sample of prevaporized JP8 at equivalence ratio $\phi = 0.9$

The flame surface area per unit is assumed to be the same as the flame surface perimeter. An 11 by 11 interrogation box is used to quantify the flame edge in each pixel for the whole image. In the inquiry box, the length of the flame for 500 CH PLIF photos is estimated by counting the number of pixels representing the flame front. The flame surface density in the center of the interrogation box is calculated by dividing the entire length by the area of the interrogation box. The average flame surface density is measured using a 2 threshold for each progress variable. Then, variation of measured Σ based on progress

variable c is presented.

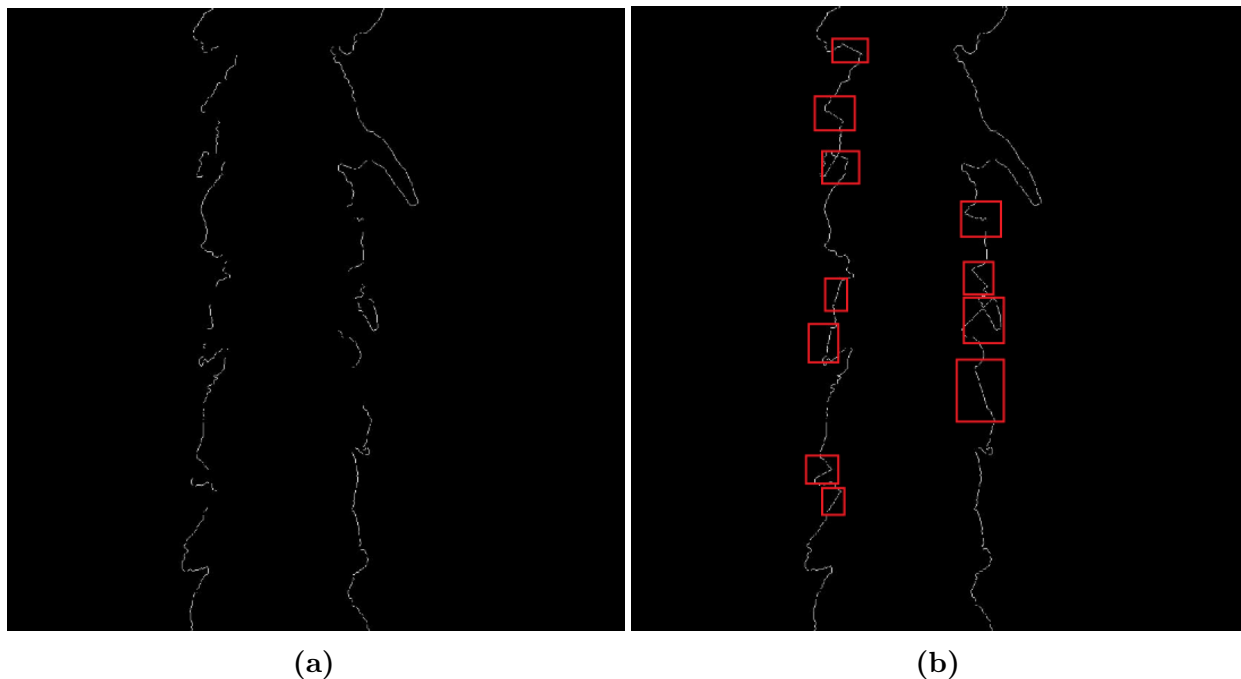


Figure 2.15: Product and reactant regions detected by (a) special algorithm for the middle section of the flame, (b) base of the burner algorithm

2.4 Apparatus

This section outlines the experimental setup and procedures used to capture flame statistics for prevaporized liquid fuels, spray liquid fuels, and chemiluminescence experiments. The study of prevaporized liquid fuel flames was conducted using a McKenna burner, while a HiPilot burner was utilized for spray liquid fuel flames. The details of each experiment are explained in the following sections.

2.4.1 McKenna Burner

The experimental setup used in this study is schematically depicted in Figure 2.16a. The setup is based on a McKenna burner with a central tube diameter of 7.6 mm and a flat flame plate with a 60 mm diameter utilized as a pilot. A methane-air mixture at stoichiometric conditions was used for the pilot burner with a mean flow velocity of 60 cm/s.

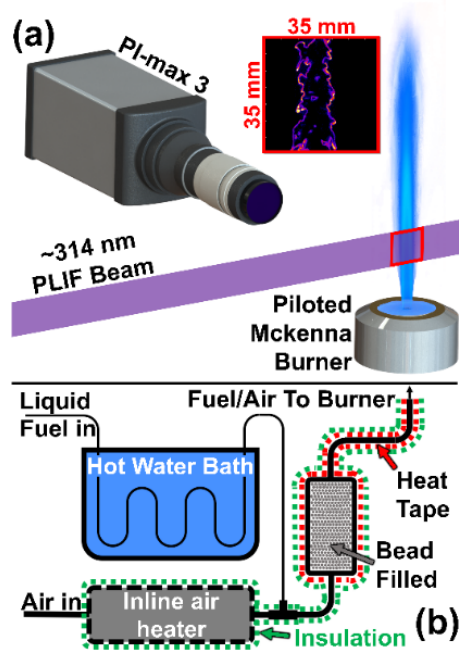


Figure 2.16: (a) Piloted McKenna burner and imaging setup. (b) Pre-vaporizer schematic

In this experiment, three different fuels, n-Dodecane, n-Heptane, and methane, were operated at a jet Reynolds number of 10,000. In order to study the liquid fuels in the premixed regime, a temperature controllable pre-vaporizer system, shown in Figure 2.16b, was implemented. Liquid fuels pass through a hot water bath to be preheated before mixing with air. Inline heaters were used to increase the air temperature to the desired point. Then the heated air and heated fuels enter the insulated mixing chamber for mixing. With control over water bath temperature and inlet heater, the degree of prevaporization can be tuned.

Table 2.1: Operating conditions for prevaporized, premixed jet flames

Re	Fuel	ϕ	Exit Velocity (m/s)	Laminar Flame Speed (cm/s)
10000	Methane	0.8, 1, 1.2	46	75.5
	n-Heptane	0.8, 1, 1.2	42	85.7
	JP8	0.8, 1, 1.2	43	68.6
	n-Dodecane	0.8, 1, 1.2	42	77.2
20000	Methane	0.8, 1, 1.2	92	75.5
	n-Heptane	0.8, 1, 1.2	84	85.7
	JP8	0.8, 1, 1.2	86	68.6
	n-Dodecane	0.8, 1, 1.2	84	77.2

Turbulent, prevaporized premixed combustion of different fuels are presented in Table 2.1. A mixture of methane-air with a 60 cm/s flow rate runs through the pilot flow for all the cases. Equivalence ratios of 0.8, 1, and 1.2 are presented for this work. The preheating temperature is set to 470 K such that all liquid fuels are vaporized properly.

2.4.2 HI-Pilot Burner

For spray liquid flame, the schematic of the experiment setup can be seen in Figure 2.17. The setup is based on the Hi-Pilot burner for both prevaporized and spray liquid fuels up to 99,000 Reynolds numbers. The burner consists of a nebulizer prevaporizing system to produce a fully vaporized and premixed mixture of fuel and air. Additionally, a 260-micron diameter needle is implemented in the burner to inject liquid fuel into the mixture. The jet Bunsen burner is surrounded by a flat plate pilot burner to provide extra heating and stabilization in the main jet flame.

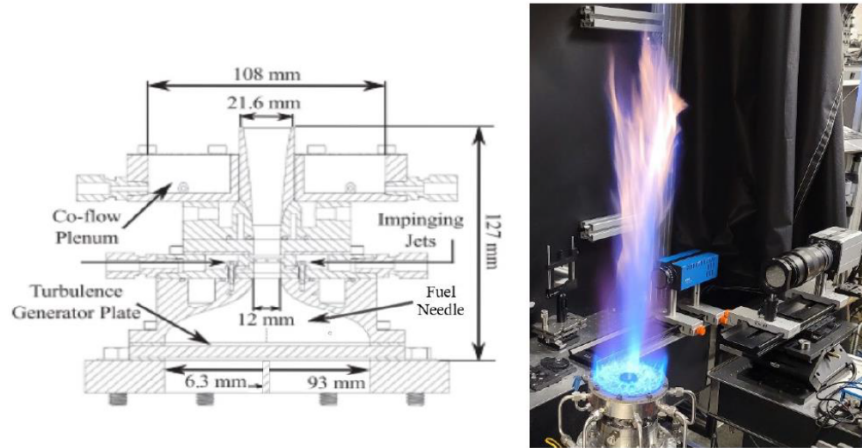


Figure 2.17: Hi-Pilot burner schematic

The conditions and fuel selection in the spray liquid experiment were based on two different categories. The first category is based on the turbulent intensity of the flow. Three different flows with Reynolds numbers of 10K, 25K, and 50K were tested while the turbulence intensity increased for each case. The second category in the experiment condition is fuel preparation. This includes premixed methane alongside liquid spray fuels, pure premixed prevaporized liquid fuels, and lastly, prevaporized liquid fuel alongside spray liquid fuels. These two categories, combined together, provided wide and diverse options toward the investigation of turbulent heavy hydrocarbon liquid fuel flames.

2.4.3 Chemiluminescence Experiment Setup

For the chemiluminescence experiment, the following setup as shown in Figure 2.18 has been used to capture CH and OH signals. Prevaporized methane, n-Heptane, n-Dodecane, and JP8 at 470K temperature and $Re=10K$ run through the piloted McKenna jet burner. A specific CH filter centered at 430 nm wavelength with a ± 10 nm margin was utilized to capture the CH chemiluminescence signal. The field of view captures the entire flame length. The spectroscopy of the flame has been done via Ocean Optics Flame model with 0.3 nm resolution and 600-micron diameter fiber. The exposure time varied from 1 to 10 seconds, and the chemiluminescence signal is the average signal of 3 similar measurements.

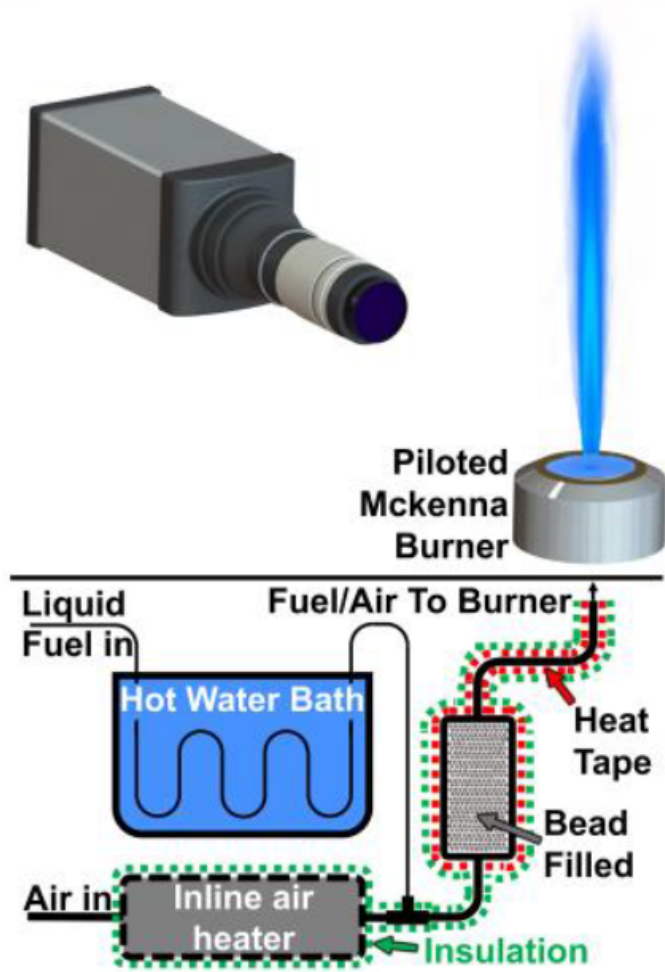


Figure 2.18: Schematic setup of chemiluminescence experiment

Chapter 3

Prevaporized Liquid Fuels

3.1 Introduction

In this chapter, several pre vaporized liquid fuels are tested to analyze their turbulent flame structures. The flame structures and statistics of these fuels are measured and compared to those of pure methane flame at two different turbulence intensities. The aim is to find a relationship between CH fluorescence signals in regions with high curvature values and interpret any influence of the Lewis number, as suggested by the DNS results. Additionally, this chapter compares the use of CH PLIF with the commonly used OH PLIF to determine which method better captures flame details for a more comprehensive understanding of turbulent combustion.

3.2 Imaging

Study of CH PLIF using the ($v'=0$, $v''=0$) band enables capturing the turbulent flame structures induced by the 10 Hz Nd:YAG laser at 314.4 nm wavelength. By emitting 1.3 mJ energy per pulse of the laser, this method is designed to measure CH PLIF in the saturated regime of the laser. It was initially developed and presented by Carter [Carter et al., 2014, Carter et al., 2016]. An optical system consisting of a cylindrical lens of 50 mm

and a spherical lens of 1000 mm produces the desired laser sheet. In order to visualize the results, a PIMAX III intensified camera is used together with a UV-Cerco 100-mm focal length lens. Polarization of horizontal beams minimizes the Rayleigh scattering effect. In order to provide optimal visual impressions, the gate factor and gain are set to 51% and 250 ns, respectively. During these experiments, the field of view was 35 x 35 mm, and the resolution was measured to be 34 microns per pixel [Gandomkar et al., 2021b].

3.3 Fuel Differences

In this study, CH PLIF was conducted for combustion of premixed, pre-vaporized liquid fuels at two different turbulence intensities of $Re=10,000$ and $20,000$, and different equivalence ratios of $\phi=0.8$, 1 , and 1.2 . Liquid fuels of n-Heptane, JP8, and n-Dodecane have been selected and prevaporized for these experiments to compare with gaseous methane flame. After imaging and processing them, which were explained in the previous chapter, curvature is measured by using a novel method to identify reactant/product sides of the flame edges and assign the correct sign of the curvature [Gandomkar et al., 2021a]. The following sections express the turbulent characteristics of flame structures.

3.4 Flame Statistics

Let's start this section with the curvature Probability Density Function (PDF) of liquid fuels and methane flames at different Reynolds numbers and equivalence ratios. Figure 3.1a expresses the curvature PDF of liquid fuels and methane at two different Reynolds numbers at equivalence ratio $\phi = 1.2$, 5 mm above the burner (the base of the burner). It is observed that for both turbulence intensities, liquid fuels have a wider curvature range than methane cases. The PDF of low curvature values for methane is larger, which indicates the flame structure for liquid fuels is more wrinkled compared to methane. Although the negative curvature patterns for all liquid fuels are similar to each other and have a significant difference with methane, the positive curvature is totally different. Based on the experimental and

DNS observations, it can be assumed that the flame extinctions and breaks occur around the regions with positive curvatures. It can be interpreted that liquid fuel flames contain more breaks than methane since the gap between the extreme negative and positive curvature PDFs is higher. Also, it seems that with higher turbulence intensity the flame structure gets more wrinkled and distribution of extreme and higher curvatures increases. This behavior has been observed for all fuels, even methane, where distribution of smooth structures with small curvature decreases with higher intensity of turbulence.

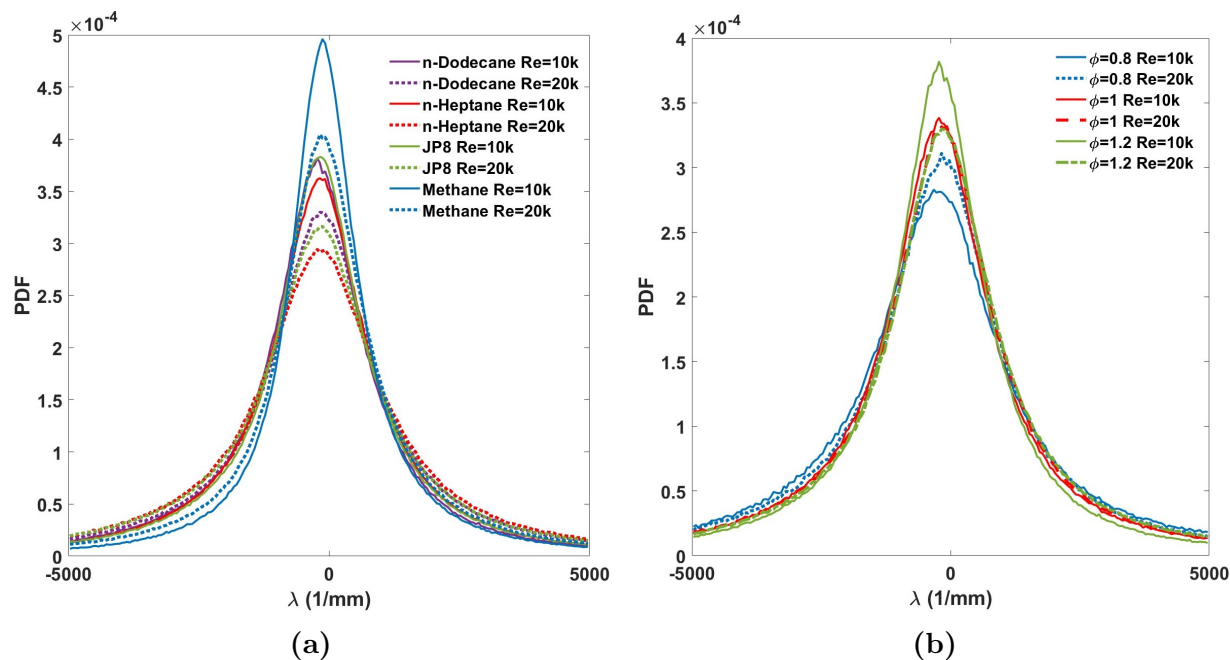


Figure 3.1: Curvature PDF of (a) all fuels with equivalence ratio $\phi = 1.2$, (b) dodecane with different equivalence ratios, 5 mm above the burner with 60 cm/s pilot flame at turbulent $Re = 10000$ and 20000

Figure 3.1b depicts the curvature PDF of n-Dodecane at $Re = 10,000$ and $20,000$, 5mm above the burner for different equivalence ratios of ϕ . It presents that the flame PDF profile gets wider by decreasing the equivalence ratio. This behavior could be due to flame extinction or more importantly, low signal detection. As the equivalence ratio decreases, the amount of CH fluorescence decreases as well. This causes ambiguity in detecting flame extinctions, which could lead to more extinction detection in lower equivalence ratios. It can be observed that lower equivalence ratio and lower CH fluorescence signal conclude more

wrinkling distribution. Although it should be mentioned that this distribution is not only due to the extinctions of flame, but not capturing flame edges due to lower signal of CH.

The statistics of curvature PDFs are presented below in Table 3.1. The variance of PDFs indicates that a wide range of curvature is occupied by liquid fuels rather than methane. It may suggest that the flame structure for liquid fuels is more wrinkled and complicated, and higher curvature values are achieved. It is a similar trend among all fuels that the mean of curvature decreases by increasing the equivalence ratio. It can be interpreted that a lower equivalence ratio leads to lower signal detection, which can cause extinction and breaks in flame structure. The skewness of the PDF distribution for liquid fuels decreases by increasing the equivalence ratio, while for methane it increases. This behavior expresses that for liquid fuels, the distribution of curvature PDF merges toward a symmetric distribution. In other words, the probability of positive curvature increases by increasing the equivalence ratio. All fuels show positive skewness for all equivalence ratios. A positive skewness means the distribution is right skewed and the mean of curvature is higher than the median value. While the flame goes from a lean condition to a rich one, the mean increases. It seems the rich liquid fuel flame has a higher probability of positive curvature compared to lean flames. Increasing the equivalence ratio increases the kurtosis of curvature PDF for all fuels. It means by increasing the equivalence ratio, the distribution diverges from normal distribution and its tail gets thicker. So the probability of higher curvature values increases.

Table 3.1: Statistical measurement of curvature PDFs

	ϕ	Mean (1/m)	Variance*(10e6)	Skewness	Kurtosis
Methane	0.8	-47.1	2.9	0.0751	3.7
	1	-42.5	2.2	0.1022	4.5
	1.2	-29.3	1.9	0.1227	4.9
Heptane	0.8	-194.4	3.6	0.1052	3.1
	1	-230.4	2.9	0.0805	3.6
	1.2	-183.0	2.7	0.0697	3.8
JP8	0.8	-303.9	3.1	0.1171	3.5
	1	-256.2	2.8	0.0842	3.7
	1.2	-156.6	2.6	0.0733	4.0
Dodecane	0.8	-295.3	3.6	0.1393	3.2
	1	-266.1	3.0	0.1043	3.6
	1.2	-271.7	2.7	0.0758	3.8

I showed the effect of turbulence intensity briefly before, but let's analyze its effect in more detail in Figure 3.2. Figure 3.2a shows negative curvature percentage of total distribution at different Reynolds numbers for all liquid fuels and methane. It appears for all fuels, the distribution of negative curvatures decreases at higher Reynolds numbers. Moreover, Figure 3.2b depicts the width of PDF corresponding to 10% of the maximum value for all fuels. The PDF distribution appears to broaden for all fuels by increasing the intensity level.

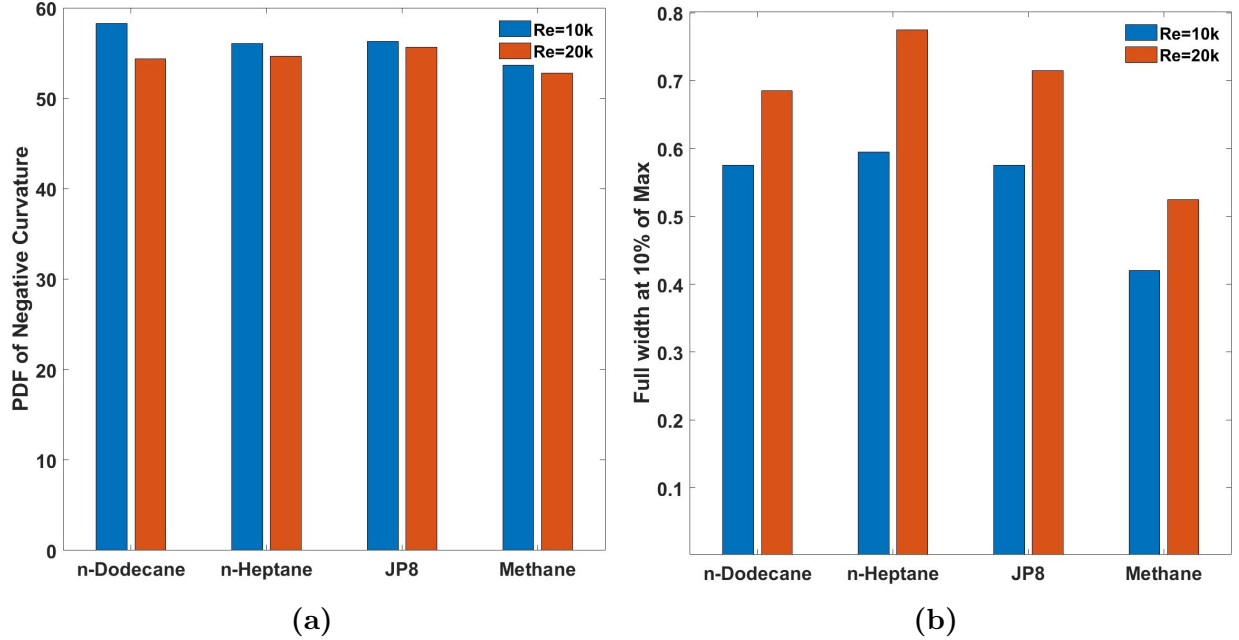


Figure 3.2: Turbulence intensity effect on flame statistics. a) Probability density functions of negative curvatures. b) width of 10Max Probability density functions, of all fuels at equivalence ratio $\phi = 1.2$ and two different Re numbers, 5 mm above the burner with 60 cm/s pilot flame

Additionally, frequency of local extinctions or breaks within the flame and their average length have been calculated and presented in Figure 3.3. Figure 3.3a displays the average quantities of extinction frequency for all fuels at different Reynolds numbers. It can be concluded that for most fuels the probability of local extinction increases at higher levels of turbulence. Number of breaks and extinctions for liquid fuels are significantly higher compared to methane regardless of Reynolds number, which suggests that the local extinction is not solely dependent on intensity level and fuel's properties may have an important role in it. Also, Figure 3.3b expresses the average length of extinctions at different Reynolds numbers for all fuels. As expected, the length of breaks is higher for liquid fuel flames compared to methane flame, and average length of break enlarges at higher turbulence levels.

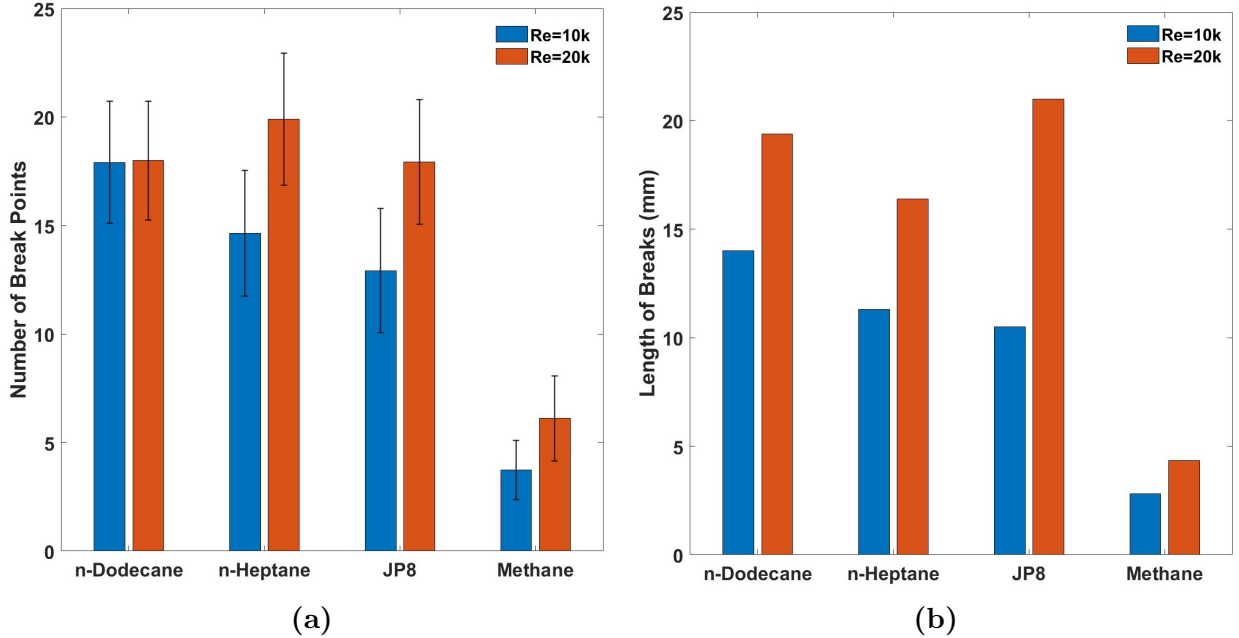


Figure 3.3: Turbulence intensity effect on flame statistics. (a) Local extinction frequency (b) Averaged size of extinctions, for all fuels at equivalence ratio $\phi = 1.2$ and two different Re numbers, 5 mm above the burner with 60 cm/s pilot flame

The next feature of flame topology, flame surface density, is determined and presented for all cases in Figure 3.4. Figure 3.4a shows the mean of calculated flame surface density (Σ) for each progress variable (c) for all fuels with CH PLIF and OH Pseudo methods at equivalence ratios of 1.2. The sizing step of the progress variable is 0.1, including a threshold of 2% to extract the flame surface density. The OH Pseudo method shows a higher flame surface density than CH PLIF for all cases. The reason is that the OH Pseudo method connects all edges of the flame, so the extinction or flame breaks are discarded. In this case, liquid fuels all have higher FSD¹ than methane, which suggests the flame length distribution increases compared to the flame area. However, in CH PLIF, methane flame presents the highest FSD among the fuels. The reason is mainly the flame extinction that occurs in liquid fuels. The difference in CH FSD between CH PLIF and OH Pseudo methods suggests that the extinction rate in methane seems to be the lowest compared to liquid fuels, and n-Dodecane shows the highest extinction rate due to the difference of CH PLIF and Pseudo

¹Flame Surface Density

OH PLIF.

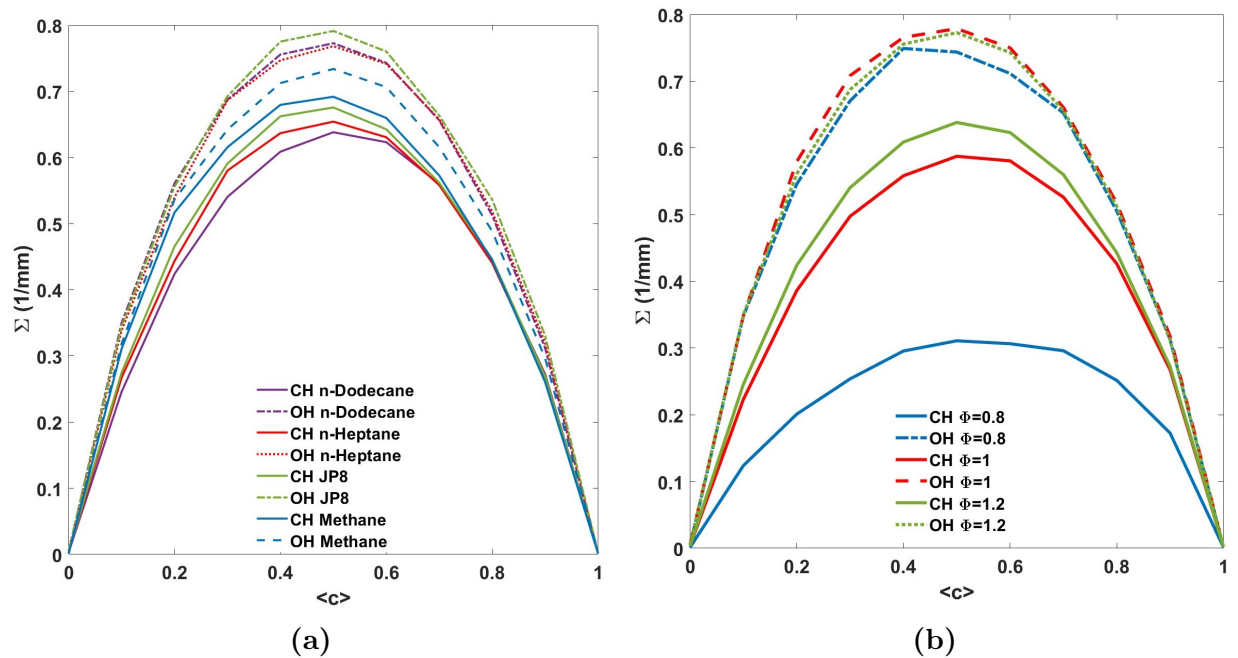


Figure 3.4: Flame surface density of CH PLIF & Pseudo OH PLIF for turbulent flame $Re=10,000$ for (a) all fuels at equivalence ratio $\phi = 1.2$, (b) dodecane at different equivalence ratios, 5 mm above the burner with 60 cm/s pilot flame

The effect of equivalence ratio on flame surface density is shown in Figure 3.4b where FSD of n-Dodecane for two CH and OH Pseudo methods has been expressed at various equivalence ratios. The flame surface density of n-dodecane increases by increasing the equivalence ratio, which means the flame distribution area decreases compared to flame length. The differences between CH and OH Pseudo methods increase significantly for lower equivalence ratios. This decrease is not just due to the extinction rate, where a lower CH signal due to the lean condition of combustion intensifies the effect of extinction.

The next turbulent feature which can be studied based on the CH PLIF is the total actual burning area relative to the exit velocity of the burner. Figure 3.5 shows the averaged ratio of length to area of the flame for each fuel at different exit velocities of fuel with a specific equivalence ratio. The laminar flame speed normalizes the exit velocity of the fuel regarding equivalence ratio.

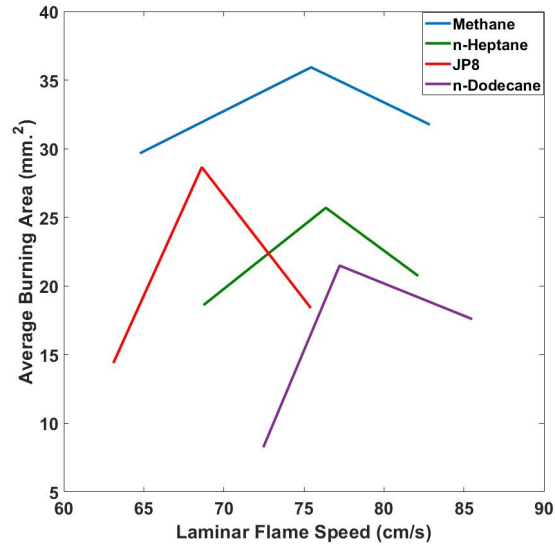


Figure 3.5: Average ratio of length to area of turbulent flame at $Re=10,000$ and all fuels flame 5 mm above the burner with 60 cm/s pilot flame

The ratio of turbulent speed to laminar flame speed has been depicted in Figure 3.6a for fuels at equivalence ratio $\phi = 1.2$ across the axial location. The liquid fuels' turbulent velocities increase rapidly along the axial location in CH PLIF and OH Pseudo methods. At the same time, methane seems to have constant or slow progress across the flame height. The equivalence ratio's effect on the turbulent flame speed of n-Dodecane has been displayed in Figure 3.6b where turbulent velocity increases alongside the axial location for the rich flame. At the same time, it remains constant halfway through stoichiometric conditions and decreases for the lean flame.

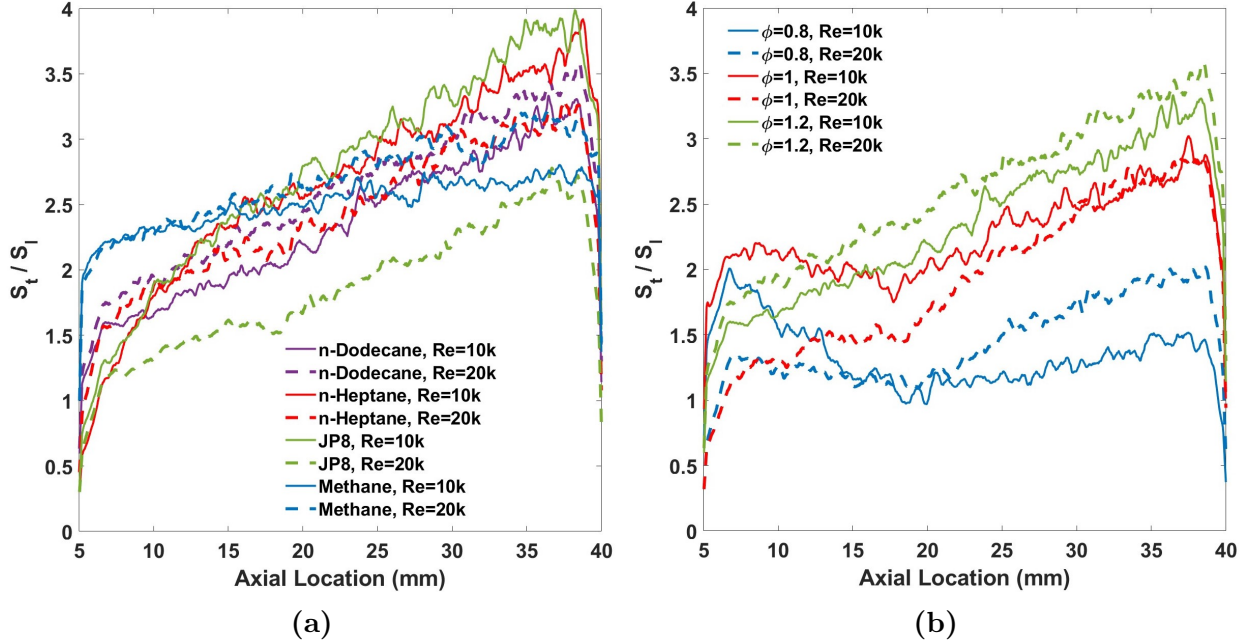


Figure 3.6: Turbulent velocity of turbulent flame $Re=10,000$ for (a) all fuels at equivalence ratio $\phi = 1.2$, (b) dodecane at different equivalence ratios, 5 mm above the burner with 60 cm/s pilot flame

3.5 Lewis Number Effect

The algorithm captures turbulent flame structure using a technique to distinguish reactant and product sides of the flame and accounts for curvature sign correction. Also, this method enables the investigation of non-unity Lewis number ($Le \neq 1$) effects on flame structure and curvature distribution in prevaporized, premixed turbulent liquid fuel jet flames. The Figure 3.7 presents curvature PDF of n-dodecane, n-heptane, JP8, and methane at $Re = 10,000$ for 5 mm above the burner using CH PLIF measurement. It is observed that liquid fuels have a wider curvature range than methane cases. The PDF of low curvature values for methane is larger, which indicates the flame structure for liquid fuels is more wrinkled than methane. Although the negative curvature patterns for all fuels are similar, the positive curvature is different. The flame extinction and break occur around the regions with positive curvatures. This is may be due to the following reasons:

- 1- The flame surface of positive curvature increases toward the reactant which is cooler and

may lead to the losing heat and cooling flame temperature and quenching flame

- 2- High positive curvature zones experience dilution of heat and reactive species because the flame is forced to spread over a larger area, which weakens the concentration of fuel and oxidizer in the reaction zone, reducing the chemical reaction rates
- 3- When a flame front is convex (positive curvature) toward the reactants, it experiences higher strain rates due to the turbulent flow and increased flame stretching. The flame speed must increase to keep up with the expanding flame surface. This stretching effect can thin the reaction zone, making it harder for the flame to maintain the high temperatures and reaction rates.

It can be interpreted that liquid fuel flames contain more breaks than methane since their positive curvature PDF is higher than methane.

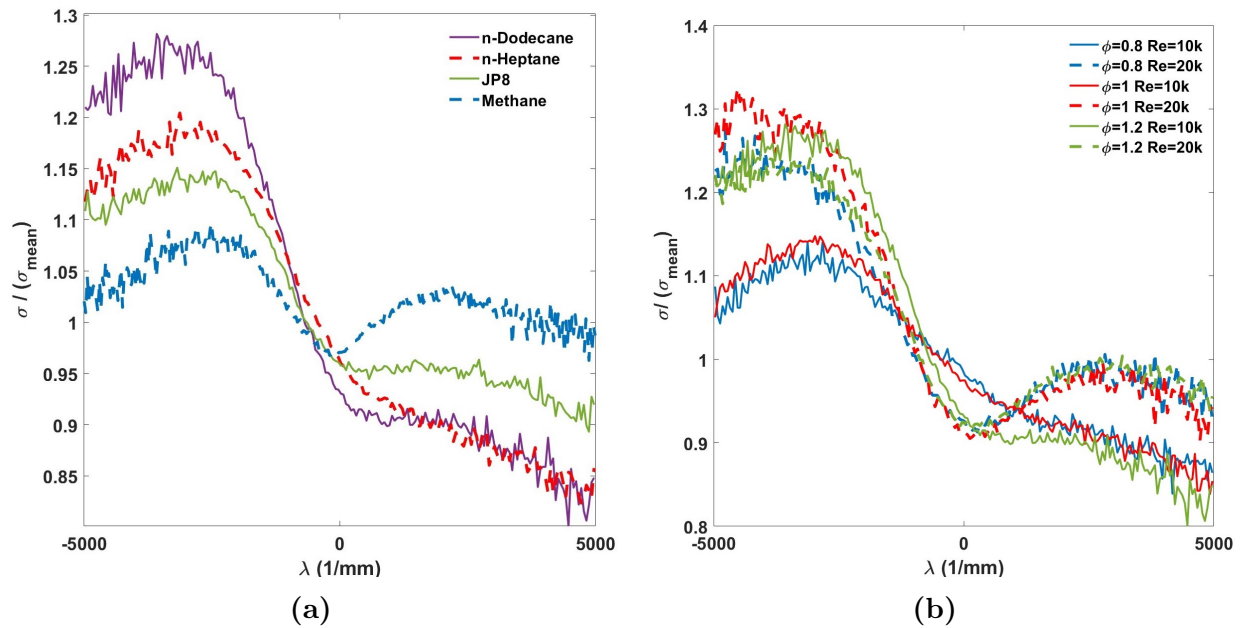


Figure 3.7: Signal-curvature correlation of turbulent flame $Re=10,000$ for (a) all fuels at equivalence ratio $\phi = 1.2$, (b)dodecane at different equivalence ratios, 5 mm above the burner with 60 cm/s pilot flame

Figure 3.7a depicts the relation between CH signal and curvature for n-Dodecane, JP8, n-Heptane, and methane at the equivalence ratio of 1.2. This result shows the effect of the Le number on curvature/signal behavior. As discussed earlier, the DNS result relates to heat

release and high curvature regions. Also, experimental observation expresses a relationship between CH signal and high curvature area. This behavior is more decisive for fuels with high Le numbers like n-Dodecane. For liquid fuels with a higher Le number, the signal increases as the curvature decreases, while methane does not follow a similar trend.

The positive and negative curvatures seem to have a similar range of signal values for methane. Based on Figure 3.7b, for n-Dodecane, it appears that the negative curvatures have a higher signal compared to positive curvatures. The average signal value reported for high negative curvature (-5000) is higher than the positive curvature (5000). A linear fitting line is represented for each curvature/signal to quantify the correlation while R-2 square coefficients are measured.

CHEMKIN simulations of flame chemiluminescence in experimental conditions are conducted to estimate the CH concentration's behavior regarding the turbulence effect and equivalence ratio. This study aims to determine the effect of strain rate on CH concentration and provide evidence of the Le number effects shown in the previous section. Two counter-flow flame modules utilized with the stoichiometric methane-air mixture and preferred fuel with a specific equivalence ratio measures the CH concentration in different strain rates. For these calculations, GRI Mech 3, HyChem, and JetSurf 2.0 have been utilized for methane, JP8, and n-Dodecane, respectively. The total value of CH concentration and heat release are calculated and presented below in Figure 3.8.

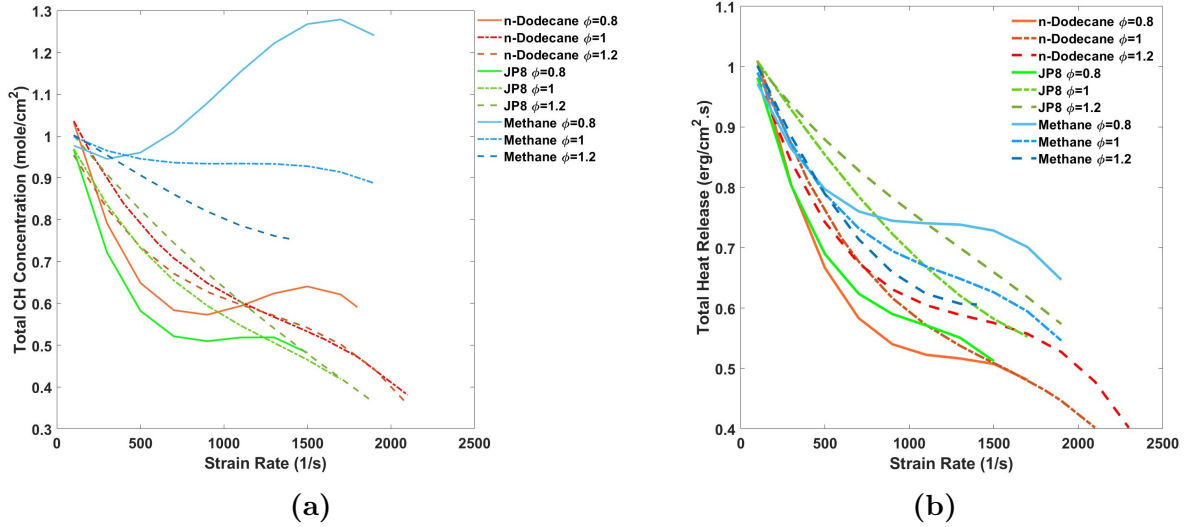


Figure 3.8: Measured quantities of (a) Total CH concentration, and (b) Total Heat Release over strain rate for heavy liquid fuels and methane at different equivalence ratios

As shown in Figure 3.8a, by increasing strain rate, for most fuels, the CH concentration decreases until global extinction occurs. However, for the lean methane case, a peculiar behavior is observed. It seems the CH production accumulated over the course of strain rate.

Additionally, Figure 3.8b shows the effect of strain rate on the amount of heat release for all fuels and equivalence ratios. It appears the value of heat release decreases by increasing the strain rate. This behavior is expected, as increasing strain rate prolongs the chemical time scale and shortens the dynamic time scale. These alterations lead to lower reaction rates and CH formation overall in higher Reynolds numbers.

Chapter 4

Spray Liquid Fuels

4.1 Introduction

In this chapter, various combinations of spray liquid fuels alongside prevaporized liquid fuels are used to analyze their turbulent flame structures. The flame structures and statistics of these fuels are measured at different turbulence intensities. The goal is to investigate droplet interactions with the flame, fragmentation, vaporization, and flame stabilization by analyzing the turbulent flame statistics of liquid spray fuels. The measurement procedures and calculations are similar to those used in the prevaporized case. Most of the spray liquid experiments are conducted using OH PLIF, which is not the primary focus of this research. However, a few selected cases are measured with CH PLIF for detailed analysis in our studies.

4.2 Imaging

In order to capture the liquid spray flame structure, a CH PLIF similar to the prevaporized experiment was conducted. But instead of exciting the CH at CX Q-branch, the R-branch excitation was implemented. The excitation is around 311nm wavelength, and to prevent interference from Mie scattering, two filters of UG5 and Semrock 0002 were installed in imaging equipment. The field of view in this experiment was determined to be 50*50. By

applying a binning process, the resolution of 49 micron/pixel was achieved. For CH and OH excitations, the amount of laser energy was recorded as 1-2 mJ/pulse and 3-4 mJ/pulse, respectively.

In the next sections, I try to evaluate statistics of spray flames to highlight their impact on prevaporized flames. Additionally, the Lewis number effect of spray flame has been investigated and curvature-signal relation has been depicted to demonstrate liquid fuel spray's effect on turbulent flames.

4.3 Flame Statistics

Figure 4.1 shows sample CH PLIF images of prevaporized methane flame with different additions of liquid n-Heptane spray. As can be seen, the effect of the Le number is similar to what we saw earlier in prevaporized cases. For cases with higher Le number fuels, the region of higher signal is the region with high negative curvature. The signal value for premixed methane with a liquid spray of n-Heptane is much higher compared to pure premixed methane.

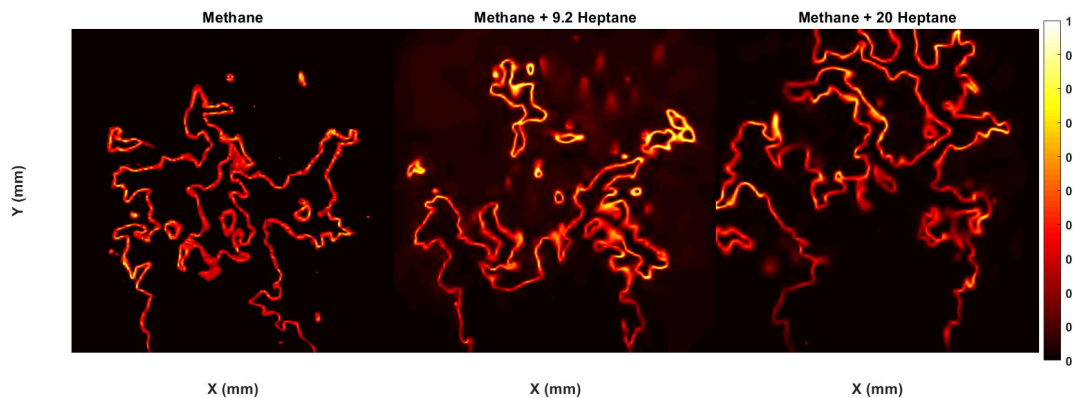


Figure 4.1: Pure Premixed methane at equivalence ratio $\phi = 0.9$ (Left), Premixed methane at equivalence ratio $\phi = 0.75$ alongside spray liquid n-Heptane with 9.2 mL/min (Middle), and 20 mL/min (Right) flow rate

The challenges in topology analysis of liquid spray flames are concerned with the algorithm to detect flame structure and calculate turbulent features. In this case, extinction and breaks occur more frequently compared to the prevaporized case, because the interaction of liquid droplets with the flame surface may lead to severe quenching. This may affect the performance of the existing algorithm, which was developed based on local moderate extinction. Also, strong Raman scattering from droplet pockets appears in the imaging due to the high density of fuel components in liquid droplets. Additionally, the low concentration of CH in lean or extremely rich conditions leads to low CH fluorescence signal, which makes topology measurement difficult.

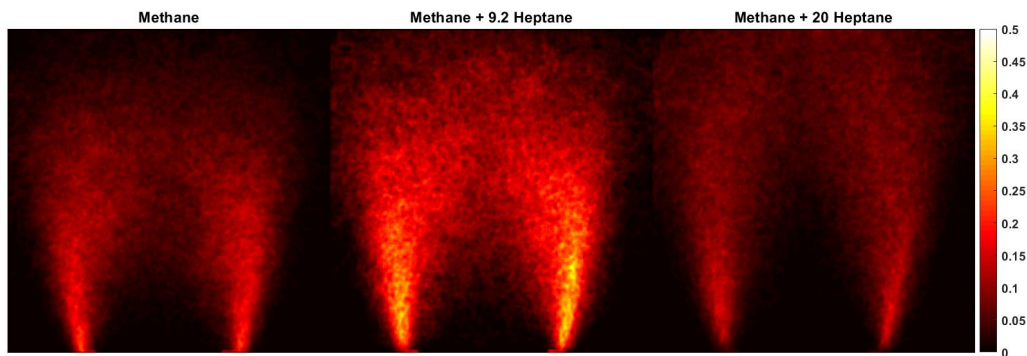


Figure 4.2: 2D map of averaged FSD for pure methane, and methane with different flow rates of n-Heptane

Figure 4.2 shows the 2-D FSD map of three different pure methane, methane, and spray n-Heptane cases with two different flow rates. Adding liquid sprays generally broadens and extends the flame compared to the pure prevaporized case. For methane, adding 9.2 ml/s of n-Heptane improves FSD and wrinkling of the flame, while adding 20 ml/s of n-Heptane decreases FSD across the axial location. It can be interpreted that the liquid spray can enhance turbulent flame features up to a point. After that, it seems that interaction of larger

and more frequent liquid droplets with the flame surface causes extinction and breaks out of the flame.

I tried to analyze the effect of liquid fuel sprays on flame structure and statistics for different turbulent intensities. The first objective is the distribution of signal values captured from the flame edges. For this observation, we focus on methane and n-Heptane jet flames with addition of n-dodecane and n-Heptane for two different turbulent intensities. The effect of n-Dodecane addition to methane flame's signal distribution is shown in Figure 4.3. For both turbulent cases, the addition of liquid spray increases the distribution of higher signal values, indicating that regions with higher CH concentration increase compared to lean methane flame and the distribution of signal is much similar to the rich methane flame. This can be explained by the fact that the interaction of liquid droplets can have other effects besides flame quenching. It appears that for some regions, the flame can vaporize liquid droplets to increase the equivalence ratio in these regions, which leads to a richer flame and higher CH formation and concentration. As shown in Figure 4.3b, for higher turbulent intensity, the distribution of signal for lower liquid spray rate leans toward the lean flame, while the higher spray case behaves similarly to the rich flame. This behavior is probably due to the effect of Reynolds number and turbulence of flow on the mixing process. As regions with higher CH formation are created, since the mixing process is much faster, some of the high CH regions may break up and scatter into other regions, so their local equivalence ratios decrease. However, as the liquid spray flow rate increases, the dispersion rate is not enough compared to the increase in the number of high CH regions.

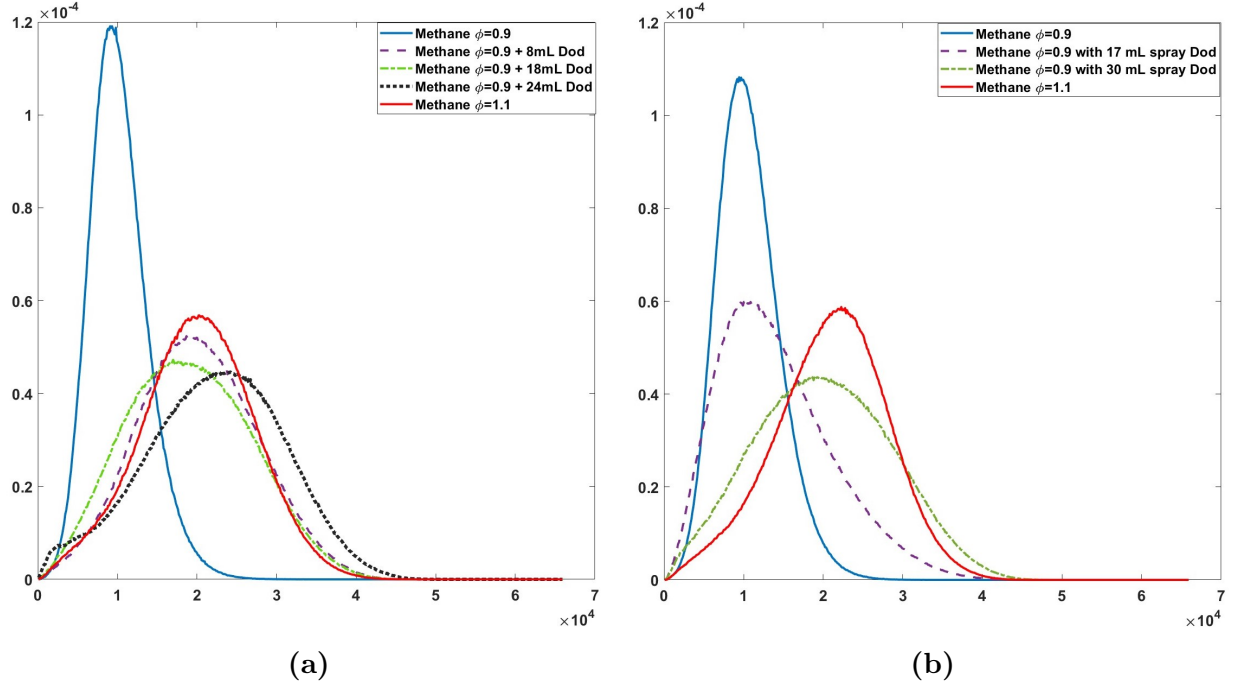


Figure 4.3: Flame signal PDF of pure methane with addition of n-Dodecane sprays (a) Case 2, (b) case 3

For the prevaporized n-Heptane with addition of n-Heptane liquid spray, for all cases of spray, the distribution of high signal values increases as predicted, shown in Figure 4.4. As shown in Figure 4.4a, for the lower turbulent intensity, it appears that none of the spray addition cases have a distribution profile similar to the rich flame of prevaporized n-Heptane. This is probably due to the incapability of the flame and turbulent intensity to vaporize liquid droplets completely, mix, and disperse the local rich region throughout the entire flame. However, for the higher turbulent intensity, the distribution of signal for different flow rates of sprays is intriguing, as presented in Figure 4.4b. The signal PDF¹ for the lowest spray flow rate follows the lean prevaporized n-Heptane flame PDF, with a slight increase in the high signal distribution, as if the quenching rate of the flame is canceled out with additional vaporized droplets to the flame. However, by increasing the flow rate of the spray to 30 mL, the signal PDF of the flame closely resembles the PDF of the rich prevaporized n-Heptane flame. It seems the dispersion rate of the vaporized droplets is higher than the extinction

¹Probability Density Function

rate caused by the droplets. Lastly, for the highest spray flow rate of 40 mL, the distribution profile reverts to the lean condition. It may be due to the fact that the extinction and quenching rate of the flame by the droplets is much higher, such that even vaporizing some portions of the droplets cannot compensate for it.

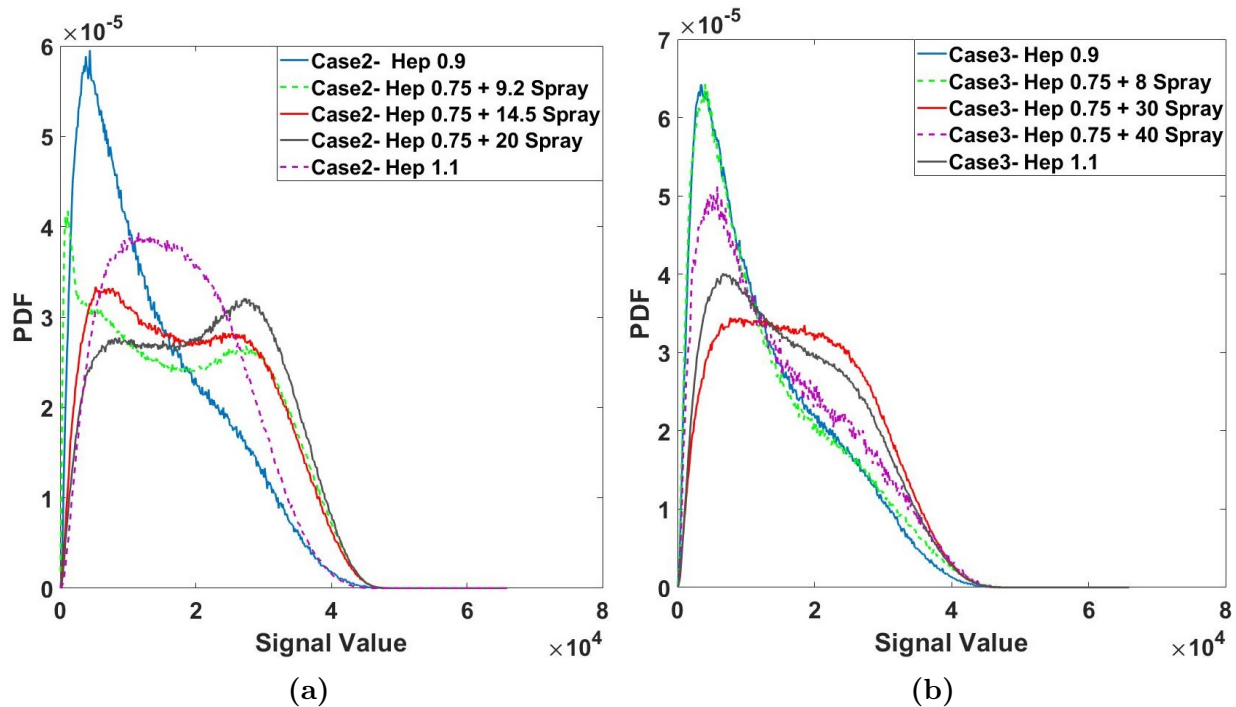


Figure 4.4: Flame signal PDF of prevaporized n-Heptane with addition of n-Heptane sprays (a) Case 2, (b) case 3

The next feature of the turbulent flame to study is the flame curvature and the effect of liquid spray on its distribution. In the following, Figure 4.5 shows the effect of spray addition on the distribution of signal values in the PDF of methane and n-Heptane. The effect of n-Dodecane spray addition on the flame curvature of methane is shown in Figure A.2a. The distribution of curvature PDF with addition of n-Dodecane is much similar to the rich methane flame. The spray addition cases have a wider distribution compared to the rich methane flame, indicating more wrinkling and sharp edges compared to the smooth structure of the rich methane flame. While increasing the spray flow rate after a point, it has the opposite effect. For the highest flow rate of spray, the curvature maximum PDF

is smaller than the maximum of the lean methane flame. This means the flame structure is not as smooth as the lean methane flame, and its edges have been demolished by the impact of liquid droplets on the flame. Figure A.2c shows the curvature PDF of prevaporized n-Heptane with the addition of liquid spray of n-Heptane with different flow rates. It appears that n-Heptane with equivalence ratio of $\phi = 0.75$ plus different flow rates of sprays show similar distribution of smooth curvature ($\lambda \approx 0$) compared to rich prevaporized n-Heptane. Another interesting outcome is the higher probability distribution of high negative curvatures for flames with liquid sprays compared to the rich flame, which suggests that spray cases have complex and wrinkled flame structures due to the interaction of liquid droplets with flames, although the overall distribution of their curvatures look similar.

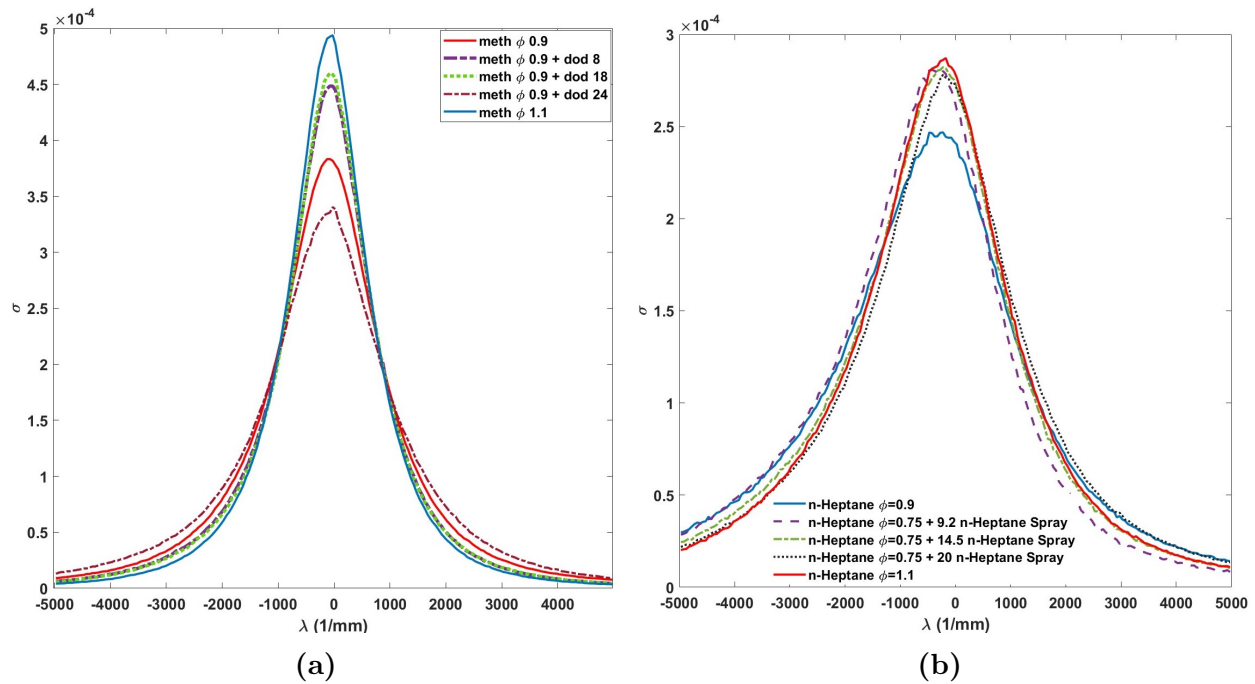


Figure 4.5: Signal-curvature correlation of turbulent flame $Re=10,000$ for (a) all fuels at equivalence ratio $\phi = 1.2$, (b) dodecane at different equivalence ratios, 5 mm above the burner with 60 cm/s pilot flame

Figure 4.6 shows the turbulent-to-laminar area ratio for pure methane and methane with n-Heptane sprays. The ratio of turbulent-to-laminar area, which indicates the ratio of turbulent to laminar flame speed, is higher for the lean case of methane. Additionally, adding

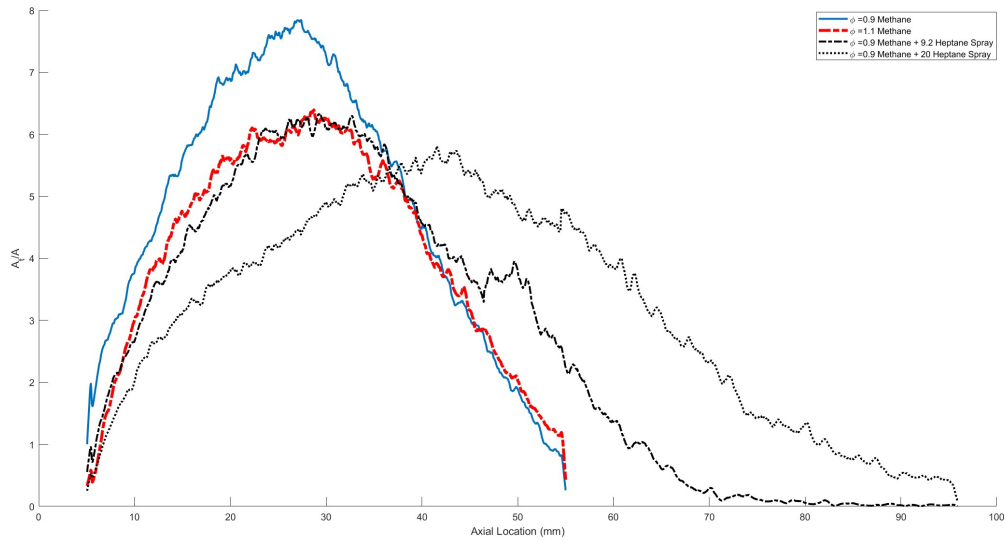


Figure 4.6: Ratio of turbulent flame area to laminar flame area for pure methane and methane with spray n-Heptane liquid

a spray of n-Heptane to methane spreads the flame longer, though the turbulent-to-laminar flame speed decreases along the flame. This may be due to the interaction of droplets with the flame.

Figure 4.7 shows different behavior for pure prevaporized n-Heptane and n-Heptane spray added to prevaporized n-Heptane. It appears that prevaporized n-Heptane with equivalence ratio $\phi = 0.75$ with 9.2ml/s spray n-Heptane shows a similar pattern to prevaporized n-Heptane with equivalence ratio $\phi = 0.9$. A similar trend is observed for prevaporized n-Heptane with equivalence ratio $\phi = 1.1$, and prevaporized n-Heptane with equivalence ratio $\phi = 0.75$ added with 14.5 ml/s spray n-Heptane. The interesting point is that the global equivalence ratio of these cases is similar to the pure prevaporized cases. The global equivalence ratio of $\phi = 0.75$ plus 9.2 ml/s spray n-Heptane is 0.9 , and the global equivalence ratio of $\phi = 0.75$ plus 14.5 ml/s spray n-Heptane is 1.1 . However, the difference in wrinkling between the pure and spray cases is significant. It suggests that although they have similar global equivalence, in the spray case, the length of flame per area increased, and it is more wrinkled compared to the pure case.

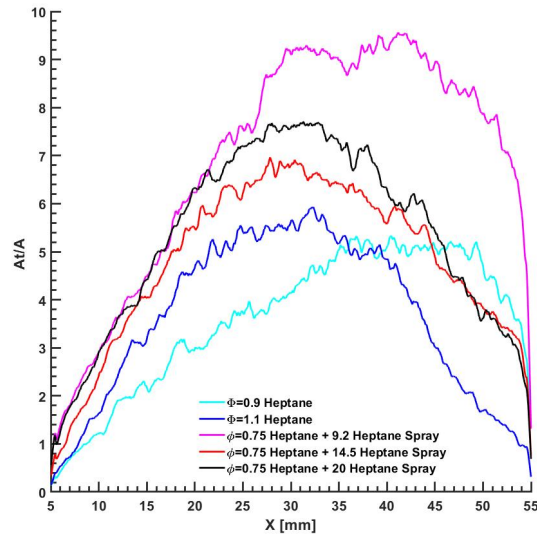


Figure 4.7: Ratio of turbulent flame area to laminar flame area for prevaporized n-Heptane with spray n-Heptane liquid

4.4 Lewis number effect

Similar to prevaporized research, after a comprehensive flame statistics analysis, fuel effect regarding Lewis number is investigated for liquid spray flames. In order to study Lewis number effect on liquid spray flames, measuring CH signal on the flame edges is essential. After detecting flame edges and interpreting the CH signal, the probability of regions with CH signal was presented in the previous section. It was shown that more regions with higher CH signal was presented in the previous section. It was shown that more regions with higher CH signals are received in spray cases than pure cases. This behavior is observed for all liquid fuels regarding the type of it. It presents that liquid fuel increases CH formation rates in the reaction zone, which leads to higher CH concentration and higher received signal. In order to depict the effect of the Le number, the correlation of CH signal values with corresponding curvature is required. Figure 4.8 shows the correlation of mean CH signal and curvature for turbulent methane flame alongside different concentrations of liquid n-Dodecane sprays at two different turbulent intensities.

It is observed that pure methane with lean and rich conditions shows somehow similar behavior at different curvature regions regarding the CH signal. However, adding liquid spray

changes this behavior significantly. It appears that adding liquid sprays increases the signal values at high negative curvature and lowers it at positive curvature, just what we expect for prevaporized liquid fuels. It can be assumed that as long as the methane flame is strong enough to evaporate liquid sprays, the vapor liquid fuel burns as well, and the characteristics of the methane flame change accordingly. Although adding liquid spray can enhance and improve the methane flame, it can have opposite effects as well when the amount of liquid spray increases beyond a certain point. As shown in Figure 4.8a, when we add 24 ml of dodecane to Case 2 of the methane flame, the signal-curvature correlation tends toward the pure cases. These cases may be a combination of evaporation and quenching in regions where the liquid spray makes contact with methane flames. The overall balance between these two factors seems to be in favor of quenching, so the total CH signal drops. Interestingly, when we add 30 ml of n-Dodecane to the methane flame in Case 3, which has higher turbulence intensity, the flame is capable of overcoming the quenching effect caused by liquid sprays as shown in Figure 4.8b. It can be assumed that the turbulence intensity can improve the flame when making contact with liquid droplets and enhance the evaporation process.

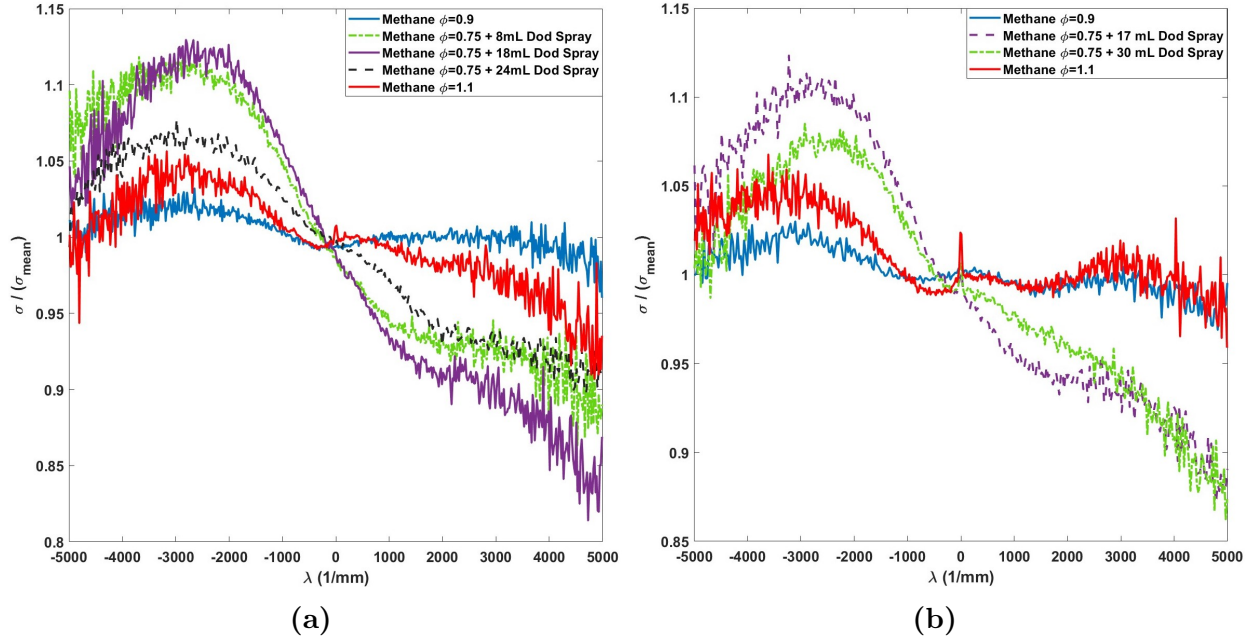


Figure 4.8: Signal-curvature correlation of methane turbulent flame with different liquid n-Dodecane sprays at (a) turbulence intensity case b, and (b) turbulence intensity case c

Figure 4.9 shows the signal-curvature correlation for pure n-Heptane lean and rich flames and two cases with added liquid spray of n-Heptane. The idea with these cases was to recreate locally lean and rich n-Heptane flame with a combination of prevaporized and liquid spray of n-Heptane and to see if the characteristics of spray flames were similar to prevaporized ones. For n-Heptane cases with liquid spray, they seem to follow neither the rich nor lean cases. Adding liquid spray to the prevaporized n-Heptane shows similar behavior to pure prevaporized lean cases in regions of negative curvature, while the positive curvature regions are completely different. It appears that due to turbulence or other unknown reasons, the vaporized droplets increase the CH production and thus CH signal in negative curvature regions. Furthermore, the addition of liquid spray to n-Heptane flame seems to behave like a methane flame where all regions of curvature correlate to a similar CH signal.

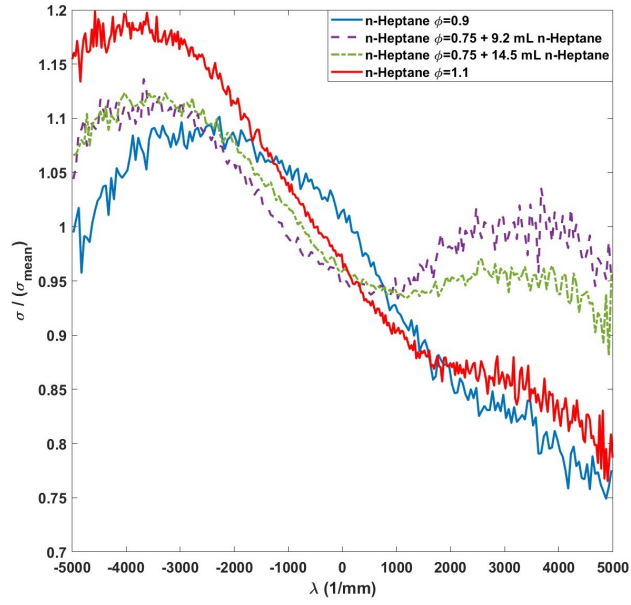


Figure 4.9: Signal-curvature correlation of prevaporized n-Heptane turbulent flame with different liquid n-Heptane sprays at turbulence intensity case b

Chapter 5

Chemiluminescence

5.1 Introduction

In this chapter, modeling simulations and experimental investigations are employed to identify the most accurate CH sub-mechanism for heavy hydrocarbon liquid fuels. Four chemiluminescence mechanisms for CH and OH are analyzed, each composed of CH* and OH* sub-mechanisms. These combinations affect the predicted CH*/OH* ratio. Photon emission rates for heavy fuels such as n-dodecane, kerosene, and JP-8 are post-processed from 1-D unstrained, laminar flame simulations at 300K and 470K. The simulation results are compared with experimental CH measurements to evaluate which sub-mechanism best predicts CH*.

The chapter also focuses on the use of chemiluminescence as a practical tool for studying combustion phenomena, including heat release, flame motion, and ignition/extinction events. Particularly useful in industrial settings with limited optical access, chemiluminescence is often applied in internal combustion engine research. However, since most data are based on methane, this chapter questions whether similar conclusions apply to heavier liquid fuels and addresses whether chemiluminescence is a suitable technique for studying such fuels.

Motivated by the need to compare experimental and computational approaches, the chapter evaluates chemical mechanisms that include chemiluminescence sub-mechanisms. Additionally, it assesses the spectroscopic validity of chemiluminescence data, ensuring consistency between experimental and theoretical models. These comparisons are crucial for validating both experimental methods and computational simulations.

The goals of this chapter are to test both full chemical mechanisms and chemiluminescence sub-mechanisms, ensuring that they predict the correct trends with varying equivalence ratios and allow reliable comparisons across different fuels. By doing so, the chapter enhances the understanding of chemiluminescence's role in combustion processes, particularly for heavy liquid fuels.

However, the chapter acknowledges several concerns and limitations. Certain quenching species are not included in the models, and the prediction of base formation species may be incomplete. Additionally, turbulence and flame area effects, as well as factors like Lewis number, stretch, and curvature, are not fully addressed. These factors could influence the accuracy of chemiluminescence predictions, especially in more complex flame conditions. These concerns highlight the need for further refinement in both experimental and computational approaches when studying heavy fuels.

5.2 CH Spectroscopy

5.3 Mechanisms and sub-mechanisms for CH and OH

In order to model CH^* and OH^* emission, the chemiluminescence sub-mechanism needs formation reactions, quenching and relaxation reactions, as well as their constant rates. The general mechanism for measuring CH and OH is provided for each fuel specifically. GRI Mech3 is the general mechanism for methane, while for n-heptane and n-dodecane, the Jetsurf 2 is the main mechanism that provides the reactions. JetSurF2.0 consists of 348 species and 2163 reactions. The development effort centers on n-dodecane and n-butyl-cyclohexane, but

the model includes the high-temperature chemistry of all n-alkanes up to n-dodecane and mono-alkylated cyclohexanes, including n-propylcyclohexane, ethylcyclohexane, methylcyclohexane, and cyclohexane, as well. Highly detailed HyChem mechanism is usually used for JP8, where it uses seven reaction steps describing JP-8 POSF10264 thermal decomposition and USC Mech IIa as the foundational fuel chemistry model. The cracked products considered are C₂H₄, H₄, H₂, CH₄, C₃H₆, 1-C₄H₈, i-C₄H₈, benzene, toluene, CH₃, and H. The oxidation kinetics of these cracking products are described by USC Mech IIa. After using CHEMKIN and main mechanisms for each fuel, the final products of CH, OH, and other species are used to calculate CH* and OH* with detailed sub-mechanisms. As mentioned in previous chapters, the main formation reactions for CH* and OH* are as:



There are several reactions in quenching and relaxing processes that should be mentioned and considered. The mechanisms used to evaluate CH* and OH* are presented in the following tables, which contain formation and quenching reactions with their reaction rate coefficients.

Table 5.1: Mechanism 1: CH* and OH* chemiluminescence mechanism from Peeters [Devriendt et al., 1996], Tamura et al. [Tamura et al., 1998], and Walsh et al. [Walsh et al., 1998]. [$k = AT^B \exp\left(\frac{-E_a}{RT}\right)$]

No.	Reactions	A	B	E_a	Ref.
1	$C_2H + O \rightleftharpoons CH^* + CO$	1.08×10^{13}	0	0	Peeters
2	$C_2H + O_2 \rightleftharpoons CH^* + CO_2$	2.17×10^{10}	0	0	Peeters
3	$CH^* \rightarrow CH + hv$	1.85×10^6	0	0	Tamura
4	$CH^* + H_2O \rightleftharpoons CH + H_2O$	5.3×10^{13}	0	0	Tamura
5	$CH^* + CO_2 \rightleftharpoons CH + CO_2$	2.4×10^{-1}	4.3	-1694	Tamura
6	$CH^* + CO \rightleftharpoons CH + CO$	2.44×10^{12}	0.5	0	Tamura
7	$CH^* + H_2 \rightleftharpoons CH + H_2$	1.47×10^{14}	0	1361	Tamura
8	$CH^* + O_2 \rightleftharpoons CH + O_2$	2.48×10^6	2.14	-1720	Tamura
9	$CH^* + N_2 \rightleftharpoons CH + N_2$	3.03×10^2	3.4	-381	Tamura
10	$CH^* + CH_4 \rightleftharpoons CH + CH_4$	1.73×10^{13}	0	167	Tamura
11	$CH + O_2 \rightleftharpoons CO + OH^*$	3.25×10^{13}	0	0	Walsh
12	$OH^* \rightarrow OH + hv$	1.45×10^6	0	0	Tamura
13	$OH^* + H_2O \rightleftharpoons OH + H_2O$	5.92×10^{12}	0.5	-861	Tamura
14	$OH^* + CO_2 \rightleftharpoons OH + CO_2$	2.75×10^{12}	0.5	-968	Tamura
15	$OH^* + CO \rightleftharpoons OH + CO$	3.23×10^{12}	0.5	-787	Tamura
16	$OH^* + H_2 \rightleftharpoons OH + H_2$	2.95×10^{12}	0.5	-444	Tamura
17	$OH^* + O_2 \rightleftharpoons OH + O_2$	2.1×10^{12}	0.5	-482	Tamura
18	$OH^* + N_2 \rightleftharpoons OH + N_2$	1.08×10^{11}	0.5	-1238	Tamura
19	$OH^* + CH_4 \rightleftharpoons OH + CH_4$	3.36×10^{12}	0.5	-635	Tamura

Table 5.2: Mechanism 2: CH* and OH* chemiluminescence mechanism from Peeters [Devriendt et al., 1996], Tamura et al. [Tamura et al., 1998], and Porter et al. [Porter et al., 1967]. [$k = AT^B \exp\left(\frac{-E_a}{RT}\right)$]

No.	Reactions	A	B	E_a	Ref.
1	$C_2H + O \rightleftharpoons CH^* + CO$	1.08×10^{13}	0	0	Peeters
2	$C_2H + O_2 \rightleftharpoons CH^* + CO_2$	2.17×10^{10}	0	0	Peeters
3	$CH^* \rightarrow CH + hv$	1.85×10^6	0	0	Tamura
4	$CH^* + H_2O \rightleftharpoons CH + H_2O$	5.3×10^{13}	0	0	Tamura
5	$CH^* + CO_2 \rightleftharpoons CH + CO_2$	2.4×10^{-1}	4.3	-1694	Tamura
6	$CH^* + CO \rightleftharpoons CH + CO$	2.44×10^{12}	0.5	0	Tamura
7	$CH^* + H_2 \rightleftharpoons CH + H_2$	1.47×10^{14}	0	1361	Tamura
8	$CH^* + O_2 \rightleftharpoons CH + O_2$	2.48×10^6	2.14	-1720	Tamura
9	$CH^* + N_2 \rightleftharpoons CH + N_2$	3.03×10^2	3.4	-381	Tamura
10	$CH^* + CH_4 \rightleftharpoons CH + CH_4$	1.73×10^{13}	0	167	Tamura
11	$CH + O_2 \rightleftharpoons CO + OH^*$	6.0×10^{10}	0	0	Porter
12	$OH^* \rightarrow OH + hv$	1.45×10^6	0	0	Tamura
13	$OH^* + H_2O \rightleftharpoons OH + H_2O$	5.92×10^{12}	0.5	-861	Tamura
14	$OH^* + CO_2 \rightleftharpoons OH + CO_2$	2.75×10^{12}	0.5	-968	Tamura
15	$OH^* + CO \rightleftharpoons OH + CO$	3.23×10^{12}	0.5	-787	Tamura
16	$OH^* + H_2 \rightleftharpoons OH + H_2$	2.95×10^{12}	0.5	-444	Tamura
17	$OH^* + O_2 \rightleftharpoons OH + O_2$	2.1×10^{12}	0.5	-482	Tamura
18	$OH^* + N_2 \rightleftharpoons OH + N_2$	1.08×10^{11}	0.5	-1238	Tamura
19	$OH^* + CH_4 \rightleftharpoons OH + CH_4$	3.36×10^{12}	0.5	-635	Tamura

Table 5.3: Mechanism 3: CH* and OH* chemiluminescence mechanism from Peeters [Elsamara et al., 2005], Tamura et al. [Tamura et al., 1998], and Porter et al. [Porter et al., 1967]. [$k = AT^B \exp\left(\frac{-E_a}{RT}\right)$]

No.	Reactions	A	B	E_a	Ref.
1	$C_2H + O \rightleftharpoons CH^* + CO$	6.02×10^{12}	0	457	Elsamara
2	$C_2H + O_2 \rightleftharpoons CH^* + CO_2$	6.02×10^{-4}	4.4	-2285	Elsamara
3	$CH^* \rightarrow CH + hv$	1.85×10^6	0	0	Tamura
4	$CH^* + H_2O \rightleftharpoons CH + H_2O$	5.3×10^{13}	0	0	Tamura
5	$CH^* + CO_2 \rightleftharpoons CH + CO_2$	2.4×10^{-1}	4.3	-1694	Tamura
6	$CH^* + CO \rightleftharpoons CH + CO$	2.44×10^{12}	0.5	0	Tamura
7	$CH^* + H_2 \rightleftharpoons CH + H_2$	1.47×10^{14}	0	1361	Tamura
8	$CH^* + O_2 \rightleftharpoons CH + O_2$	2.48×10^6	2.14	-1720	Tamura
9	$CH^* + N_2 \rightleftharpoons CH + N_2$	3.03×10^2	3.4	-381	Tamura
10	$CH^* + CH_4 \rightleftharpoons CH + CH_4$	1.73×10^{13}	0	167	Tamura
11	$CH + O_2 \rightleftharpoons CO + OH^*$	6.0×10^{10}	0	0	Porter
12	$OH^* \rightarrow OH + hv$	1.45×10^6	0	0	Tamura
13	$OH^* + H_2O \rightleftharpoons OH + H_2O$	5.92×10^{12}	0.5	-861	Tamura
14	$OH^* + CO_2 \rightleftharpoons OH + CO_2$	2.75×10^{12}	0.5	-968	Tamura
15	$OH^* + CO \rightleftharpoons OH + CO$	3.23×10^{12}	0.5	-787	Tamura
16	$OH^* + H_2 \rightleftharpoons OH + H_2$	2.95×10^{12}	0.5	-444	Tamura
17	$OH^* + O_2 \rightleftharpoons OH + O_2$	2.1×10^{12}	0.5	-482	Tamura
18	$OH^* + N_2 \rightleftharpoons OH + N_2$	1.08×10^{11}	0.5	-1238	Tamura
19	$OH^* + CH_4 \rightleftharpoons OH + CH_4$	3.36×10^{12}	0.5	-635	Tamura

Table 5.4: Mechanism 4: CH* and OH* chemiluminescence mechanism from Peeters [Elsamra et al., 2005], Tamura et al. [Tamura et al., 1998], and Carl et al. [Carl et al., 2003]. [$k = AT^B \exp\left(\frac{-E_a}{RT}\right)$]

No.	Reactions	A	B	E_a	Ref.
1	$C_2H + O \rightleftharpoons CH^* + CO$	6.02×10^{12}	0	457	Elsamara
2	$C_2H + O_2 \rightleftharpoons CH^* + CO_2$	6.02×10^{-4}	4.4	-2285	Elsamara
3	$CH^* \rightarrow CH + hv$	1.85×10^6	0	0	Tamura
4	$CH^* + H_2O \rightleftharpoons CH + H_2O$	5.3×10^{13}	0	0	Tamura
5	$CH^* + CO_2 \rightleftharpoons CH + CO_2$	2.4×10^{-1}	4.3	-1694	Tamura
6	$CH^* + CO \rightleftharpoons CH + CO$	2.44×10^{12}	0.5	0	Tamura
7	$CH^* + H_2 \rightleftharpoons CH + H_2$	1.47×10^{14}	0	1361	Tamura
8	$CH^* + O_2 \rightleftharpoons CH + O_2$	2.48×10^6	2.14	-1720	Tamura
9	$CH^* + N_2 \rightleftharpoons CH + N_2$	3.03×10^2	3.4	-381	Tamura
10	$CH^* + CH_4 \rightleftharpoons CH + CH_4$	1.73×10^{13}	0	167	Tamura
11	$CH + O_2 \rightleftharpoons CO + OH^*$	6.0×10^{10}	0	0	Carl
12	$OH^* \rightarrow OH + hv$	1.45×10^6	0	0	Tamura
13	$OH^* + H_2O \rightleftharpoons OH + H_2O$	5.92×10^{12}	0.5	-861	Tamura
14	$OH^* + CO_2 \rightleftharpoons OH + CO_2$	2.75×10^{12}	0.5	-968	Tamura
15	$OH^* + CO \rightleftharpoons OH + CO$	3.23×10^{12}	0.5	-787	Tamura
16	$OH^* + H_2 \rightleftharpoons OH + H_2$	2.95×10^{12}	0.5	-444	Tamura
17	$OH^* + O_2 \rightleftharpoons OH + O_2$	2.1×10^{12}	0.5	-482	Tamura
18	$OH^* + N_2 \rightleftharpoons OH + N_2$	1.08×10^{11}	0.5	-1238	Tamura
19	$OH^* + CH_4 \rightleftharpoons OH + CH_4$	3.36×10^{12}	0.5	-635	Tamura

Generally, radicals have low concentrations in flames, because they have a low rate of formation and a rapid rate of removal and quenching. The concentrations were evaluated as a post-process to the flame simulation, and assumed to be in a quasi-steady state, having little overall effect on the total kinetics. Concentrations of species can be calculated by

using the formation and removal reaction rates. The following equation is for measuring the concentration of CH^* (moles/cm³) and OH^* :

$$[CH^*] = \frac{k_1[C_2H][O] + k_2[C_2H][O_2]}{\sum_j k_{Q,j}[M_j] + A_c} \quad (5.4)$$

$$[OH^*] = \frac{k_3[CH][O_2]}{\sum_j k_{Q,j}[M_j] + A_c} \quad (5.5)$$

Where K_1 and K_2 are the reaction constant rates for two formation reactions (R1 and R2), $k_{Q,j}$ is the quenching rate constant by species j , and A_c is the Einstein coefficient for spontaneous emission. K_3 is the constant reaction rate for formation reaction R3. The photon emission rate, i (mole photon, cms) is calculated by:

$$i_{CH^*} = A_c[CH^*] \quad (5.6)$$

$$i_{OH^*} = A_c[OH^*] \quad (5.7)$$

The profiles through the 1D simulation are integrated to calculate the full spatial formation of each species, I_{CH^*} (Photons cm⁻² s⁻¹), where L is the integration path length across the 1D domain:

$$I_{CH^*} = \int i_{CH^*} dx \quad (5.8)$$

The total emission rate, P (Photons/s), is given by the flame area, and can be derived by:

$$P_{CH^*} = I_{CH^*} \times A_f = I_{CH^*} \frac{m}{\rho u S_L} \quad (5.9)$$

Normalized by the fuel mass flow rate:

$$\frac{P_{(CH^*)}}{\dot{m}_f} = I_{(CH^*)} \left(\frac{1 + \frac{\dot{m}_a}{\dot{m}_f}}{\rho_u S_L} \right) \quad (5.10)$$

$$\frac{P_{(OH^*)}}{\dot{m}_f} = I_{(OH^*)} \left(\frac{1 + \frac{\dot{m}_a}{\dot{m}_f}}{\rho_u S_L} \right) \quad (5.11)$$

These equations are presented to calculate the concentration of radical species. As shown in the equations, these radical species depend on the concentration of species, which can be measured through detailed mechanisms. Each fuel has its own specific mechanisms that predict intermediate and final species.

Detailed chemical and kinetic calculations were done for a one-dimensional, unstrained, adiabatic premixed flame in CHEMKIN for methane, JP-8 kerosene, and dodecane. For methane, the GRI-mech 3 mechanism [Smith et al., 2011] with 325 reactions and 53 species was used. The HyChem Fuel A1 (JP-8) detailed mechanism [Wang et al., 2018, Xu et al., 2018] was utilized to simulate the combustion of JP-8. Finally, for dodecane, the JetSurf 2 [Wang et al., 2010] detailed high-temperature chemistry mechanism of all n-alkanes up to n-dodecane, which contains 2163 reactions and 348 species, was employed. The simulations have been done for temperatures of 300K and 470K and an equivalence ratio of 0.6 to 1.2. The results from CHEMKIN are post-processed with different CH* and OH* sub-mechanisms to evaluate each radical concentration.

5.4 Comparison to Mechanisms

Initially, I aim to depict the simulated distribution of different species for the combustion of each fuel. Then, by utilizing various sub-mechanisms for CH* and OH*, it is possible to determine which sub-mechanism can predict these species.

Preliminary CHEMKIN simulations using JetSurf2.0 [Wang et al., 2010] are given below in Figure 2-4 for a freely propagating dodecane flame at ambient temperature and

pressure. The JetSurf mechanism inherently calculates the species concentrations of CH^* and OH^* using the built-in model reactions by Renlund [Renlund et al., 1982] and Hall and Petersen [Hall and Petersen, 2006]. Figure 5.1 depicts the spatial structure of combustion intermediates of formaldehyde, HCO, CH, and OH. The structure of these profiles provides information on the low-temperature preheat zones, reacting layers, and post-flame heat release. Using the intermediate species profiles and the modeling approaches, profiles for CH^* and OH^* can also be computed as given in Figures 5.2 and 5.3. The integration of these profiles of chemiluminescent species can then be used for comparison against the measured spectroscopic quantities from experiments.

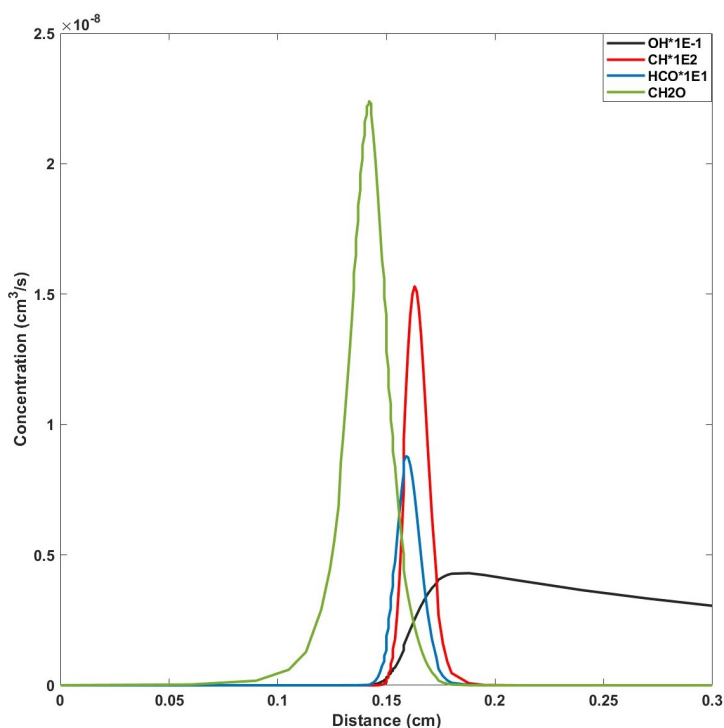


Figure 5.1: Spatial structure of combustion intermediates of formaldehyde, HCO, CH, and OH in a freely propagating n-Dodecane flame

Figure 5.2 shows the distribution of radical CH within a freely propagating rich n-Dodecane flame, obtained from equilibrium condition, as described before. The concentration of radical CH is two orders smaller than the CH. Figure 5.3 expresses the distribution of OH and radical OH, which was measured similarly to radical CH. OH radical concentration is 8

degrees smaller than OH species concentration.

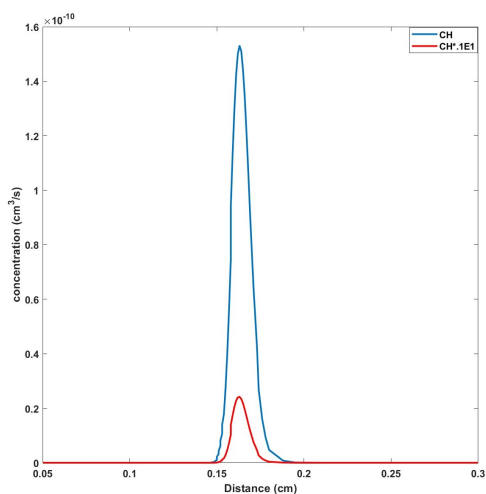


Figure 5.2: Spatial structure of combustion intermediate CH and CH* in a freely propagating n-Dodecane flame

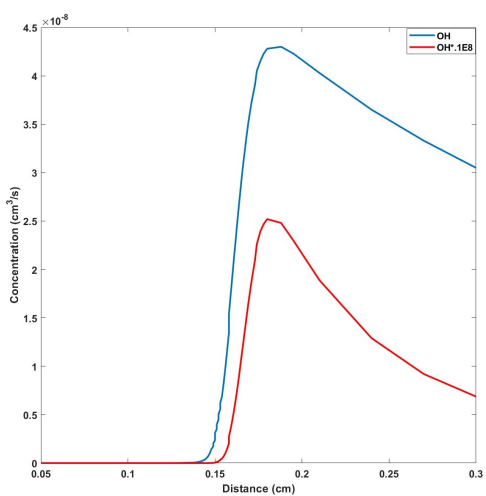


Figure 5.3: Spatial structure of combustion intermediate OH and OH* in a freely propagating n-Dodecane flame

The four mechanisms presented in Tables 1 to 4 are suggested sub-mechanisms to predict OH* and CH*. In addition, the JetSurf chemical mechanism includes a built-in sub-mechanism for CH* and OH* excited species. The results for the ratios of CH*/OH* are representative of the combination of sub-mechanisms included in the above table for each pairing of CH* or OH*.

Figure 5.4 depicts the normalized signal values of CH^* measured during experiments for different fuels and equivalence ratios. As can be seen, the CH^* signal level increases with the equivalence ratio for all fuels, however, the rate of increase is higher for liquid fuels compared to methane. The heavy hydrocarbon liquid fuels seem to produce higher CH^* compared to methane. This can be due to the multi-component effect and more CH formation elements within the fuels.

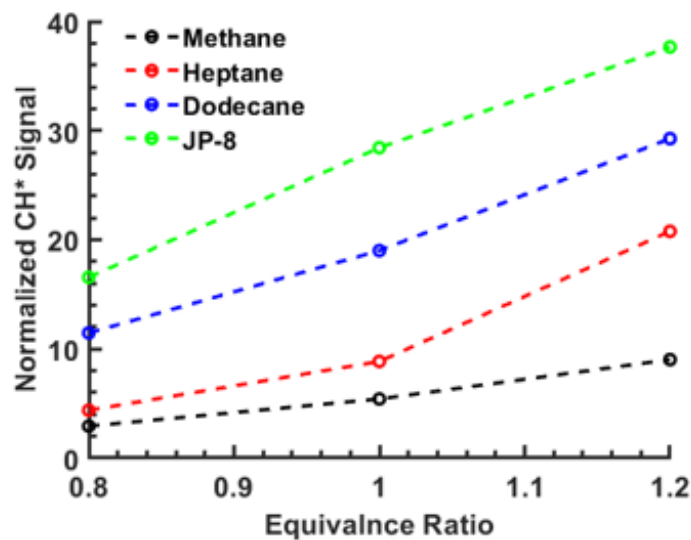


Figure 5.4: Experimental normalized values of measured CH^* signal for fuels at different equivalence ratio

The measurement of CH^* with simulation tools such as CHEMKIN is tested to evaluate whether the sub-mechanisms can predict the CH^* production for each fuel. Figure 5.5 shows the CH^* measurements with two different sub-mechanisms introduced by Peeters and Elsamra. For CH , as Figure 5.5 shows, the sub-mechanism simulations do not predict the experimental trend. The experiments follow the expected trend where heavy hydrocarbon fuels have a higher CH^* signal than lighter fuels like methane. However, the simulation is not capable of predicting the correct trend.

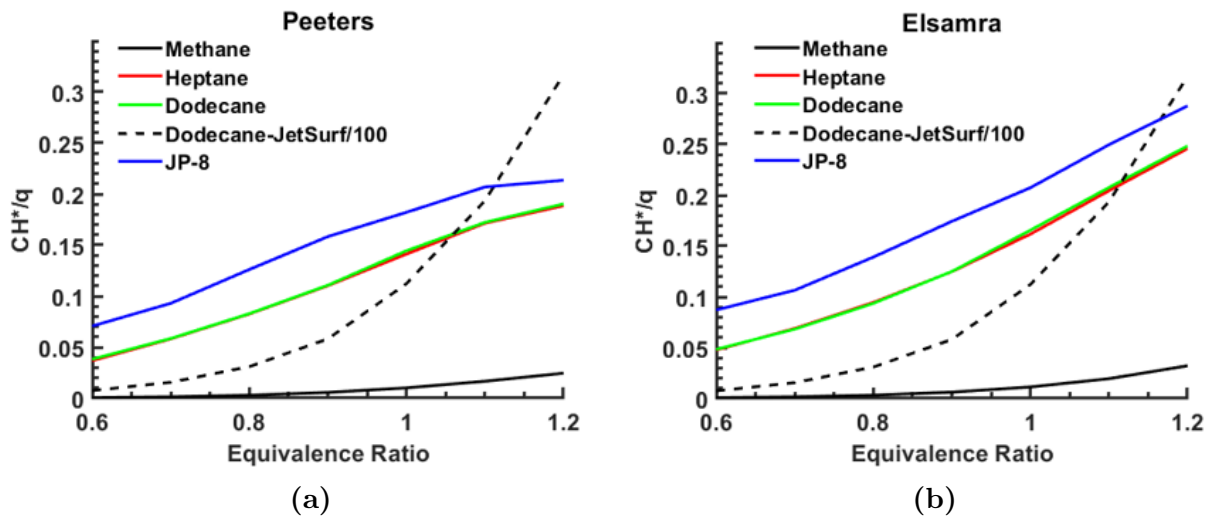


Figure 5.5: simulation measurement of CH^* signal based on (a) Peeters and (b) Elsamra sub-mechanisms for fuels at different equivalence ratios

The other important intermediate species of interest is OH. Figure 5.6 shows the experimental signals of OH^* captured for different fuels at different equivalence ratios. The trend of OH is pretty similar to CH^* distribution. As the equivalence ratio increases, the OH^* signal increases as well. The level of OH^* signal is higher for liquid fuels than methane, which can be due to several reasons. The multi-component fuels break apart into smaller species and produce many more reactions compared to methane. These reactions can lead to excessive production of CH^* compared to methane at the same equivalence ratios.

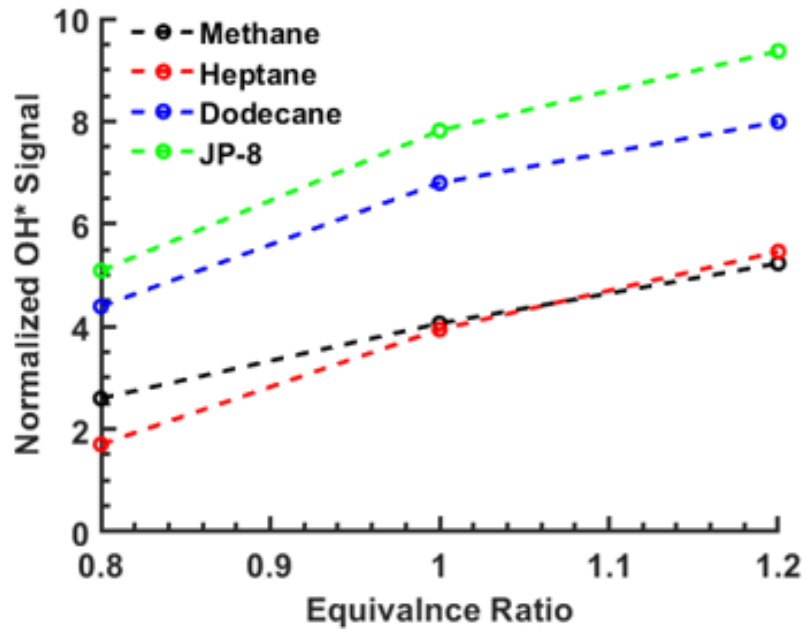


Figure 5.6: Experimental normalized values of measured OH* signal for fuels at different equivalence ratio

For the evaluation of sub-mechanisms, the same procedure is used for the calculation of the OH signal. Figure 5.7 shows the different sub-mechanisms' capability to predict the OH* values for different fuels. Similar to CH*, the trend of sub-mechanism OH* does not follow the experimental measurements. It seems all sub-mechanisms can follow the experimental trend with equivalence ratios. However, the sub-mechanisms are not capable of distinguishing the effect of fuels. The prediction of all of the sub-mechanisms for liquid fuels is similar to each other.

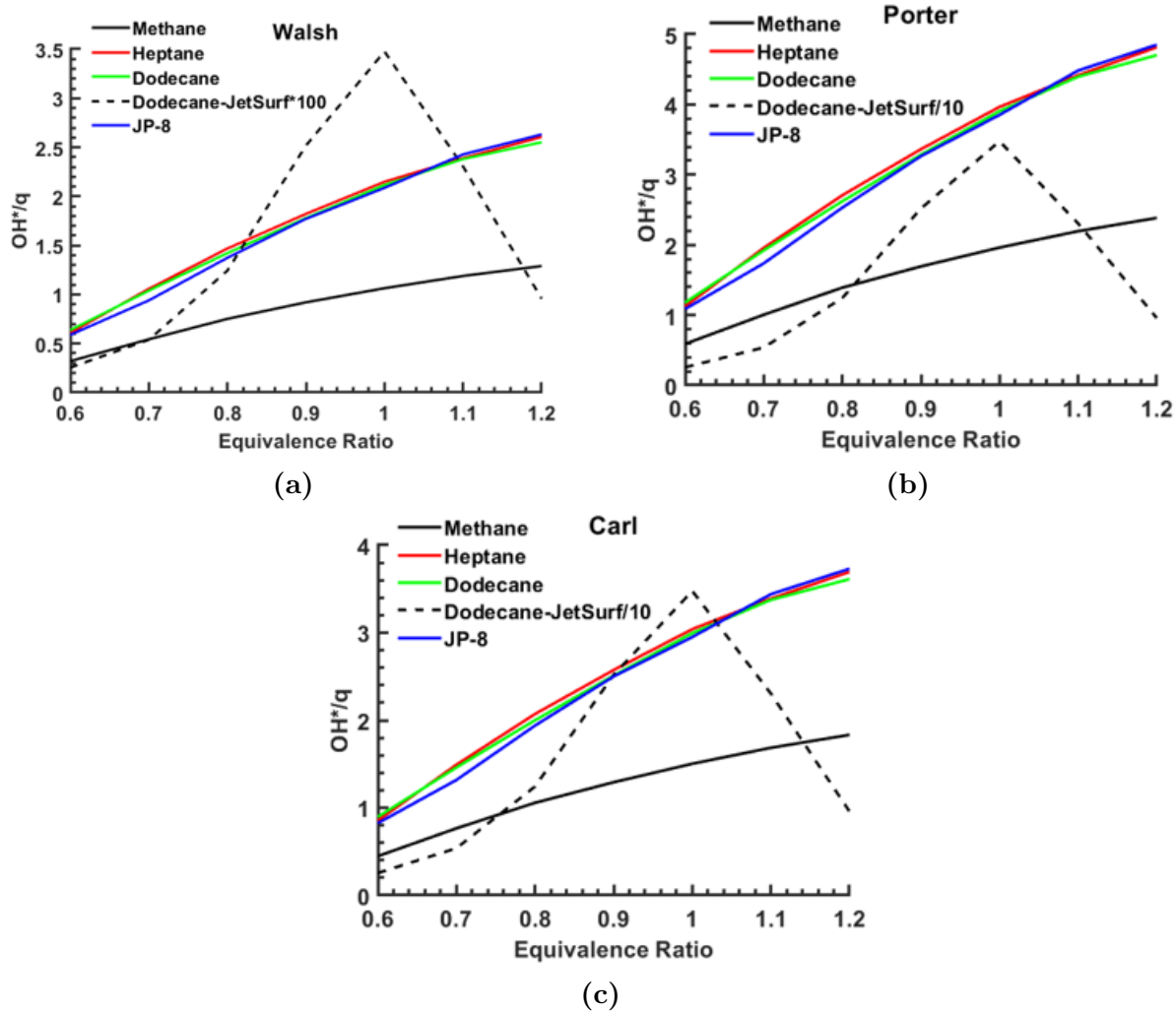


Figure 5.7: simulation measurement of OH* signal based on (a) Walsh, (b) Porter, and (c) Carl sub-mechanisms for fuels at different equivalence ratio

The ratio of CH*/OH* in different equivalence ratios is shown in Figure 5.8. This ratio is significantly higher for liquid fuels at any given equivalence ratio. It shows that by increasing the equivalence ratio, the ratio of CH*/OH* increases as well, and the rate of increase is higher for liquid fuels compared to methane.

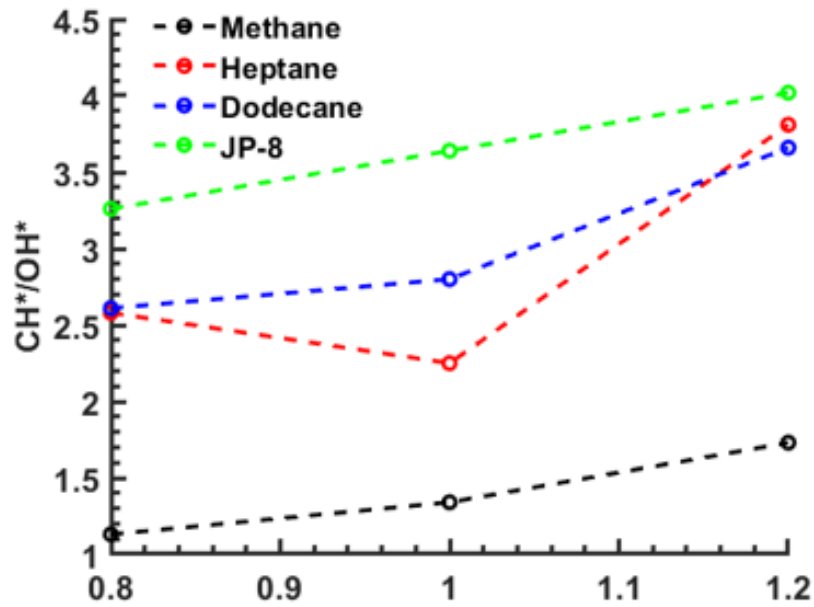


Figure 5.8: Experimental values of CH^*/OH^* for fuels at different equivalence ratio

Figure 5.9 shows the simulated ratio of CH^*/OH^* for different sub-mechanisms for fuels at different equivalence ratios. As it is shown, the ratio of CH^*/OH^* does not follow any specific trend with the equivalence ratio, compared to experimental results, where the ratio of CH^*/OH^* increases with the equivalence ratio.

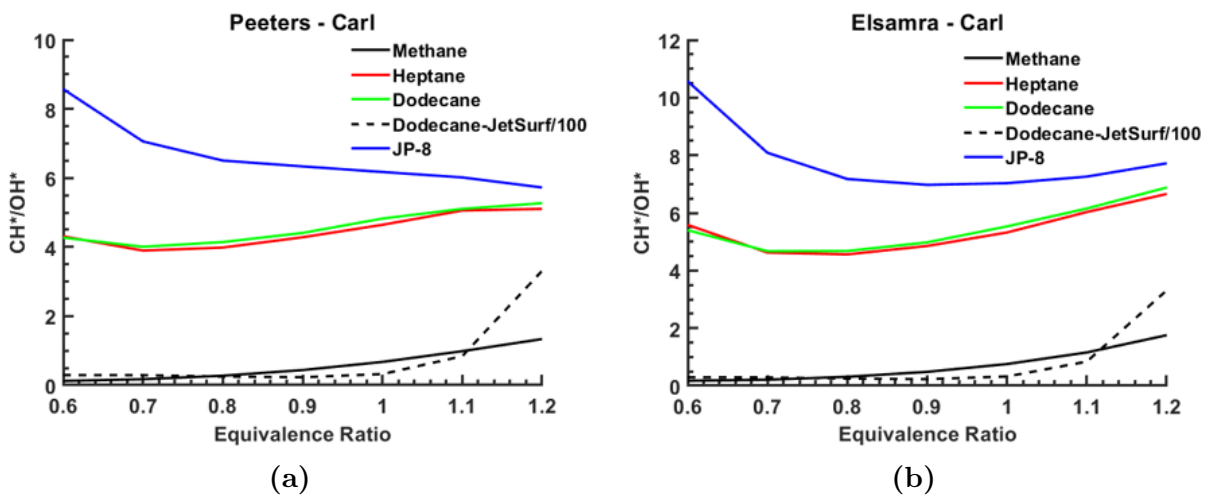


Figure 5.9: simulation measurement of CH^*/OH^* based on (a) Peeters-Carl, (b) Elsamra-Carl sub-mechanisms for fuels at different equivalence ratio

The sub-mechanism built into JETSURF 2 is not capable of predicting either CH* or OH* like other sub-mechanisms. The predicted CH and OH measurements do not match experimental values. These results show the failure of chemical mechanisms to predict CH and OH and indicate the necessity of further investigation into intermediate species and finding a better mechanism to represent CH/OH chemiluminescence more accurately.

Chapter 6

Summary and Discussion

In this thesis, I investigated the complexities of liquid fuel combustion in aerospace applications, particularly focusing on the challenges posed by gas turbines. Liquid fuel combustion differs significantly from gaseous fuel combustion due to factors such as the slower vaporization rate, complex fuel composition, and the turbulent nature of combustion. These factors present unique challenges in achieving flame stabilization, understanding droplet interactions, and defining the flammability limits of fuel mixtures, especially under varying turbulent conditions. Traditional diagnostic methods like chemiluminescence and Planar Laser-Induced Fluorescence (PLIF) have faced limitations in studying liquid fuels, particularly due to issues like signal interference from droplets and the low intensity of emissions from the combustion process.

To address these challenges, our research aimed to develop advanced diagnostic techniques and computational models to improve the accuracy of flame diagnostics and gain a deeper understanding of turbulent liquid fuel combustion. A key innovation introduced in this work is the use of CH PLIF for effectively capturing flame structures and extinction events, without being affected by the interference of liquid droplets. This was achieved through collaboration with the Air Force Research Laboratory (AFRL), which allowed us to develop and implement a new diagnostic methodology. In addition to CH PLIF, I introduced a nu-

merical image processing algorithm to enhance the accuracy of flame structure measurements, particularly focusing on turbulence, flame curvature, and local extinction events.

Throughout the study, several experimental approaches were applied to measure turbulent flame characteristics and understand the influence of parameters such as equivalence ratio, fuel composition, and turbulence intensity on combustion dynamics. I found that liquid fuels exhibit higher local extinction frequencies and larger flame breaks compared to methane flames, indicating that flame behavior in liquid fuels is affected by factors beyond turbulence intensity alone. The flame surface density (FSD) of liquid fuels was found to be significantly different from that of methane, especially under lean conditions, which highlighted the importance of accurate diagnostic techniques that account for flame breaks and extinction events.

Another major aspect of the research was to understand the influence of liquid fuel sprays on flame structure. Our study showed that adding liquid sprays to methane and n-Heptane flames increases CH concentrations and alters the signal distribution, resulting in higher CH emissions, especially in highly turbulent conditions. However, I also found that the addition of liquid sprays leads to more complex flame structures, characterized by increased flame wrinkling and surface instability. These effects varied with the turbulence intensity and spray flow rate, which ultimately determined the balance between flame enhancement and quenching. The results highlighted the complexity of droplet interactions with the flame and the impact of turbulence on the combustion process.

In addition, I explored the role of chemiluminescence as a diagnostic tool for studying combustion phenomena in heavy hydrocarbon fuels such as kerosene, JP-8, and n-Dodecane. Chemiluminescence is widely used in industrial combustion studies due to its simplicity and cost-effectiveness. However, I found discrepancies between the experimental measurements of CH^*/OH^* ratios and those predicted by the chemical mechanisms for heavier fuels. This indicated that the existing chemical models might not fully capture the intermediate species formation and reaction pathways for heavy fuels. Therefore, the study emphasized the need

for further refinement of chemical mechanisms to improve the accuracy of combustion models for heavy liquid fuels.

The research also identified several limitations in existing diagnostic methods. For example, background emissions from CO_2 and C_2 significantly affect the accuracy of CH chemiluminescence measurements. To mitigate this, I developed techniques to subtract the contributions of these interfering species, and I emphasized the use of narrower optical filters to improve measurement accuracy. These improvements allowed for more precise determination of CH concentrations, which is critical for understanding the combustion characteristics of heavy hydrocarbon fuels.

Overall, the research presented in this thesis provides significant advancements in the study of liquid fuel combustion. By developing advanced diagnostic tools, refining computational models, and addressing the challenges of measuring turbulent flame characteristics, this work contributes to the optimization of combustion processes in aerospace applications. The findings from this study can lead to improved combustion efficiency, stability, and reduced emissions in liquid-fuel-based systems, which are essential for the development of more efficient and environmentally friendly propulsion technologies.

6.1 Key Results and Conclusions:

- This is the first application of C-X CH PLIF for any liquid fuel and represents the highest-signal to noise imaging of CH for these fuels. This is the first time that local extinctions have been visualized in liquid fuels.
- Developed a novel CH PLIF diagnostic technique to effectively visualize flame structures and detect extinction events without droplet interference.
- The ability to perform CH PLIF in liquid fuels, both spray and prevaporized, is novel and useful in the access to extinction data which is not accurately captured on OH PLIF. The OH species is longer lived even after a local extinction has occurred and is therefore not necessarily an accurate marker of when extinctions occur. However, CH

is a short-lived molecule exclusively produced in the heat release region of the flame thickness, whose presence directly indicate reaction or quenched processes.

- Created a numerical algorithm and the OH Pseudo method to enhance the accuracy of flame structure measurements, addressing limitations in traditional PLIF techniques.
- Demonstrated that liquid fuels exhibit higher local flame extinction frequencies and longer flame breaks compared to methane flames, highlighting the impact of fuel properties on flame behavior.
- Higher and lower CH PLIF signals are observed in regions of high positive versus high negative curvature. The value CH PLIF signal is controlled with the concentration of the CH radical which correlated with the local heat release value. Thus, varying CH fluorescence is indicative or vary heat release. This curvature driven variance is a Lewis number effect and not observed strongly in methane flames because the Le is approximately equal to 1. This is the first experimental observation of Lewis number curvature effects in liquid fuels, which is corroborated by DNS calculations of other liquid fuels.
- Where the fluorescence signal of CH is low is correlated with a lower heat release and even extinction of the flame surface. This is a new extinction mechanism for liquid fuels, with larger Le number, that has only been previously seen in hydrogen which has a low Le number.
- Found that flame surface density (FSD) is significantly affected by fuel type and flame conditions, with methane showing higher FSD under lean conditions compared to liquid fuels.
- Showed that adding liquid sprays leads to higher CH concentrations and increased flame wrinkling, indicating more complex and unstable flame structures, depending on turbulence intensity and spray flow rate.
- Identified discrepancies between experimental and simulated CH^*/OH^* ratios for heavy

hydrocarbon fuels, indicating the need for further refinement of chemical models.

- The primary conclusion of the chemiluminescence effort suggest that the chemical mechanism for the heavy fuels should not be trusted to accurately account for chemiluminescence differences in fuels. The general experimental trend shows that heavier fuels generate more CH^* and OH^* , which is not predicted by the calculations.
- In fact, particularly for OH^* , chemical mechanisms predict the same production of radical signal for three different fuels since the same concentration of chemiluminescent reactants are predicted for each fuel. Thus, the mechanisms are unable to distinguish even between different liquid fuels.
- Highlighted the role of turbulence intensity and fuel composition in determining the balance between flame enhancement and quenching in liquid fuel sprays.

These results provide critical insights into the combustion dynamics of liquid fuels, offering guidelines for optimizing combustion processes in aerospace propulsion systems and contributing to the development of more efficient and stable combustion technologies.

6.2 Next Steps

For future work, several avenues could be pursued to advance the understanding of chemiluminescence in heavy hydrocarbon fuels. One approach would be to refine the existing chemical mechanisms further by incorporating a broader range of intermediate species and quenching reactions. This could involve developing more sophisticated models that account for the detailed interactions between fuel components, radicals, and other intermediates during combustion. Integrating these mechanisms into higher-dimensional simulations, such as 2D and 3D turbulent flame models, could also provide a more comprehensive understanding of how these fuels behave under realistic flow conditions.

Additionally, future work should aim to improve the accuracy of experimental measurements by developing new diagnostic tools or refining current ones. For example, using

more advanced spectrometers with narrower optical filters could help reduce interference from species like CO_2 and C_2 , providing a clearer signal for CH and OH chemiluminescence. Furthermore, implementing more advanced image-processing techniques to separate overlapping emissions could enhance the resolution and reliability of the collected data.

Another potential direction would be to expand the scope of the research to include other heavy fuels, such as alternative and sustainable biofuels. Investigating the chemiluminescence characteristics of these fuels could provide insights into their combustion properties, helping optimize their use in propulsion systems and industrial applications. Comparing these findings with traditional fuels like JP-8 could also support the development of generalized models applicable across a wider range of fuel types.

Incorporating computational fluid dynamics (CFD) models with refined chemiluminescence mechanisms could also help predict flame behavior more accurately in practical combustion systems. Integrating these models with real-world data would enable the development of robust predictive capabilities that can guide the design and optimization of industrial combustion systems, such as power plants and aerospace engines, to enhance their efficiency and reduce emissions. Collaborating with industry partners could facilitate the transfer of these refined diagnostic and computational techniques from the laboratory to industrial applications, broadening the impact of this research.

Attributions and Other Contributions

Chapters of this work are extended text based on several manuscripts that were authored by Amirreza Gandomkar: [Gandomkar et al., 2020, Gandomkar et al., 2021b, Gandomkar et al., 2021a, Gandomkar et al., 2021c]. Two additional articles on prevaporized and spray liquid fuels are currently prepared for submission and are expected to be published in the near future.

Chapter 2

This chapter is based on work done in collaboration with Savvas Gkantonas [Gandomkar et al., 2021a]. Both authors contributed equally to the initial development of the methodology of flame edge detection. Gandomkar resumed the initial draft and finalized the algorithms to measure flame statistics.

Chapter 3

This chapter is based on unpublished work done in collaboration with Dr. Campbell Carter and Thomas A McManus from Air Force Research Laboratory. This research was inspired by the original study on liquid fuels [McManus et al., 2021]. Most of the prevaporized liquid fuels experiments were conducted by Dr. Allison and Dr. Carter in the AFRL. Gandomkar contributed to the original text, image processing, data analysis, and experimental design.

Chapter 4

This chapter is based on work done in collaboration with Dr. Campbell Carter from Air Force Research Laboratory. Most of the spray liquid fuels experiments were conducted by Dr. Allison and Dr. Carter in the AFRL¹. Gandomkar contributed to the original text, image processing, data analysis, and experimental design.

¹Air Force Research Laboratory

Chapter 5

This chapter is based on work done in collaboration with John Schihl [Gandomkar et al., 2020] and another unpublished research. Both authors contributed equally to the final text of the original manuscript, data collection and analysis, and experimental design. Schihl contributed to the experiment data acquisition. Gandomkar provided CHEMKIN simulation results and the final figures.

BIBLIOGRAPHY

- [Aspden et al., 2017] Aspden, A., Bell, J., Day, M., and Egolfopoulos, F. (2017). Turbulence–flame interactions in lean premixed dodecane flames. *Proceedings of the Combustion Institute*, 36(2):2005–2016.
- [Borghi, 1985] Borghi, R. (1985). On the structure and morphology of turbulent premixed flames. In *Recent Advances in the Aerospace Sciences: In Honor of Luigi Crocco on His Seventy-fifth Birthday*, pages 117–138. Springer.
- [Carl et al., 2003] Carl, S., Van Poppel, M., and Peeters, J. (2003). Identification of the $\text{CH} + \text{O}_2 \rightarrow \text{OH} + \text{CO}$ reaction as the source of $\text{OH}(\text{A})$ chemiluminescence in $\text{C}_2\text{H}_2/\text{O}_2/\text{H}_2\text{O}$ atomic flames and determination of its absolute rate constant over the range $T = 296$ to 511 K. *The Journal of Physical Chemistry A*, 107(50):11001–11007.
- [Carter et al., 2014] Carter, C. D., Hammack, S., and Lee, T. (2014). High-speed planar laser-induced fluorescence of the CH radical using the $\text{C}^2\Sigma^+ \leftarrow \text{X}^2\Pi(0, 0)$ band. *Applied Physics B*, 116:515–519.
- [Carter et al., 2016] Carter, C. D., Hammack, S., and Lee, T. (2016). High-speed flamefront imaging in premixed turbulent flames using planar laser-induced fluorescence of the $\text{CH}(\text{C-X})$ band. *Combustion and Flame*, 168:66–74.
- [Chakraborty and Cant, 2005] Chakraborty, N. and Cant, R. (2005). Influence of Lewis number on curvature effects in turbulent premixed flame propagation in the thin reaction zones regime. *Physics of Fluids*, 17(10).
- [Chen, 2007] Chen, Y.-C. (2007). Measurements of flame-front curvature based on Fourier transformation. *Combustion Theory and Modelling*, 11(3):333–349.
- [Devriendt et al., 1996] Devriendt, K., Van Look, H., Ceursters, B., and Peeters, J. (1996). Kinetics of formation of chemiluminescent $\text{CH}(\text{A})$ by the elementary reactions of $\text{C}_2\text{H} + \text{H}$ ($\text{X} + \text{C}_2\text{H} \rightarrow \text{C}_2 + \text{H}$) with O and O_2 ($\text{X} + \text{O}_2 \rightarrow \text{O} + \text{O}_2$): A pulse laser photolysis study. *Chemical Physics Letters*, 261(4-5):450–456.
- [Driscoll, 2008] Driscoll, J. F. (2008). Turbulent premixed combustion: Flamelet structure and its effect on turbulent burning velocities. *Progress in Energy and Combustion Science*, 34(1):91–134.
- [Elsamra et al., 2005] Elsamra, R. M., Vranckx, S., and Carl, S. A. (2005). $\text{CH}(\text{A})$ formation in hydrocarbon combustion: The temperature dependence of the rate constant of the reaction $\text{C}_2\text{H} + \text{O}_2 \rightarrow \text{CH}(\text{A}) + \text{CO}_2$. *The Journal of Physical Chemistry A*, 109(45):10287–10293.

- [Falkenstein et al., 2020] Falkenstein, T., Kang, S., and Pitsch, H. (2020). Analysis of premixed flame kernel/turbulence interactions under engine conditions based on direct numerical simulation data. *Journal of Fluid Mechanics*, 885:A32.
- [Gandomkar et al., 2021a] Gandomkar, A., Gkantonas, S., Schihl, J., McManus, T. A., Carter, C., and Allison, P. M. (2021a). Non-unity lewis number effects on curvature statistics in prevaporized, turbulent liquid fuel jet flames: Curvature calculation methodology.
- [Gandomkar et al., 2021b] Gandomkar, A., Gkantonas, S., Schihl, J., McManus, T. A., Carter, C. D., and Allison, P. M. (2021b). Fuel effects on turbulent premixed jet flame topology as resolved by ch plif imaging. In *AIAA Scitech 2021 Forum*, page 0079.
- [Gandomkar et al., 2021c] Gandomkar, A., Gkantonas, S., Svoboda, A., McManus, T. A., Carter, C., and Allison, P. M. (2021c). New perspectives of turbulent flame structure via ch plif in prevaporized liquid fuels.
- [Gandomkar et al., 2020] Gandomkar, A., Schihl, J., and Allison, P. M. (2020). Applicability of flame chemiluminescence from liquid, heavy-hydrocarbon fuels. In *AIAA Scitech 2020 Forum*, page 0523.
- [García-Armingol and Ballester, 2014] García-Armingol, T. and Ballester, J. (2014). Influence of fuel composition on chemiluminescence emission in premixed flames of ch₄/co₂/h₂/co blends. *International journal of hydrogen energy*, 39(35):20255–20265.
- [Guethe et al., 2012] Guethe, F., Guyot, D., Singla, G., Noiray, N., and Schuermans, B. (2012). Chemiluminescence as diagnostic tool in the development of gas turbines. *Applied Physics B*, 107:619–636.
- [Guiberti et al., 2017] Guiberti, T., Durox, D., and Schuller, T. (2017). Flame chemiluminescence from co₂-and n₂-diluted laminar ch₄/air premixed flames. *Combustion and Flame*, 181:110–122.
- [Guyot et al., 2010] Guyot, D., Guethe, F., Schuermans, B., Lacarelle, A., and Paschereit, C. O. (2010). Ch/oh chemiluminescence response of an atmospheric premixed flame under varying operating conditions. In *Turbo Expo: Power for Land, Sea, and Air*, volume 43970, pages 933–944.
- [Hall and Petersen, 2006] Hall, J. M. and Petersen, E. L. (2006). An optimized kinetics model for oh chemiluminescence at high temperatures and atmospheric pressures. *International journal of chemical kinetics*, 38(12):714–724.
- [Hammack et al., 2018] Hammack, S. D., Skiba, A. W., Lee, T., and Carter, C. D. (2018). Ch plif and piv implementation using cx (0, 0) and intra-vibrational band filtered detection. *Applied Physics B*, 124:1–5.

- [Haq et al., 2002] Haq, M., Sheppard, C., Woolley, R., Greenhalgh, D., and Lockett, R. (2002). Wrinkling and curvature of laminar and turbulent premixed flames. *Combustion and Flame*, 131(1-2):1–15.
- [Hardalupas and Orain, 2004] Hardalupas, Y. and Orain, M. (2004). Local measurements of the time-dependent heat release rate and equivalence ratio using chemiluminescent emission from a flame. *Combustion and Flame*, 139(3):188–207.
- [Higgins et al., 2001] Higgins, B., McQuay, M., Lacas, F., Rolon, J.-C., Darabiha, N., and Candel, S. (2001). Systematic measurements of oh chemiluminescence for fuel-lean, high-pressure, premixed, laminar flames. *Fuel*, 80(1):67–74.
- [Hossain and Nakamura, 2014] Hossain, A. and Nakamura, Y. (2014). A numerical study on the ability to predict the heat release rate using ch chemiluminescence in non-sooting counterflow diffusion flames. *Combustion and flame*, 161(1):162–172.
- [Jenkins and Cant, 2002] Jenkins, K. and Cant, R. (2002). Curvature effects on flame kernels in a turbulent environment. *Proceedings of the Combustion Institute*, 29(2):2023–2029.
- [Kim and Pitsch, 2007] Kim, S. H. and Pitsch, H. (2007). Scalar gradient and small-scale structure in turbulent premixed combustion. *Physics of Fluids*, 19(11).
- [Lachaux et al., 2005] Lachaux, T., Halter, F., Chauveau, C., Gökalp, I., and Shepherd, I. G. (2005). Flame front analysis of high-pressure turbulent lean premixed methane–air flames. *Proceedings of the Combustion Institute*, 30(1):819–826.
- [Lauer and Sattelmayer, 2010] Lauer, M. and Sattelmayer, T. (2010). On the adequacy of chemiluminescence as a measure for heat release in turbulent flames with mixture gradients.
- [Lee and Seo, 2015] Lee, H. and Seo, S. (2015). Experimental study on spectral characteristics of kerosene swirl combustion. *Procedia Engineering*, 99:304–312.
- [Lemaire et al., 2009] Lemaire, R., Faccinetto, A., Therssen, E., Ziskind, M., Focsa, C., and Desgroux, P. (2009). Experimental comparison of soot formation in turbulent flames of diesel and surrogate diesel fuels. *Proceedings of the Combustion Institute*, 32(1):737–744.
- [Li et al., 2010] Li, Z., Li, B., Sun, Z., Bai, X.-S., and Aldén, M. (2010). Turbulence and combustion interaction: High resolution local flame front structure visualization using simultaneous single-shot plif imaging of ch, oh, and ch₂o in a piloted premixed jet flame. *Combustion and Flame*, 157(6):1087–1096.
- [McManus et al., 2021] McManus, T. A., Gandomkar, A., Carter, C. D., and Allison, P. M. (2021). Topological imaging of turbulent premixed, prevaporized liquid fuel jet flames using ch (cx) band plif. *Proceedings of the Combustion Institute*, 38(2):3049–3056.

- [Meyer et al., 2005] Meyer, T. R., Roy, S., Belovich, V. M., Corporan, E., and Gord, J. R. (2005). Simultaneous planar laser-induced incandescence, oh planar laser-induced fluorescence, and droplet mie scattering in swirl-stabilized spray flames. *Applied optics*, 44(3):445–454.
- [Mitsingas et al., 2019] Mitsingas, C. M., Hammack, S. D., Mayhew, E. K., Rajasegar, R., McGann, B., Skiba, A. W., Carter, C. D., and Lee, T. (2019). Simultaneous high speed piv and ch plif using r-branch excitation in the $c2\sigma+x2\pi$ (0, 0) band. *Proceedings of the Combustion Institute*, 37(2):1479–1487.
- [Nori and Seitzman, 2008] Nori, V. and Seitzman, J. (2008). Evaluation of chemiluminescence as a combustion diagnostic under varying operating conditions. In *46th AIAA Aerospace Sciences Meeting and Exhibit*, page 953.
- [Nori and Seitzman, 2009] Nori, V. N. and Seitzman, J. M. (2009). Ch chemiluminescence modeling for combustion diagnostics. *Proceedings of the Combustion Institute*, 32(1):895–903.
- [Otsu, 1979] Otsu, N. (1979). A threshold selection method from gray-level histograms. *IEEE transactions on systems, man, and cybernetics*, 9(1):62–66.
- [Panoutsos et al., 2009] Panoutsos, C., Hardalupas, Y., and Taylor, A. (2009). Numerical evaluation of equivalence ratio measurement using oh and ch chemiluminescence in premixed and non-premixed methane–air flames. *Combustion and Flame*, 156(2):273–291.
- [Paul and Najm, 1998] Paul, P. H. and Najm, H. N. (1998). Planar laser-induced fluorescence imaging of flame heat release rate. In *Symposium (international) on combustion*, volume 27, pages 43–50. Elsevier.
- [Porter et al., 1967] Porter, R., Clark, A., Kaskan, W., and Browne, W. (1967). A study of hydrocarbon flames. In *Symposium (International) on Combustion*, volume 11, pages 907–917. Elsevier.
- [Renlund et al., 1982] Renlund, A., Shokoohi, F., Reisler, H., and Wittig, C. (1982). Reaction of ethynyl radical with oxygen. chemiluminescent products. *The journal of physical chemistry*, 86(21):4165–4170.
- [Renou et al., 1998] Renou, B., Boukhalfa, A., Puechberty, D., and Trinité, M. (1998). Effects of stretch on the local structure of preely propagating premixed low-turbulent flames with various lewis numbers. In *Symposium (International) on Combustion*, volume 27, pages 841–847. Elsevier.
- [Rodrigues et al., 2015] Rodrigues, H. C., Tummers, M. J., van Veen, E. H., and Roekaerts, D. J. (2015). Spray flame structure in conventional and hot-diluted combustion regime. *Combustion and Flame*, 162(3):759–773.

- [Rosell et al., 2017] Rosell, J., Bai, X.-S., Sjöholm, J., Zhou, B., Li, Z., Wang, Z., Pettersson, P., Li, Z., Richter, M., and Alden, M. (2017). Multi-species plif study of the structures of turbulent premixed methane/air jet flames in the flamelet and thin-reaction zones regimes. *Combustion and Flame*, 182:324–338.
- [Rutland and Trouvé, 1993] Rutland, C. and Trouvé, A. (1993). Direct simulations of premixed turbulent flames with nonunity lewis numbers. *Combustion and Flame*, 94(1-2):41–57.
- [Sadiki et al., 2005] Sadiki, A., Chrigui, M., Janicka, J., and Maneshkarimi, M. (2005). Modeling and simulation of effects of turbulence on vaporization, mixing and combustion of liquid-fuel sprays. *Flow, Turbulence and Combustion*, 75:105–130.
- [Savard and Blanquart, 2015] Savard, B. and Blanquart, G. (2015). Broken reaction zone and differential diffusion effects in high karlovitz n-c7h16 premixed turbulent flames. *Combustion and flame*, 162(5):2020–2033.
- [Savard et al., 2015] Savard, B., Bobbitt, B., and Blanquart, G. (2015). Structure of a high karlovitz n-c7h16 premixed turbulent flame. *Proceedings of the Combustion Institute*, 35(2):1377–1384.
- [Savitzky and Golay, 1964] Savitzky, A. and Golay, M. J. (1964). Smoothing and differentiation of data by simplified least squares procedures. *Analytical chemistry*, 36(8):1627–1639.
- [Smith et al., 2011] Smith, G. P., Golden, D. M., Frenklach, M., Moriarty, N. W., Eiteneer, B., Goldenberg, M., Bowman, C. T., Hanson, R. K., Song, S., Gardiner Jr, W., et al. (2011). Gri-mech 3.0, 1999. URL http://www.me.berkeley.edu/gri_mech, 38.
- [Smolke et al., 2018] Smolke, J., Carbone, F., Egolfopoulos, F. N., and Wang, H. (2018). Effect of n-dodecane decomposition on its fundamental flame properties. *Combustion and Flame*, 190:65–73.
- [Smooke et al., 1996] Smooke, M., Ern, A., Tanoff, M., Valdati, B., Mohammed, R., Marran, D., and Long, M. (1996). Computational and experimental study of no in an axisymmetric laminar diffusion flame. In *Symposium (International) on Combustion*, volume 26, pages 2161–2170. Elsevier.
- [Soika et al., 2003] Soika, A., Dinkelacker, F., and Leipertz, A. (2003). Pressure influence on the flame front curvature of turbulent premixed flames: comparison between experiment and theory. *Combustion and flame*, 132(3):451–462.
- [Stepowski et al., 1994] Stepowski, D., Cessou, A., and Goix, P. (1994). Flame stabilization and oh fluorescence mapping of the combustion structures in the near field of a spray jet. *Combustion and flame*, 99(3-4):516–IN1.

- [Tamura et al., 1998] Tamura, M., Berg, P. A., Harrington, J. E., Luque, J., Jeffries, J. B., Smith, G. P., and Crosley, D. R. (1998). Collisional quenching of ch (a), oh (a), and no (a) in low pressure hydrocarbon flames. *Combustion and Flame*, 114(3-4):502–514.
- [Tripathi et al., 2012] Tripathi, M. M., Krishnan, S. R., Srinivasan, K. K., Yueh, F.-Y., and Singh, J. P. (2012). Chemiluminescence-based multivariate sensing of local equivalence ratios in premixed atmospheric methane–air flames. *Fuel*, 93:684–691.
- [Tsushima et al., 1998] Tsushima, S., Saitoh, H., Akamatsu, F., and Katsuki, M. (1998). Observation of combustion characteristics of droplet clusters in a premixed-spray flame by simultaneous monitoring of planar spray images and local chemiluminescence. In *Symposium (international) on combustion*, volume 27, pages 1967–1974. Elsevier.
- [Walsh et al., 1998] Walsh, K., Long, M., Tanoff, M., and Smooke, M. (1998). Experimental and computational study of ch, ch, and oh in an axisymmetric laminar diffusion flame. In *Symposium (international) on combustion*, volume 27, pages 615–623. Elsevier.
- [Wang et al., 2010] Wang, H., E Dames, B Sirjean, D. A. S., R Tango, A Violi, J. Y. W. L., F N Egolfopoulos, D. F. D., R K Hanson, C. T. B., C K Law, W. T., Cernansky, N. P., Miller, D. L., and Lindstedt, R. P. (September 19, 2010). A high-temperature chemical kinetic model of n-alkane (up to n-dodecane), cyclohexane, and methyl-, ethyl-, n-propyl and n-butyl-cyclohexane oxidation at high temperatures, jetsurf version 2.0. <http://web.stanford.edu/group/haiwanglab/JetSurF/JetSurF2.0/index.html>.
- [Wang et al., 2018] Wang, H., Xu, R., Wang, K., Bowman, C. T., Hanson, R. K., Davidson, D. F., Brezinsky, K., and Egolfopoulos, F. N. (2018). A physics-based approach to modeling real-fuel combustion chemistry-i. evidence from experiments, and thermodynamic, chemical kinetic and statistical considerations. *Combustion and Flame*, 193:502–519.
- [Wang et al., 2019] Wang, Y., Jain, A., and Kulatilaka, W. (2019). Co imaging in piloted liquid-spray flames using femtosecond two-photon lif. *Proceedings of the Combustion Institute*, 37(2):1305–1312.
- [Xu et al., 2018] Xu, R., Wang, K., Banerjee, S., Shao, J., Parise, T., Zhu, Y., Wang, S., Movaghar, A., Lee, D. J., Zhao, R., et al. (2018). A physics-based approach to modeling real-fuel combustion chemistry–ii. reaction kinetic models of jet and rocket fuels. *Combustion and Flame*, 193:520–537.
- [Zhang et al., 2014] Zhang, M., Wang, J., Xie, Y., Wei, Z., Jin, W., Huang, Z., and Kobayashi, H. (2014). Measurement on instantaneous flame front structure of turbulent premixed ch₄/h₂/air flames. *Experimental Thermal and Fluid Science*, 52:288–296.
- [Zhang et al., 2019] Zhang, W., Wang, J., Lin, W., Guo, S., Zhang, M., Li, G., Ye, J., and Huang, Z. (2019). Measurements on flame structure of bluff body and swirl stabilized premixed flames close to blow-off. *Experimental Thermal and Fluid Science*, 104:15–25.

[Zhang et al., 2020] Zhang, W., Wang, J., Lin, W., Mao, R., Xia, H., Zhang, M., and Huang, Z. (2020). Effect of differential diffusion on turbulent lean premixed hydrogen enriched flames through structure analysis. *International Journal of Hydrogen Energy*, 45(18):10920–10931.

APPENDIX

These experiments were conducted in collaboration with John Schihl, Ph.D candidate of Mechanical Engineering at Michigan State University. This appendix provides a brief overview of the results.

As mentioned before, the captured signal of CH^* chemiluminescence with the specific filter involves background CO_2^* emission and C_2 . Figure A.1 shows the chemiluminescence spectrometry of JP8 at different equivalence ratios.

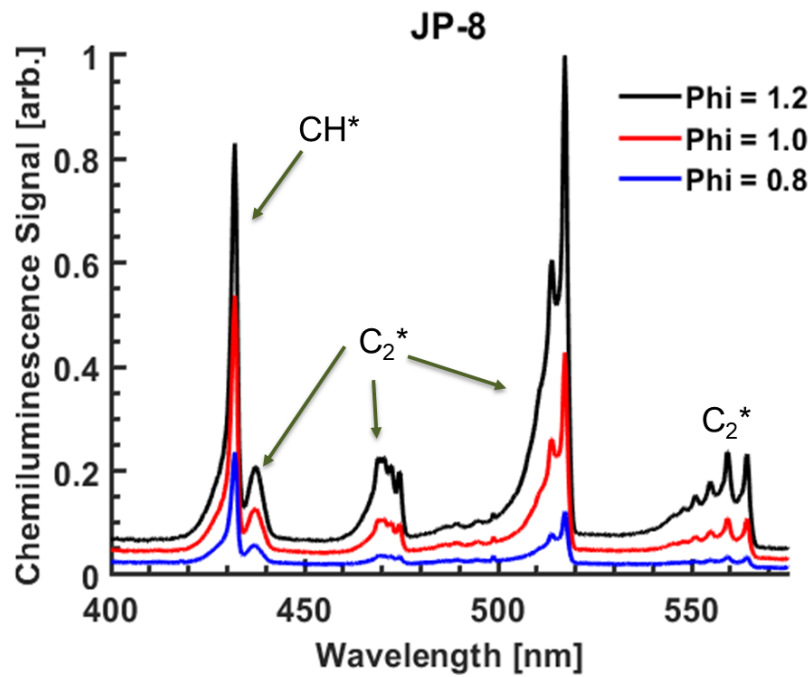


Figure A.1: Chemiluminescence spectrometry of JP8 at different equivalence ratios

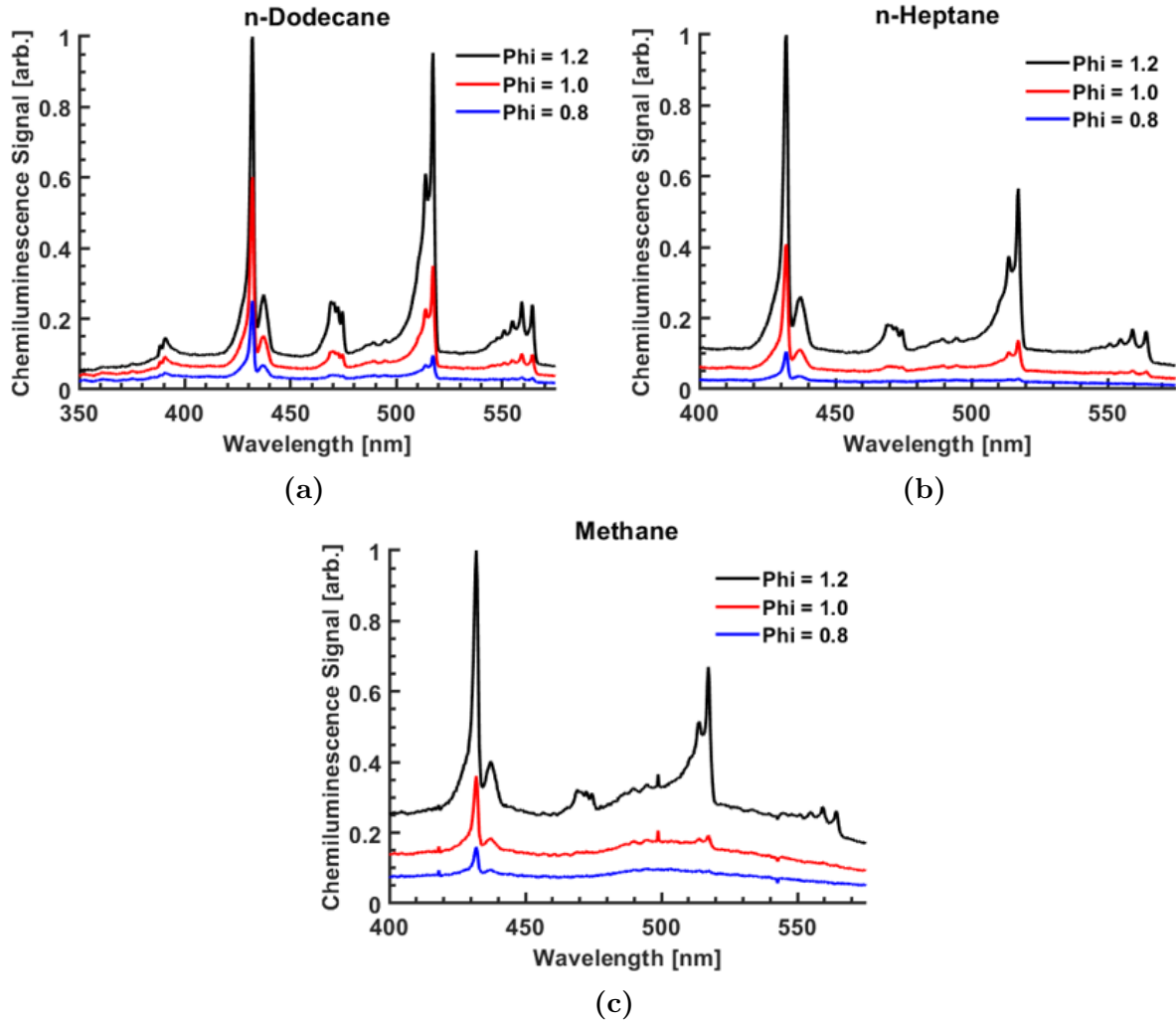


Figure A.2: Chemiluminescence spectrometry of (a) n-Dodecane, (b) n-Heptane, and (c) Methane s at different equivalence ratios

As shown here, other than background CO_2 emission, there are regions with C_2^* chemiluminescence which can affect the total CH evaluation. Figure A.2 shows the chemiluminescence spectrometry of n-Dodecane, n-Heptane, and methane at different equivalence ratios. Rich fuel flames produce more CH chemiluminescence compared to the lean cases. However, it is not just CH that is captured and measured. The figure A.3 shows a zoomed-in view of chemiluminescence in the region of the CH signal around 430 nm for all fuels at an equivalence ratio of 1.

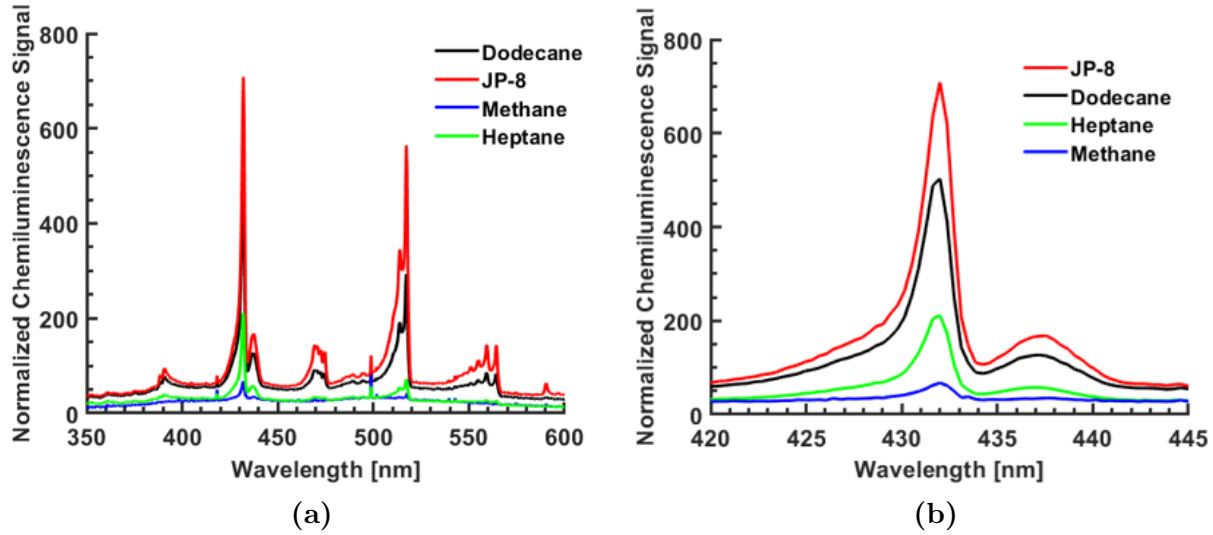


Figure A.3: (a) Chemiluminescence spectrometry of liquid fuels and Methane at equivalence ratio $\phi = 1$ (b) zoom in around CH chemiluminescence to observe CO_2 and C_2^* contributions

There are two peaks in the spectrometry around 433 nm and 438 nm. The first one is CH, and the latter is the C_2 signal. Due to the width of the CH filter equipped in the experiment, the C_2 chemiluminescence is captured as well. The amount of C_2 chemiluminescence gets higher as the equivalence ratio of liquid fuels increases. Therefore, the total CH signal received is a superposition of CH, C_2 , and CO_2 . First, the effect of background CO_2 should be calculated. Then the contribution of C_2^* is investigated, and finally, the total effective CH chemiluminescence will be measured and reported.

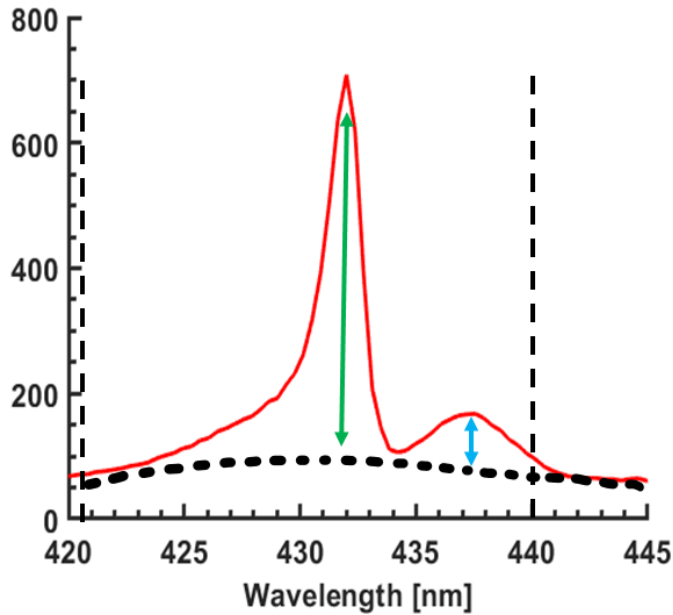


Figure A.4: Chemiluminescence spectrometry of JP8 around 430 nm wavelength

Figure A.4 shows background CO_2 in JP8 spectrometry within regions of CH chemiluminescence. To calculate the contribution of CO_2 to CH chemiluminescence, we measure two areas: one below the CH chemiluminescence, and the other one is the area below the black dotted line. Then, if we subtract the second area from the first area, the total CH chemiluminescence without background CO_2 is measured. Figure A.5 shows the effect of background CO_2 on the CH chemiluminescence captured in experiments. For liquid fuels, the contribution of CO_2 is around 30 to 50 percent, while it's around 60 to 80 percent for methane. The CO_2 contribution is higher in lean conditions compared to rich flames for all fuels. Also, liquid fuels show higher CH chemiluminescence and insensitivity to equivalence ratio.

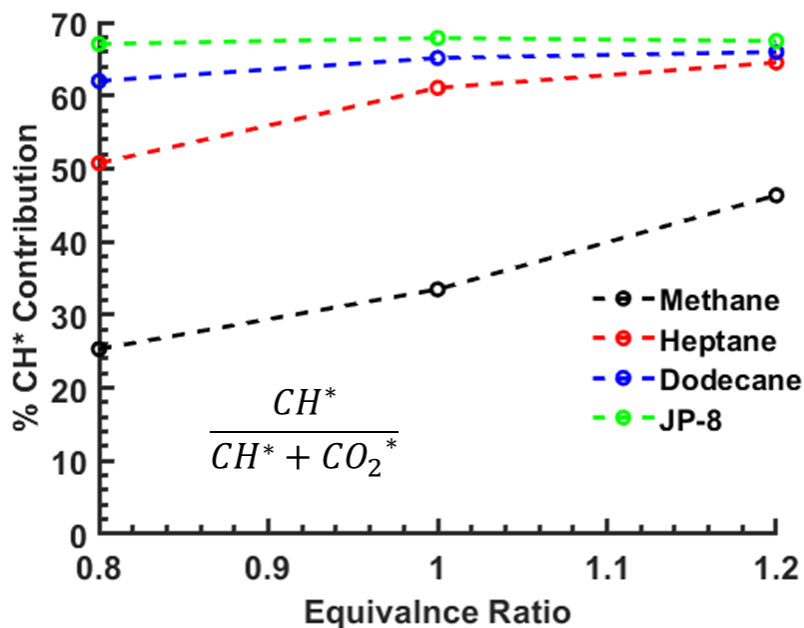


Figure A.5: Ratio of CH chemiluminescence without background CO_2 to total CH chemiluminescence with consideration of CO_2

Now we try to calculate the effect of C_2^* on the CH chemiluminescence similarly to what we did with CO_2^* . Based on Figure A.4, we calculate two areas: one between the CH chemiluminescence and black dotted line (green and blue arrows together), and the other one is the area where the blue arrow represents. The total CH^* chemiluminescence is calculated without the contribution of CO_2^* . Just similar to CO_2 measurement, we calculate two areas and subtract the second one from the first one. The results are shown in Figure A.6. It seems that the C_2^* contribution remains constant across equivalence ratios for all fuels. The variation of CH^* with equivalence ratio is proportional to the change in C_2^* with an equivalence ratio. Also, all fuels show similar behavior regarding C_2^* contribution across different equivalence ratios.

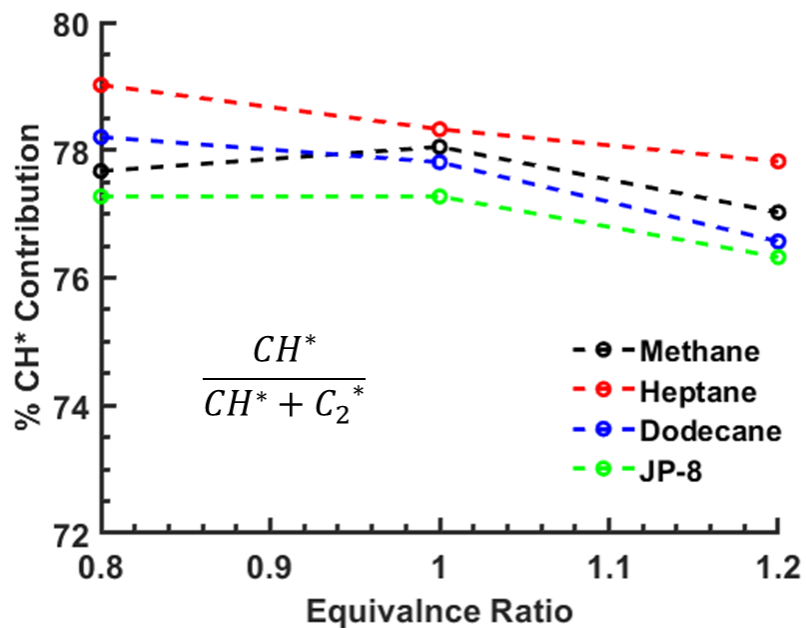


Figure A.6: Ratio of CH chemiluminescence without background C_2^* to total CH chemiluminescence with consideration of C_2^*

Finally, if we do these steps together, we can calculate the pure CH^* chemiluminescence regarding the elimination of CO_2 and C_2 . Figure A.7 shows the percentage of CH contribution to what is actually captured in experiments, including the effects of CO_2 and C_2 .

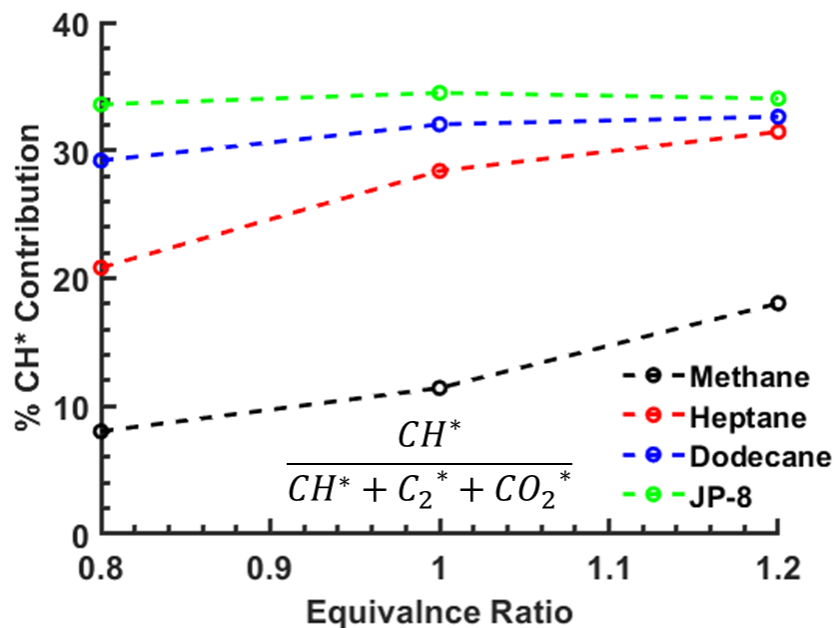


Figure A.7: Ratio of only CH chemiluminescence to total CH chemiluminescence with consideration of CO_2^* and C_2^*

The CH chemiluminescence improves by increasing the equivalence ratio, especially for methane. It seems that around 60 to 70 of what we record in experiments is CO_2 or C_2 , not CH. These results are based on a 10 nm filter around 430 nm wavelength. This suggests implementing a narrow filter to reduce the participation of C_2 and CO_2 in chemiluminescence.